Experimental research into the potential of pressure reconstruction on surface piercing hydrofoils with regard to ventilation

R.C. Belmer

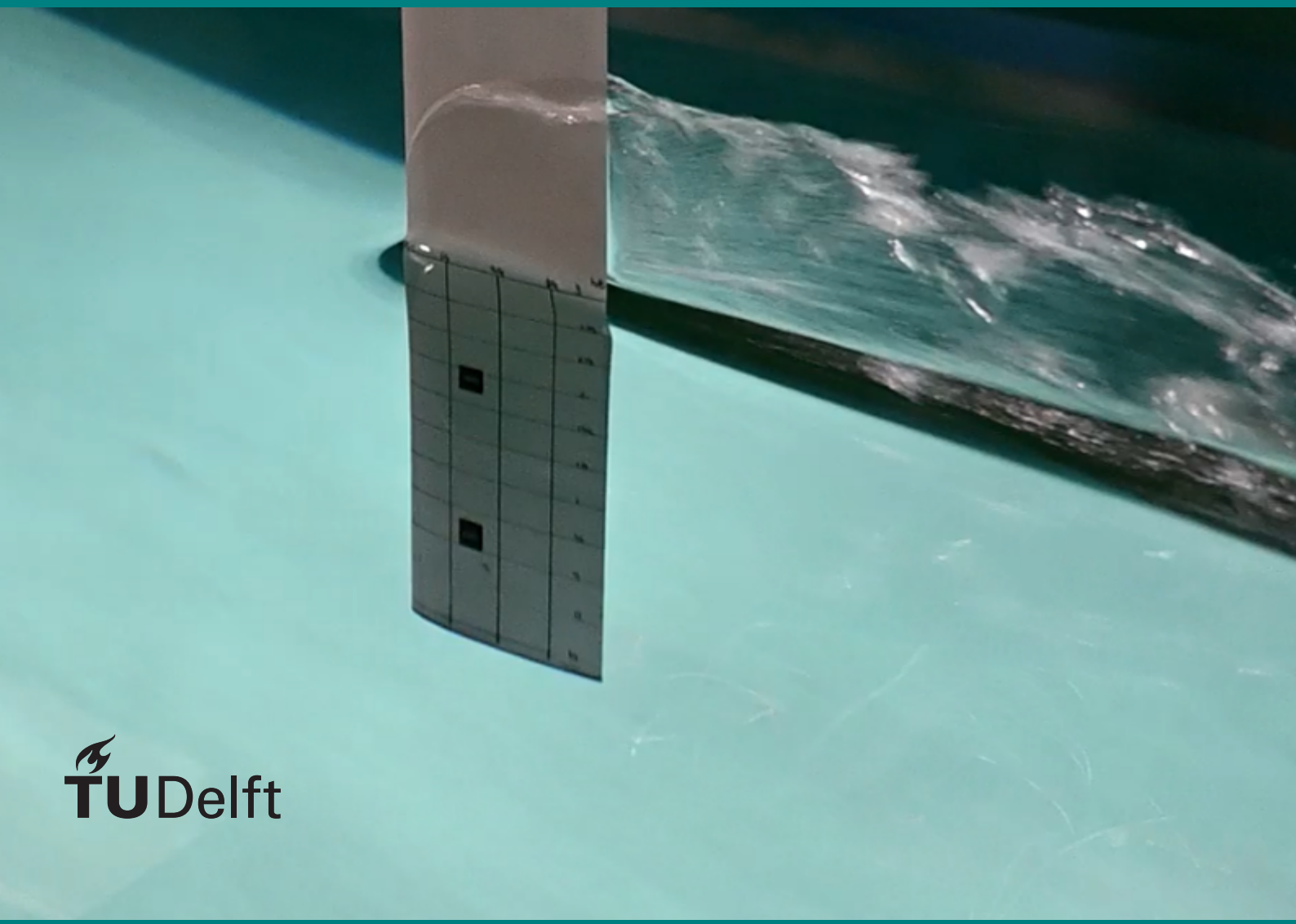

TU Delft

Thesis for the degree of MSc in Marine Technology in the specialisation of *Hydrodynamics and Ship Design*

Experimental research into the potential of pressure reconstruction on surface piercing hydrofoils with regard to ventilation

by

R.C. Belmer

This thesis (MT.22/23.026.M) is classified as confidential in accordance with the general conditions for projects performed by the TUDelft.

To be defended publicly on February 17, 2023 at 09:30 AM.

Student number:	4499468	
Project duration:	Nov 16, 2021 – Feb 17, 2023	
Thesis exam committee:	Dr. ir. I. Akkerman,	Chair
	J. L. Gelling,	Staff member
	Dr. ir. D. Fiscaletti ,	Staff member
	Dr. ir. P. de Vos ,	Staff member

TU Delft

Preface

This thesis, ”Experimental research into the potential of pressure reconstruction on surface-piercing hydrofoils with regard to ventilation”, is the grand finale of my academic career at the TU Delft. This academic career started back in 2015, with the bachelor Maritime Technology. Next to this I had the gained some in-field maritime experience. I continued with the master program of Maritime Technology of which this research is the last mark. I believe there is no other field of work better suited to me than the maritime field. And it is that feeling that made me enthusiastic, persevere and enjoy my time at 3Me.

Starting this thesis, my knowledge of hydrofoils was limited. After reviewing and studying basic concepts and other people’s work I found a knowledge gap in the behaviour of ventilation. In aid of the goal in the future to make ventilation a predictable and repeatable event, this research explores the possibility of tracking ventilation using full surface pressure reconstruction.

As this is an era coming to an end, I would like to thank all teachers and staff I have come across in the last seven years. A special thanks regarding this final stretch goes out to my graduation supervisors. Jaap for always giving me the broader picture, and also for the opportunity to connect with the amazing people from VPLP. A thank you to Ido for giving sharp analysis and out-of-the-box ideas. Also a word of appreciation to Jasper, Pascal, Frits, Peter, Jennifer, Gunnar, and Sebastian, for all the work you have done with and for me during the experimental phase.

I hope you enjoy reading this research.

R.C. Belmer
Rotterdam, February 2023

Abstract

Introduction Hydrofoils are often used for high-performance craft. They enable the hull to rise out of the water and reduce drag. A recurring problem is ventilation, this is the presence of a cavity filled with ambient air on the lifting surface. Ventilation causes the lift of the hydrofoil to decrease drastically. A lot of research has been done on ventilation behaviour. Ventilation remains a stochastic phenomenon to this day. The same operational conditions do not yield the same flow behaviour, a correlation between the pressure on the lifting surface and ventilation behaviour might exist. This research is an intermediate step towards finding a correlation between pressure on the surface of a foil and ventilation, making ventilation repeatable. The main goal of this research is to find out if a full surface pressure reconstruction can aid the search for a correlation between pressure and ventilation.

Method The test geometry is a NACA0012 surface-piercing hydrofoil with pressure measured using 2 rows of 15 pressure tappings. Extension pieces are used to obtain the span-wise pressure distribution while keeping the submerged span constant. The test program has three sets: all vertical runs (Set 1), high roll angle runs (Set 2), and runs with ventilation (Set 3).

During the experiment, the loads are measured with force transducers on a frame that measures forces in 6 degrees of freedom. The calibration of the force transducers is performed prior to the experiment. The calibration of the pressure sensors is done first using a 9 meter water column before the experiment and during the experiment in the towing tank, extra re-calibration (stepped runs) data is collected. The collected force measurement data is processed to attain the lift and drag coefficients. The pressure measurements are translated to the pressure coefficient and placed in a matrix on the right location of the lifting surface.

Results Based on repeated experimental runs the percentage differences are obtained on sensor and array levels. 30% of the sensors have a percentage difference of more than 10%, while the maximum difference for an entire array is 2.5%. A cross-check between the upper and lower arrays showed a percentage difference above 15% for 28% of the sensors, with a maximum difference of 1.2% at the array level. The pressure distributions at 0° roll angle, from Set 1, match the general pressure distribution characteristics. Comparing the 3D lift coefficient computed from the pressure measurements to that of the force data or an empirical method yields ambiguous results. The 3D lift coefficient based on the pressure measurement is within a 4% difference to Xfoil. The result of the high roll angle runs, Set 2, show the effect free-surface proximity has on the chord-wise pressure distribution. For the shallowest pressure reconstructions, close to the free-surface, the pressure distribution shows a minor peak near the leading edge after which the curve drops to near zero quickly. The operational conditions do not affect the quality of measurements. During two runs ventilation occurred, this is Set 3. The time-traces of the three forwardmost sensors show a dip prior to ventilation, with one sensor displaying an oscillating response. It is hypothesised that this is the position where ventilation is induced, but based on the results this can not be proven. All sensor response follows the same pattern when the ventilation bursts over the surface. The set-up is able to capture quick pressure changes.

Conclusion The percentage difference is too high for too many sensors. On the array level, however, the difference is considered small enough. The results of set 1 are in good agreement with known data. The results obtained at 60° roll angle are concluded to be of the same quality as for 0° roll. The method is capable of providing results in a wide range of operational conditions. Based on the ventilation runs, no correlation to pressure reading has been found. The time-traces of the sensors near the leading edge of these runs do show fluctuations prior to ventilation. With more ventilation runs available, it is highly likely that a correlation can be established. Due to the slim data set, it is possible that the conclusions drawn will be refuted in the future when a larger data set is available. Currently, the goal has not been achieved, and it cannot be stated with certainty that the method used here to attain a full surface pressure reconstruction can be used to correlate pressure to ventilation.

Contents

List of Figures

List of Tables

Nomenclature

α	Angle of attack
Γ	Circulation
γ	Vortex sheet strength
μ	Mean value
ν	Kinematic viscosity
Ψ	Stream function
ρ	Density
σ	Source sheet strength
σ	Standard deviation
σ_v	Ventilation inception number
σ_y	Yield stress
τ	Shear forces
θ	Local surface angle
A	Area
a_0	2D lift slope
AoA	Angle of attack
AR	Aspect ratio
BP	Bunching parameter
c	Chord
C_D	3D drag coefficient
C_L	3D lift coefficient
C_P	Pressure coefficient
CM	3D moment coefficient
Cd	2D drag coefficient
Cl	2D lift coefficient
Cm	2D moment coefficient
CoG	Center of gravity
D	Depth ventilated cavity
D	Drag force in 3D
d	Drag force in 2D
E	Lifting surface correction
F	Free surface correction factor
Fn	Froude number
FV	Fully ventilated
FW	Fully wetted
g	Gravitational acceleration
h	Submergence
h_m	Mean submergence
I	Moment of inertia
L	Lift force in 3D
l	Lift force in 2D
LE	Leading edge
M	Moment in 3D
m	Moment in 2D
N	Sample size
P	Local pressure
P_∞	Free stream pressure
P_{atm}	Atmospheric pressure
PV	Partly ventilated
R	Nose radius
r	Radius
Re	Reynolds number
Re_{crit}	critical Reynolds numer
s	Span
TE	Trailing edge
V	Velocity
V_∞	Free stream velocity

1 Introduction

1.1. Motivation

In the latest Transat Jacques Vabre, IMOCA boats with and without foils competed against each other. The average speed of the top three foilers was only 0.6% faster than non-foilers, which was a disappointment as a 6% increase was expected. The expected increase in speed by using hydrofoils is not achieved, the results are even somewhat disappointing. This is partly due to ventilation, a common issue that affects nearly all hydrofoils at some point. If ventilation can be prevented or delayed, a significant performance improvement is expected.

Figure 1.1: IMOCA 60, with surface piercing hydrofoil (Editor, 2020)

A hydrofoil is a small underwater structure that allows a boat's hull to partially rise out of the water, reducing the wetted surface area and wave-making volume. This results in a significant decrease in drag and a corresponding increase in speed. The IMOCA boats, as shown in figure 1.1, have surface-piercing hydrofoils. Due to the lifting surface intersecting with the free-surface, this type of

hydrofoil is prone to ventilation. Ventilation is the phenomenon of ambient air being sucked onto the hydrofoil reducing the lifting capacity drastically, this results in a decrease of performance. Ventilation is also known to be stochastic since the same operational conditions do not always yield the same ventilation behaviour (Wadlin, 1958). This makes it difficult for researchers to analyse, but more importantly, it can pose dangerous situations for sailors.

1.2. Current knowledge regarding ventilation of surface-piercing hydrofoils

Ventilation leads to a significant reduction in lift. When ventilation occurs, the forces on the foil change significantly and can even reverse. Breslin conducted experiments on surface-piercing foils and measured the force for both fully wetted (FW) and fully ventilated (FV) conditions. He found that in fully ventilated flow, the lift force is only a result of the wetted side. The ventilated cavity forms on the suction side of the foil, from which in FW flow the lift predominantly originates. The pressure side only has a small lifting capacity, hence the large reduction in lift (Breslin and Skalak, 1959). Breslin's data showed a reduction of around 70% of lift in fully wetted conditions compared to fully ventilated conditions at an angle of attack of 15° at various speeds. With increasing angle of attack, the drop in lift also increases(Breslin and Skalak, 1959). An exploratory study by Kiceniuk found lift coefficient reduction of up to 80%, at AoA 17.5° (Kiceniuk, 1954).

For ventilation to occur, two prerequisites are necessary: a path of air ingress and a negative pressure peak. Research has been done on how to block the path of air ingress, for example by using fences, but most conclude that the additional drag created by these constructions does not outweigh the improved resistance against ventilation (Swales et al., 1974). This leaves the negative pressure peak as the focus for further exploration.

The pressure distribution of a hydrofoil is closely related to ventilation. Currently, it is possible to predict and calculate the pressure profile of a hydrofoil using existing methods and tools. By including an indication of the expected ventilation behaviour based on the pressure profile, hydrofoil designers can take ventilation into account during the design process. For IMOCA boats, operational conditions are crucial for performance. The impact of operational conditions, roll angle, and proximity to the free surface on ventilation is emphasised. Various measurement techniques have been employed in the past, and the advantages and disadvantages of the most commonly used techniques are documented.

1.2.1. Ventilation quantifiable using pressure measurements

Ventilation forms at high speed and high angle of attack, but it is not a repeatable or quantifiable point. Harwood formulated the section cavitation number which he based on a submerged Froude number for a surface-piercing hydrofoil(Harwood et al., 2016). Barden carried this out further to make a ventilation inception number as shown in equation 1.1 (Barden and Binns, 2012). When this number becomes negative the likelihood of ventilation is present. This equation is also used in a study on kite foils (Bartesaghi et al., 2022), as a low-fidelity indicator.

$$\sigma_v = \frac{P - P_{atm}}{\frac{1}{2}\rho V^2} \tag{1.1}$$

The ventilation inception number will give a likelihood for ventilation for even a slight under pressure. However, for ventilation to occur, a significant under pressure is needed, as well as a path of ingress (Acosta, 1973), (Wadlin, 1958). The ventilation inception number is not a foolproof indicator of whether or not a foil will ventilate under certain operational conditions, but it can provide an indication of the foil's performance during the design process. By comparing two foils and computing the ventilation inception number, it is safe to say that the foil with the lowest number is likely to perform better regarding ventilation (Bartesaghi et al., 2022). Waid states that the vapour cavitation number is the most significant parameter to quantify the inception of ventilation, since this number is based on the local pressure coefficients, this indicates that pressure measurements can aid the research (Waid, 1968). All of the above studies agree that ventilation as observed is not a repeatable process, and

there is information missing to make the experiments repeatable.

1.2.2. Ventilation behaviour in various operational conditions

Placing a surface-piercing hydrofoil under a high roll angle, mimics the operational condition of an IMOCA hydrofoil. Under high roll angles, a surface-piercing hydrofoil is partly in the proximity of the free-surface. In the proximity of the free-surface the lift force is decreased. Decreasing the distance between the lifting surface and free-surface will decrease the *Cl/Cd* ratio (Wadlin et al., 1954), (Ashworth Briggs, 2018), (J. R. Binns et al., 2008). The effect on the pressure distribution is given by Parkin, who found that the pressure peak decreases for increased proximity to the water surface (Parkin et al., 1956). It also concluded that at higher speeds, the pressure distribution resembles that of a fully submerged hydrofoil, with the minimum pressure peak increasing as speed increases (Parkin et al., 1956). Do note these experiments are executed for a horizontally placed hydrofoil, thus different flow effects can occur for a surface-piercing lifting surface.

A NACA0012 T-foil is found to have equal hydrodynamic values (lift and drag) at both 0° and 30° roll angle. Ventilation is observed only for the 30° roll condition (J. R. Binns et al., 2008). Expanding on this by implementing more roll angles in an experiment would be interesting.

Next to rolled experiments, Binns showed that with increasing proximity of the free-surface, both the lift and drag coefficients reduce (J. R. Binns et al., 2008). Experiments were carried out from an h/c of 0 to 3. The lift and drag curves versus h/c tend to reach an asymptotic value. The trend of the curve matches those of other research (Ashworth Briggs, 2018, Wadlin et al., 1954). For an increased angle of attack, the asymptotic value is reached at higher h/c values (J. R. Binns et al., 2008). For a surface-piercing hydrofoil, the free-surface effects are never negligible since the crux is in the intersection of fluid and air domain. The influence submergence ratio has on the hydrodynamics, can be helpful when verifying own results.

Ventilation of surface-piercing struts is often found past the stall angle. THe stall angle indicated when the flow has separated from the foil highly increasing the risk of ventilation (Michel et al., 1954).

1.2.3. Experimental methods

Depending on the desired result of an experiment a specific measurement technique is chosen. In this research, emphasis is on measuring pressure distributions along a foil and capturing ventilation behaviour. Which method is able to do so using a rather small model (surface-piercing hydrofoil) for a wide range of operational conditions (free-surface proximity and high roll angles). Measuring techniques which can be used to capture pressure and flow properties on a surface are discussed. Namely; hot-films, particle image velocimetry (PIV), pressure sensors and pressure tappings. In these sections, the basic methodology will be explained from which also potential shortcomings or restrictions will follow.

Hot-films can determine if a flow is laminar or turbulent. This method can track at which location the transition happens. The hot-film sensors measure the temperature of the water. When this is constant, the flow is laminar. If this starts to fluctuate the flow is turbulent ((J. Binns et al., 2009)). In essence, this is a simple method to obtain the location of a difficult to predict transition point on the foil. The calibration of hot-films is a very complex procedure to carry out (Akhlaghi et al., 2020). The hot-film method is not yet a standard at the DUT testing facility. Employing this technique is very interesting but will at the same time be too time consuming.

Particle image velocimetry (PIV) is a technique that captures images of the flow around an object seeded with small particles to measure the fluid flow velocity. Mono and stereo PIV exist. Mono PIV uses a single camera to capture two images of particles and calculates velocity through cross-correlation of particle displacement. Stereo PIV, on the other hand, uses two cameras to simultaneously capture the flow from different angles and determine velocity based on particle depth information, leading to a more accurate measurement. Mono PIV is simpler to implement but less precise, while Stereo PIV is more complex but provides higher accuracy. PIV requires a laser and thus one or two cameras, all must not be attached to the model but to the towing carriage. The benefit of this is that the test geometry does not need to house any equipment or sensors that need to be attached. Whereas more traditional measurements yield a number of discrete measuring points, PIV

stands out because it is a non-intrusive measurement technique, which captures a continuous field. The set-up system of the cameras and laser is sensitive to vibrations, induced by the carriage. The technique is so sensitive to vibrations because if the camera vibrates it will capture the particles on a different position than they actually are. Jacobi has done research into this to map the error due to vibrations and correct for those, using a correction factor (Jacobi et al., 2016). The disadvantages of the PIV method, are the difficulty of coping with a wide range of operational conditions and the inability of measuring close to the free-surface. The set-up of two cameras and a laser is a precise procedure, calibration takes a really long time and therefore it is best if the test geometry moves very little. Due to the reflection of the free-surface the cameras are unable to capture the particles close to the waterline.

Surface mounted pressure sensors are currently being developed by the DUT hydrodynamics department, which can be integrated in a model to capture the pressure on a surface directly (Schreier and Poelma, 2018). These pressure sensors are developed with the purpose of getting insight into sloshing. They are however perfectly applicable to integrate into a hydrofoil to measure the pressure distribution. The sensors are made with micro-electro-mechanical system (MEMS) devices. These are widely used to measure static pressure and can operate in liquid. The sensor itself measures 1.7 x 1.7 mm, and is soldered on a printed circuit board (PCB), connected to a data acquisition system. The smallest sensor dimensions are 25 x 12 x 2.5 mm. The surface of a foil is curved and implementing a rectangular shape will compromise the curvature. To minimise compromising the foil geometry placing this sensor is best done with the shortest side in the direction of the chord. This measurement technique is fairly simple to implement and due to its simplicity also reliable. However, the need for surface mounting and substantial size, using these sensors as the primary method would compromise the shape too much.

A combination of surface mounted pressure sensors and hot-film sensors is being developed as well. The sensor is 60x10x2.5 mm in size, this is 2 mm thinner than the previously mentioned sensor and 5 times longer. The sensor contains a pressure sensor and a hot-film sensor. Now the sensor is rigid, but they are moving towards developing a flexible sensor making it even better applicable to hydrofoil (or any model with a curved surface) testing (Schwerter et al., 2017).

Pressure tappings are a more traditional method. Tiny tappings are drilled into the surface to which a tube is attached, the tube leading to the pressure sensor. The tubes allow the pressure sensor to be placed in or outside the model. An example set-up is shown in figure 1.2. This method is used often in research to back up the more novel measuring techniques. The method is relatively simple. The tubes must be filled with water, and have no air bubbles in there. Any air bubble compromises the measurement.

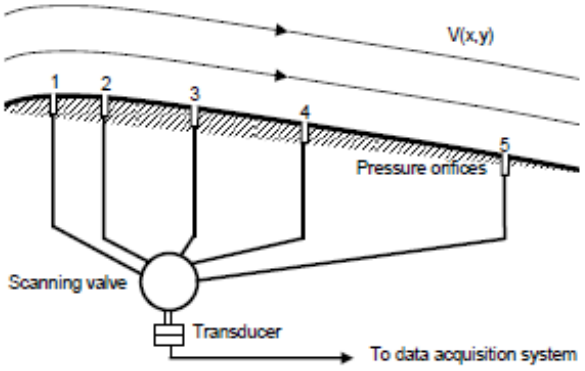

Figure 1.2: Schematic overview of application of pressure tapping in surface of a foil (Ragni, 2012)

Kuester investigated the disturbance which may be caused by the presence of pressure tappings. Pressure tappings of different diameters were tested from which was found that the measured pressure is effected by the diameter in a turbulent flow. A pressure tapping of 1 mm diameter near the leading edge creates a triangular-shaped turbulent wake which taints the tappings behind. After

sanding the edges of the tapping, the wake is still present thus it was deduced that it is not caused by edge roughness. The 0.5 mm diameter pressure tap did not show this turbulent wedge, thus it is best to use 0.5 mm taps (or even smaller). Do note these tests are conducted in a wind tunnel. Kuester concluded that the effect of the tapping on the pressure measurement is small (Kuester et al., 2016).

To obtain a pressure distribution several tappings must be drilled into the surface. The tappings must not disturb the tappings behind it. Traub executed a study to map the potential effect pressure tappings might have on the pressure distribution, and compared the experiments to Xfoil. A row of pressure tappings was placed in-line, at an angle of 30° and a vertical row on the leading edge. From this, no indication of interference due to the tapping on the measurement was found. Pressure tappings which are in-line did cause the flow to transition to turbulent prematurely at Reynolds number of 200,000 in air, which would approximate a Re of 2,810,000 in water. These speeds will not be reached in this experiment thus in-line placement of pressure tappings is not thought to be a problem (Traub and Cooper, 2008).

1.3. Research objective

Ventilation is a known problem where a lot of studies and research have already gone into. From previous studies, it is concluded that blocking the path of ingress is no suitable solution. Since for performance yachts, the increased drag is unacceptable. The opportunity lies in the second necessity for ventilation, which is the negative pressure peak. The ultimate goal is correlating pressure values to ventilation. Based on the literature, the pressure measuring method of choice is the pressure tappings. The space needed inside the test geometry is small, the disturbance caused by this method on the surface is little and the working principle is relatively simple.

This research is an intermediate step towards finding a true correlation between pressure on the surface of a hydrofoil and ventilation. The goal is to aid the research into ventilation, by creating a pressure reconstruction method that yields validated results for high roll angles and free-surface proximity.

A test geometry must be designed, which can be used for all wanted tests from the test program. The right measuring equipment must be chosen, after which the system is built and calibrated. A method for data processing must be proposed, such that the incoming data yields usable results. It should be shown what the quality of the results is compared to other known data. For this, a set of vertical experiments is carried out. To show the ability of the method to work in a wide range of operational conditions, there is a set of experiments for which the foil has a very high roll angle. If during the experiments ventilation occurs, this is an opportunity to search for a correlation.

1.4. Research questions

The main goal of this research is to give a reliable method to map the pressure distribution over the full span of a surface-piercing hydrofoil. This is a step towards trying to make ventilation quantifiable. The main research question is:

”Can a full surface pressure reconstruction made with pressure tappings aid the search to correlate pressure and ventilation?”

With supporting sub-questions:

- How repeatable is the method?
- How do the experimental pressure results compare to known data?
- Does the method yield valid results when the foil operates under high roll angles?
- Can a correlation to the pressure distribution be found if there is ventilation?

1.5. Thesis structure

The report starts with a deeper theoretical background in chapter 2. Then the method is divided into chapters 3, 4 and 5. Chapter 3 is on the experimental preparation regarding test program, geometry and equipment. Chapter 4 depicts the calibration process and results. Chapter 5 shows the method

used for data processing, from incoming data to plots. The results are depicted in chapter 6 together with the accompanying analysis and discussion. In chapter 7, the general discussion, limitations and recommendations are given. Lastly, in chapter 8, the conclusion is stated, here the answer to the research question is given.

2

Theoretical background

In this chapter, more in-depth theory is given about hydrofoils and ventilation. The first section introduces the hydrofoil. Explaining the working principle, different methods of computing the hydrodynamics and what conditions or design choices can affect the performance. In the second section, the phenomenon of ventilation is introduced as are the formation and elimination mechanisms.

2.1. Hydrofoil

A hydrofoil operates in water with the main purpose to generate lift. In this section, the hydrofoil is discussed by first giving an introduction to hydrofoils. Second, different methods of calculating the lift coefficient and other hydrodynamic coefficients are discussed. Thereafter the influence of operational conditions, hydrofoil shapes and material on a hydrofoil are discussed.

2.1.1. Introduction to hydrofoils

The cross-section of a typical geometry of a hydrofoil is shown in figure 2.1. The chord *(c)* is the shortest distance from leading to the trailing edge and the hydrodynamic centre is defined at quarter chord *(c/4)*.

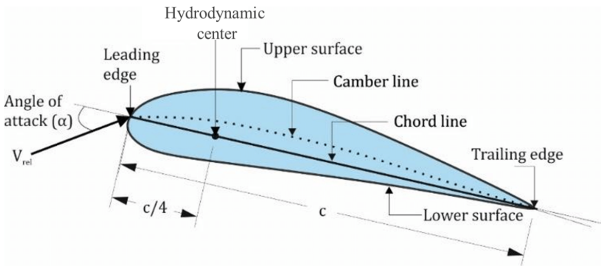

Figure 2.1: Geometry of a foil (Muratoglu et al., 2016)

A hydrofoil produces lift because of a superposition of a circulating and homogeneous incoming flow (Michel et al., 1954). This can be explained using the fundamentals of fluid mechanics, which can be found in the appendix section A. Bernoulli's equation (eq. 2.1) states that the sum of the static pressure, dynamic pressure and hydrostatic pressure is constant along a streamline (the streamline is the path tangent to the velocity vector of the water particles at all points). For a hydrofoil the vertical translation is small, thus the potential energy component is neglected. Based on equations 2.1 it is concluded that the pressure must decrease when the velocity of a fluid increases.

$$P + \frac{1}{2}\rho V^2 + \rho g z = constant \tag{2.1a}$$

$$P + \frac{1}{2}\rho V^2 = constant \tag{2.1b}$$

Assuming only a uniform flow over a foil, an upward vortex forms at the trailing edge due to viscous effects. However, conservation of momentum must be maintained. Thus, a clockwise circulating flow forms around the foil. This circulating flow reduces the incoming flow on the lower side and accelerates the flow on the top of the foil (Hoerner and Borst, 1975). The total flow around a foil is a superposition of the incoming uniform flow and the circulating flow, see figure 2.2.

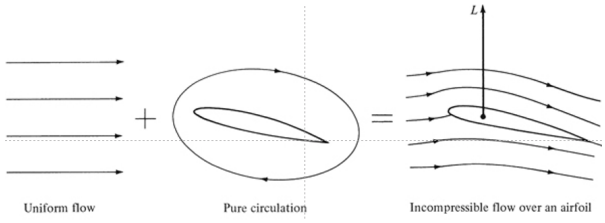

Figure 2.2: Superposition of flow around a foil (Hoerner & Borst, 1975)

On the lower surface (pressure side) of the foil, where the velocity is reduced there is a higher pressure area and on the upper surface (suction side) there is a lower pressure. The pressure distribution over the chord of a foil, is plotted in figure 2.3.

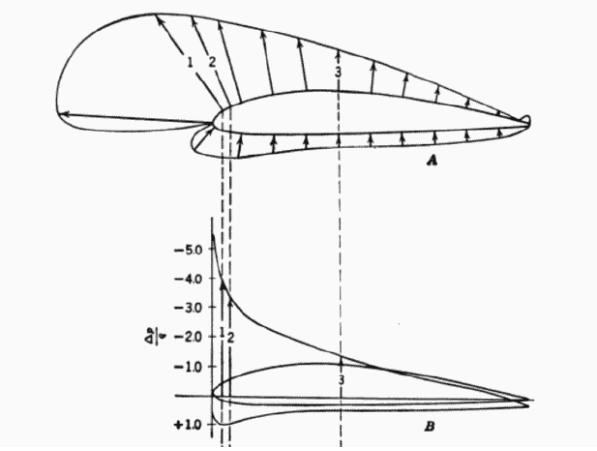

Figure 2.3: Pressure distribution on foil, with corresponding pressure coefficient plot (Pope, 1951)

The pressure distribution over the chord length is often denoted with the pressure coefficient (*Cp*), which is described in equation 2.2.

$$C_p = \frac{P_{local} - P_{atm}}{P_{dynamic}} \tag{2.2a}$$

$$C_p = \frac{P - P_\infty}{\frac{1}{2}\rho V^2} \tag{2.2b}$$

A pressure distribution plot gives great insight into the (prospected) performance of a hydrofoil. For example, a hydrofoil that has partly separated flow is shown in figure 2.4. In the corresponding

pressure distribution, a *plateau* can be seen in the curve where the separation bubble is located.

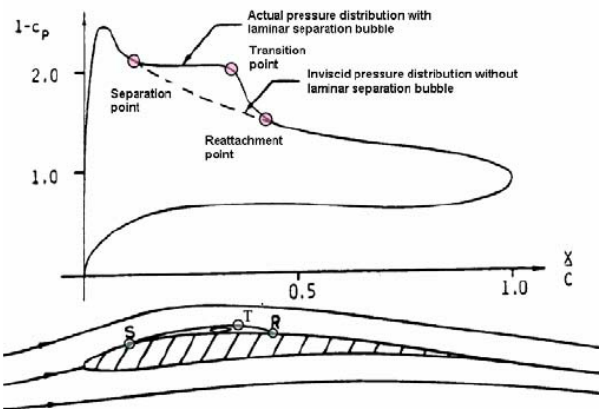

Figure 2.4: Pressure distribution on foil, with partial separation (Russell, 1979)

The pressure distribution determines the lift and drag forces on the foil, taking the integral of the pressure distribution will yield the hydrodynamic force (Pope, 1951). Lift is defined perpendicular to the direction of movement and drag is always parallel but in the opposite direction of movement. The ratio between drag and lift determines the efficiency of the foil, *L/D* or *Cl/Cd* ratio. The drag of the foil can be split into a friction drag which is a result of pressure tangential to the surface caused by viscosity, and a form drag which is a result from normal pressure. Hoerner explains viscosity as *"Molecular resistance which fluid particles exhibit against displacement in relation to each other and with respect to the surface of a solid body"* (Hoerner, 1976). The drag coefficient is highly dependent on the shape and the Reynolds number. The Reynolds number becomes decreasingly important as it gets higher, so at some point the drag will only be a function of the shape since at that point the viscous effects have been minimised (Acosta, 1973).

Lift force is the integral of pressure on the foil using equation 2.3, where θ denotes the local angle of the surface to the free stream inflow.

$$L = \int_A (-Psin\theta - \tau cos\theta) dA \tag{2.3}$$

For easier comparison of performance to another research independent of size (scale), the lift and drag forces are made dimensionless. A distinguishing between 3D and 2D is made with either capital or lowercase letters. For a 3D analysis the equations are given in 2.4c; in which L, M, and D are the forces for lift drag and moment. The 2D hydrodynamic coefficients are denoted by l, m, and d and described in equations 2.5.

$$C_L = \frac{L}{\frac{1}{2}\rho V^2 hc} \tag{2.4a}$$

$$C_D = \frac{D}{\frac{1}{2}\rho V^2 hc} \tag{2.4b}$$

$$C_M = \frac{M}{\frac{1}{2}\rho V^2 hc^2} \tag{2.4c}$$

$$C_l = \frac{l}{\frac{1}{2}\rho V^2 c} \tag{2.5a}$$

$$C_d = \frac{d}{\frac{1}{2}\rho V^2 c} \tag{2.5b}$$

$$C_m = \frac{m}{\frac{1}{2}\rho V^2 c^2} \tag{2.5c}$$

2.1.2. Using numerical, analytical and empirical methods to compute hydrodynamics of a hydrofoil

When a hydrofoil is fully submerged, its flow pattern resembles that of an airfoil with the same geometry and speed. As a result, aerodynamic methods are often used for base calculations, like Xfoil. However, two major differences must be considered: the finite length of the hydrofoil and its proximity to the free surface. To account for the finite length, the AR correction from lifting line theory can be applied. The free surface correction can be approached as the biplane effect or taken from empirical methods.

Xfoil is a program created by Mark Drela in 1986 that aids in the design and analysis of foils. Xfoil is particularly applicable to low Reynolds numbers ($\mathrm{Re} < 0.5 \cdot 10^6$) foils, which is the operational range of hydrofoils. Xfoil can solve both inviscid and viscous analyses. This demands a way to capture the complex transition of separation and an algorithm that can solve the non linear coupling between the inviscid, viscous and transitional flow. The three main necessities of this program lie in;
(1) laminar and turbulent viscous formulations
(2) a transition formulation
(3) a global Newton solution method. (Drela, 1989)

Xfoil is based on a panel method, also called a boundary element method (BEM). A panel method is a numerical computation of discretised elements which form the foil surface. It is no analytical method, though this method can be scripted using Matlab without the need for complex computational fluid dynamics programs. On each element of the surface, an elemental flow is imposed. The streamlines are recreated to match the original shape. Further, the condition of no penetration is imposed on the surface of the foil. When applying the Kutta condition (the pressure at the upper and lower surface at the trailing edge (node 1 and node N) must be equal, fig. 2.5) the analysis becomes numerically solvable. Elementary flows that exist are uniform, source, doublet and vortex. To describe the flow around a foil, the uniform and vortex flows are used (recall figure 2.2).

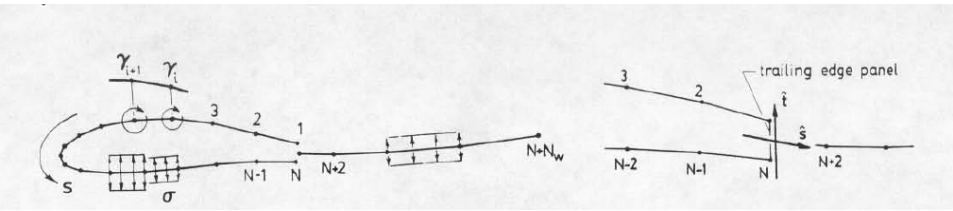

Figure 2.5: Graphic of panel distribution and elemental flows. On the right, the Kutta condition on the trailing edge panel is shown (Drela, 1989)

For the inviscid computations, a linear-vorticity stream function is formulated which is a superposition of uniform flows, vortex sheet strength (γ) on the surface of the foil and source sheets with strength (σ) on the wake:

$$\Psi(x,y) = u_\infty y - v_\infty x + \frac{1}{2\pi}\int \gamma(s)\ln r(s;x,y)ds + \frac{1}{2\pi}\int \sigma(s)\theta(s;x,y)ds \tag{2.6}$$

Herein s is a coordinate along the panels (see figure 2.5), r is the spacial difference between a point s and the coordinate point in x,y. θ is the vector angle towards point s, and u_∞, v_∞ are the free stream velocity components rotated with respect to the angle of attack.
Xfoil discretises the surface of the foil into N panels, the size and refinement location of panels are editable by the user, the wake consists of N_w panels. The panels are assumed flat. Great care should therefore be given in the allocation and refinement. Each foil panel has a linear vortex strength distribution (γ_i) and the wake panel a constant source strength (σ_i). After imposing the Kutta condition that $\gamma_1 + \gamma_N = 0$ the system becomes linear solvable (Drela and Youngren, 2001). The surface vorticity is equal to the surface velocity, thus the pressure coefficient at each panel can be computed using:

$$C_{p,i} = 1 - \left(\frac{\gamma_i}{q_\infty}\right)^2 \tag{2.7}$$

There is also the inviscid mixed-inverse procedure, which allows the designer to have a part of the foil geometry prescribed and a part of the foil velocity distribution described. For parts of the foil, either the velocity distribution is computed as shown above, or the velocity distribution is known and the method is inversed to find the geometry. Especially the last method is of great use when a certain pressure distribution is desired and a little compromise on geometry is allowable (Drela and Youngren, 2001).

For a viscous flow analysis, the source strengths on the wake are not known. These need to be computed with the boundary layer equations which then are implemented to create a solvable system again. The boundary layer equations are the compressible integral momentum and kinetic energy shape parameter equation. The transition point from laminar to turbulent can be determined by the user in the parameter N_{crit}. This number has a huge influence on the performance as it in a sense implies the ratio of the area of the foil which is in a laminar or turbulent flow. Drela does give some ballpark numbers for N_{crit} in a number of situations, regrettably non-applicable for a hydrofoil (Drela and Giles, 1987).

Lifting line theory is an analytical method from which the formulation of correction of finite length can be obtained. A formulation is found to compute 3D lift coefficient (C_L) from the sectional lift coefficient (C_l) by correcting for the aspect ratio (AR).

$$C_L = \frac{C_l}{(1 + 2/AR)} \tag{2.8}$$

There is an additional correction that can be applied which holds for foils with a small AR, small AR being less than 10 (Michel et al., 1954). That is the lifting surface correction (E), for AR between 2 and 10 E is empirically found by:

$$E = 1 + 2/AR^2 \tag{2.9}$$

Free-surface correction imposes a correction on a 2D found solution such that the effect of the free-surface is taken into account. At low Froude numbers, the free-surface effect can be split into a wave and a rigid wall effect. The wave effect reduces the efficiency of the strut, while the rigid wall effect increases it. At high Froude numbers, the surface effect resembles the biplane effect on a foil (Michel et al., 1954, P.7-9). Low Froude numbers are lower than considered practical, thus the biplane effect is the parameter which dictates the free-surface correction (F). The free-surface correction found from (Michel et al., 1954, P.2-26) is based on a K factor which is approximated at 1.08, than the correction factor is found using the following fomrula:

$$F = 1 - \frac{K}{\pi \cdot AR} = 0.9006 \tag{2.10}$$

Empricial methods exist to predict hydrofoil performance. Here one of Damley is shown which predicts 3D lift coefficient for a vertical hydrofoil and on of Tinney dat predicts the influence on th C_L based ono the roll angle of hydrofoil.

An empirical method of Damley for vertical surface piercing hydrofoils is explained. It predicts the 3D lift coefficient for 0° roll angle. The method is a non-viscous prediction. (Damley-Strnad et al., 2019).

$$C_L = \frac{a_0 \sin\alpha}{\frac{E}{F} + \frac{a_0}{\pi AR_h}} + \frac{4}{3}\left[1 - \frac{AR_h}{10}\right]\sin^2\alpha\cos\alpha \tag{2.11}$$

Where a_0 is the 2D lift slope, α the angle of attack, AR_h the submerged aspect ratio, E is a edge correction factor and F a free-surface correction factor. The computation of E and F are shown below, in which h_m is half the submergence h.

$$E = \sqrt{1 + \left(\frac{a_0}{\pi AR}\right)^2} \tag{2.12}$$

$$F = 1 - 0.422e^{-1.454 h_m/c} \tag{2.13}$$

This correction for the free-surface as proposed by Damley, depends on the averaged submergence and chord length, this correction factor is empirically found especially for vertical surface-piercing hydrofoils.

An analytical expression for the influence on the 3D lift coefficient due to roll angle is expressed by Tinney (Tinney, 1954). The expression takes into account roll angle and finite length (AR correction). In equation 2.14, the formula is shown, in which the initial C_L is the measured lift coefficient at 0° roll and AR is the aspect ratio.

$$C_L = C_L(0) \cdot \left(1 - 0.422e^{-0.364 AR \tan(\phi)}\right) \tag{2.14}$$

2.1.3. Influence of operational conditions on performance

Typical foil characterisation curves show the lift and drag coefficients over a range of angles of attack as seen in figure 2.6. As the angle of attack increases, the lift coefficient will increase, until a sudden drop of lift is observed (Acosta, 1973). The angle for which this occurs is called the stall angle. Experimental studies showed that the dynamic stall angle is higher than the static stall angle (Breslin & Skalak, 1959). This stall angle denotes an operational point at which the flow is not able to follow the surface anymore, the streamlined body has taken on the characteristics of a bluff body.

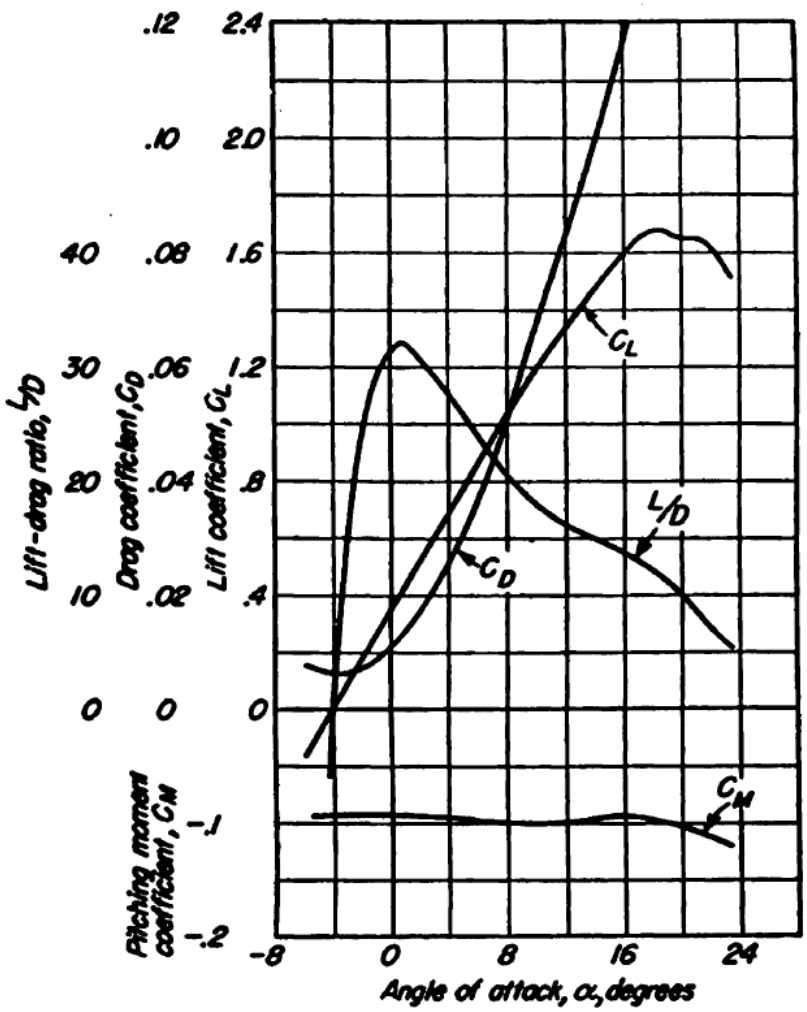

Figure 2.6: Typical foil characteristics (Abbott and Von Doenhoff, 2012, P3).

For increased speed and constant angle of attack, the lift coefficient will increase. The drag coefficient decreases under this condition since increased speed means an increased Reynolds number and the drag over the foil reduces for an increased Reynolds number. This results in an increased *Cl/Cd*, a higher efficiency. For constant speed and increasing angle of attack both lift and drag coefficients will increase, and the *Cl/Cd* will increase as well.

The speed at which the foil operates does not change the characteristic shape of the pressure distribution at moderate angles of attack, but it does influence the amplitude. The angle of attack has a bigger influence on the pressure distribution than the operating velocity, only at high angles of attack does the velocity cause a change in shape (Pinkerton, 1938).

The dynamic pressure on a foil is the result of speed and angle of attack, Acosta states that a reduction of dynamic pressure of 100kPa will possibly lead to cavitation (Acosta, 1973). Cavitation is the event of vapour bubbles forming due to the pressure dropping below the vapour pressure. Even before cavitation, there is a chance of ventilation to occur already at a dynamic pressure decrease of 50kPa on a foil (Ellsworth, 1967). The effect of roll angle on the hydrodynamic coefficients of a foil is researched by Binns. Interesting from this study was that the lift force seemed not to be affected by a 30° roll angle. The efficiency of the foil is also the same for a 0° and 30° roll angle (J. R. Binns et al., 2008). The used test geometry in this study is a T-foil, which under a roll angle will form a V-shape together with the strut. For a surface-piercing hydrofoil it is expected that the lift coefficient will drop for increased roll angle.

2.1.4. Influence of shape on performance

Hydrofoils are almost always streamlined bodies. A streamlined body will always have a reduced form drag compared to a bluff body (Hoerner, 1976). Parameters discussed that have an influence on the performance are the nose radius *(R)*, thickness ratio *(t/c)*, camber, and camber location.

Kermeen identified that foils with a larger nose radius show an increase in drag force, and decrease in lift-drag ratio. Larger nose radius also leads to a decreased cavitation number (Kermeen, 1956). Hoerner gives an optimum nose radius as percentage of the chord *(R/c)* between 1.5% and 2%, whilst having a *(t/c)* between 6 and 8% (Hoerner and Borst, 1975). In addition Rothblum states that at lower speeds a sharp leading edge shows unexpected random ventilation (Rothblum, 1969). A NACA0012 foil has a R/c ratio of 1.58%, but a thickness ratio of 12%.

A 12 % *(t/c)* is mentioned as most efficient thickness based on large number of experiments by Hoerner. This is an all-round well performing thickness, which does not mean that it is the best in every specific design condition. The effect of thickness is mostly seen in the drag, for increasing thickness ratio the drag will increase (Hoerner and Borst, 1975), (Winslow et al., 2018). Experiments executed by Perry showed that for increased thickness ratio the chance of ventilation increases (Perry, 1954).

Camber increases the lift significantly, the drag increases less pronounced (Winslow et al., 2018). An increased camber increases the lift force, it also shifts the zero lift line to a negative angle of attack (Hoerner and Borst, 1975). This shift means that a cambered foil needs less angle of attack to have the same lift force as a symmetrical foil. This can be beneficial taking into account stall angles. Camber also reduces the pressure peak at the leading edge. An indication of where on the foil the maximum camber should be is between 30 and 50% of the chord, this location will yield maximum lift (Hoerner and Borst, 1975).

2.1.5. Influence of surface on performance

A foil with surface roughness will have the transition point from laminar to turbulent flow more forward than a smooth foil. Surface roughness affects the critical Reynolds number of said object (Hoerner, 1976). Surface roughness on the pressure side of a foil can lead to an increased lift at some angles of attack. Surface roughness on the suction side will reduce the lift (Hoerner and Borst, 1975). Regarding surface roughness and total foil performance an experiment on a NACA0012 is done comparing a smooth surface to a grit 36 roughened surface. It was concluded that increasing roughness increases the drag and decreases the lift. An interesting result was that with increasing roughness the stall angle increases (Chakroun et al., 2004). This can indicate a larger operational profile can be reached without increased risk of ventilation. An experiment into the effect of surface finishes found no clear outcomes on a better finish (Williams et al., 2008). This can mean that a finish has no substantial effect, as long as the surface is smooth or it can indicate the finishes used are too similar to obtain a clear result.

2.2. Ventilation

In this section first, an introduction to ventilation is given. Second, a more in-depth description is given of how ventilation develops. Third and lastly a piece on the elimination of ventilation.

2.2.1. Introduction to ventilation

Ventilation is the presence of a cavity filled with atmospheric air on a hydrofoil (Wadlin, 1958). There are multiple mechanisms that can lead to the formation of this air cavity, but in all cases it forms when air gets sucked from the air domain into the fluid domain onto the lifting surface. The word suction is used since the air is drawn to a sub-atmospheric pressure area.

Two broadly accepted necessities for ventilation to occur, are a separation of the boundary layer (the possibility of ingress of air) and a low-pressure peak (suction peak).
The needed sub-atmospheric pressure for ventilation is found to be an approximate reduction of 50 kPa (Acosta, 1973). These necessary prerequisites to induce ventilation do not mean that when these are present ventilation is guaranteed to occur (Wadlin, 1958). The general tendency is also that ventilation is highly stochastic. There is a wide range of experiments that, when repeated, do not yield

the same results regarding ventilation. The presence and severity of ventilation are predominantly influenced by speed, angle of attack and the foil shape (Wetzel, 1957).

To make the determination of ventilation easier three flow regimes are distinguished around a hydrofoil. A fully wetted (FW), a partly ventilated (PV) and a fully ventilated (FV) flow. During operation, the flow can transition from one to another regime. The separation of these flow phases aids analysis, since within one regime the behaviour is more predictable.

In figure 2.7 a 2D foil section with increasing cavity length from fully wetted to fully ventilated is shown. The PV regime, shows the cavity might tend to shed off partly, meaning this is a non stable flow regime.

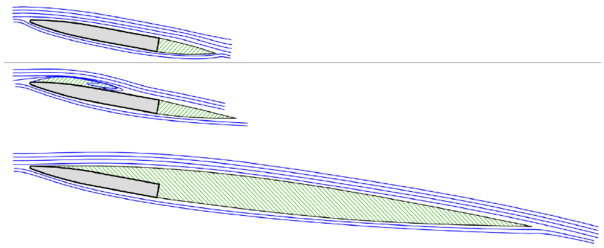

Figure 2.7: Flow regimes on a 2D foil section, top: fully wetted, middle: partly ventilated, bottom: fully ventilated. (Harwood et al., 2016)

In 3D different flow regimes can exist along the span, Harwood came up with guidelines to determine if a hydrofoil is ventilating or not. A fully wetted flow is easiest to determine since there is no sign of an air filled cavity anywhere. Apart from a possible bubbly wake which is most often present for foils with a blunt trailing edge (Acosta, 1973). Fully ventilated flow has an air cavity running along the entire submerged span. The partly ventilated flow is often non-stable and has a cavity which runs only partly down the span of the foil (Young et al., 2017), (Harwood et al., 2016), (Harwood et al., 2014). Figure 2.8 shows the different flow regimes and the guidelines proposed by Harwood.

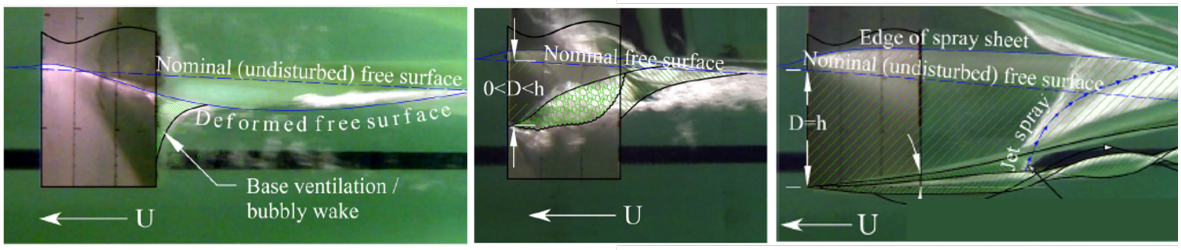

Figure 2.8: A hydrofoil in different flow regimes. 1) FW, 2) PV, 3) FV (Harwood et al., 2016)

2.2.2. Ventilation formation mechanisms

Foils have been tested in waves by Swales, it was found that ventilation was prone to induce near the crest of a wave. This is because the wave introduces a downward acceleration which locally changes the angle of attack of the incoming flow which is an influencing factor of ventilation (Swales et al., 1974).

Angle of attack and speed are operational conditions to indicate the probability of ventilation. On a more scientific level, there are two necessities in order for a ventilated flow to form; low pressure and path of ingress need to be present (Wadlin et al., 1954). This path of ingress is also referred to as a separation of the boundary layer. The separation of the boundary layer is described by Swales as the rupture of the free-surface seal, Swales observed three types of rupture: at the nose, at the tail and via the tip vortex (Swales et al., 1974). These three types of rupture are the main formation mechanisms of ventilation.

Nose ventilation begins to form on the leading edge of the hydrofoil at the free surface. Nose ventilation is prone to the downward acceleration of the foil (Swales et al., 1974). From the leading edge the ventilated cavity can travel downwards until the entire span is ventilated. Nose ventilation is often seen at moderate speed and at angles of attack close too or past the stall angle of a foil. This type is not that much dependent on speed, but more on the angle of attack (Wadlin, 1958).

Tail ventilation is the ventilation which forms at the trailing edge of the foil. This ventilation is seen most at high speeds and moderate angles of attack (Young et al., 2017). Once a ventilated cavity is attached to the foil it tends to 'burst' over the entire foil in a very short time.

Tip vortex ventilation can look similar to tail ventilation, since it also bursts from the trailing edge tip of the foil. However, the free-surface seal rupture is very different. The tip vortex of the foil travels from the tip too far behind the hydrofoil, this distance can be multiple chord lengths long (Ashworth Briggs, 2018). At some point the vortex makes contact with the free-surface and due to the low pressure on the foil air is sucked through the core of this tip vortex to the foil surface (Swales et al., 1974). Tip vortex ventilation is an often seen ventilation and hence a big problem (Parkin et al., 1956), (Acosta, 1973). Breslin even states that tip vortex ventilation is the most often occurring mechanism in his experiment. A sketch of this type of ventilation is shown in figure 2.9. The left shows a fully wetted foil and the right shows the tip vortex travelling in the wake of the foil toward the free-surface.

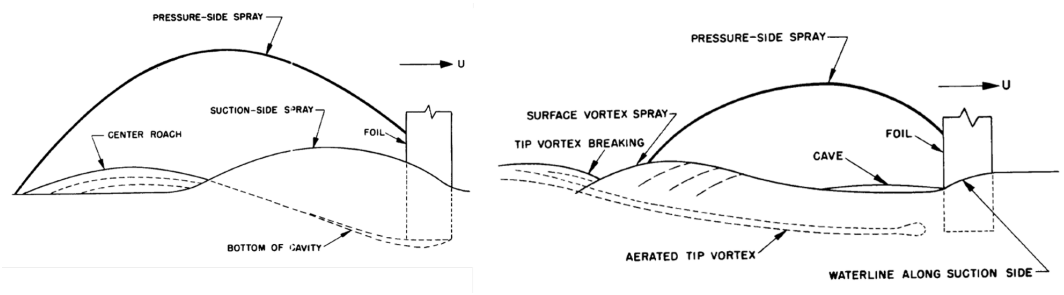

Figure 2.9: A fully ventilated flow on the left and right a sketch tip vortex-induced ventilation (Breslin & Skalak, 1959)

2.2.3. Ventilation elimination

The formation and elimination of ventilation are greatly influenced by the angle of attack and velocity of the foil. Rothblum conducted high-speed experiments in which is concluded that a stable ventilated flow remained present for a much lower angle of attack value than the ventilation had formed (Rothblum, 1969). To eliminate ventilation the velocity and/or angle of attack need to reduce drastically (Harwood et al., 2014), (Swales et al., 1974), (Breslin and Skalak, 1959).

Once a foil is ventilating, it is known that it is hard to get rid off, this is visualised in figure 2.10. The transition from a FV flow to a FW flow requires either a massive reduction in speed or in angle of attack. This is shown in a graph as a large hysteresis loop, seen in figure 2.10. The lift coefficient reduces enormously in this loop each time it goes from FW to FV, which is unfavourable when sailing (Acosta, 1973), (Wetzel, 1957), (Fridsma, 1963).

The behaviour of ventilation and the reduction in efficiency make it a popular and interesting topic of research. Eliminating or mitigating the ventilation or its hysteresis loop would increase performance (Breslin and Skalak, 1959), (Kiceniuk, 1954). Ventilation is observed a couple degrees past stall angle, but remains for long time even when reducing angle of attack. The needed reduction of angle of attack can be up to 10° (Kiceniuk, 1954).

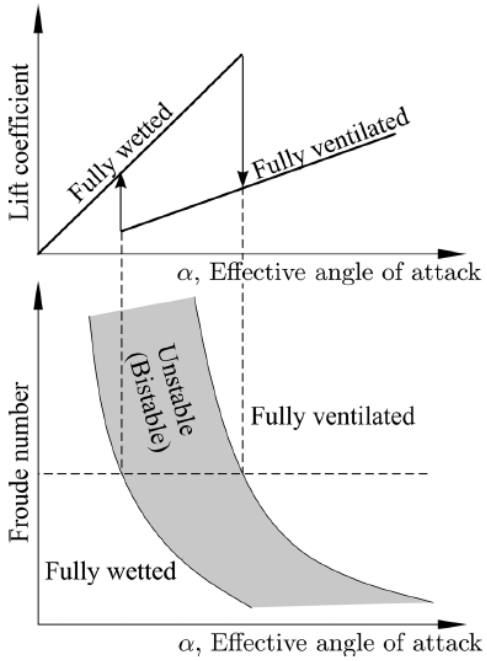

Figure 2.10: Hysteresis loop showing ventilation regime versus lift coefficient, angle of attack and speed (Young et al., 2017)

In figure 2.10 the area within the hysteresis loop is called the bi stable region, this is where the flow can move from FW to FV and back very quickly and is therefore difficult to model, even numerically. This bi-stable region is an unfavourable region from design and sailing perspective since no prediction on the effect of lift can be made. It might be better to *force* the hydrofoil towards a FW or a FV flow from a safety point of view. Better yet is if by some design the shift from FV to FW would come closer to each other, closing the loop. This would not eliminate ventilation, but it would widen the operational conditions and make measures to get rid of ventilation less extreme.

3

Method - Experiment preparation

This chapter encompasses all that is needed to build the experimental set-up. Therefore first the test program is given in section 3.1. In the design phase results of numerical simulations of Xfoil are used in force estimates. In section 3.2, the convergence study of Xfoil is depicted. The design process of the test geometry and considerations are elaborated on in section 3.3. The measuring equipment choices are shown in section 3.4. This chapter is the result of a simultaneous process in which a lot of choices influenced other parameters. The fourth section gives an overview of the total setup used in the towing tank.

3.1. Test program

The test program comprehends all runs needed to achieve the experimental goals. The test program is divided into three sets. Set 1 is to characterise the foil and to verify the method to known data. Set 2 is to test the work-ability under high roll angles, which means the lifting surface is in close proximity to the free-surface. Set 3 is a subset of the other two, it includes all the runs in which ventilation occurred.

The sets and their operational conditions are shown in table 3.1. All runs are carried out at a towing tank speed of 3 m/s. Set 1 is executed at 0° roll, a vertical configuration. This makes it possible to compare the results to theoretical and analytical values. Both negative and positive angles 8° and 12° are tested. This enables the reconstruction of a full surface pressure plot of suction and pressure side as the pressure tappings are only on one side of the foil. This set is carried out over the full range of the span, which is indicated by z/c 1.67 - 3. Within set 1 two dynamic sweeps will be carried out as well. The purpose of these dynamic sweeps is to provide the hydrodynamic force results over a large range of AoA to characterise the test geometry. These dynamic sweeps are either from +/- 4° to +/- 18°, purely rotated over the z-axis. The rotation is imposed by a script to the Hexamove, in which the period and boundaries of the rotation are set. The rotational speed is intentionally low, to prevent a contribution of added mass and other unwanted dynamic effects in the results.

The goal of set 2 is to explore workability and quality of results under high roll angles of 45° and 60°. Due to limited time at 45° only force is measured (since this only requires one run). At 60° roll angle, force and pressure is measured for AoA 8° and 12° are tested. Pressure reconstruction is done only on the suction side of the foil. A full suction side surface plot is obtained by doing measurements for the full span range.

Table 3.1: Test program

Set	V[m/s]	Roll [°]	AoA [°]	z/c [-]	Runs [#]
1	3	0	-12, -8, 8, 12	1.67 - 3	20
2	3	45, 60	8, 12	1.67 - 3	12
3	3	60	12	1.67	2

Before each test-run, first a null-run and then a stepped-run (only in set 1) is executed. The null-run result is used to deduct any pre-existing loads from the wanted result. The stepped-run is executed as an extra intermediate step, which can be used later to check the status of all sensors. The stepped-run is only executed in the vertical configuration, at high roll angles there is not enough vertical space to translate the model this much. The stepped-run is a static run, 0 m/s, that goes from z/c 1.67 to z/c=3 in 40 mm increments. The pressure result is a stepped response, this response is used in section 4.3 to perform a re-calibration.

3.2. Xfoil convergence study and numerical simulations

Xfoil predictions are used in the experimental preparation to estimate the loads on the foil. The Xfoil numerical simulations are also used to compare experimental results to measured values, in chapter 6. Xfoil has a lot of settings of which most are left at default. The most important settings are the number and location density of the panels and the value of Ncrit which varies dependent on the usage of the foil (ex. for the wind-tunnel experiment it is 9). Ncrit can be selected from 0 - 9, however unlike increasing the number of panels it does not yield a converged solution. Ncrit is selected at 3, based on comments made by both Drela and Speer on using Xfoil in regard to hydrofoils (Speer, 2004). A small convergence study is carried out to determine the number of panels. The maximum panels in Xfoil is 494, the number of panels has an effect on the maximum angle there is between panels. Several number of panels are run trough Xfoil, all using viscous mode at Re $3.42 \cdot 10^5$, the results are shown in table 3.2. Apart from the N = 20 panels, all values hover around the same value. Once above 50 panels, the effect on the results is limited, convergence is reached.

Table 3.2: Numerical outputs for various number of panels for AoA 8 and 12, at Re $3.42 \cdot 10^5$ for a NACA0012 foil

AoA 8°

N panels	Min Cp	Cl	Cd	Max panel angle
494	-3.789	0.875	0.016	2.21
400	-3.799	0.875	0.016	2.73
325	-3.803	0.875	0.016	3.36
210	-3.804	0.875	0.016	5.2
160	-3.807	0.875	0.016	6.85
120	-3.814	0.876	0.016	9.12
80	-3.826	0.876	0.016	13.78
50	-3.902	0.877	0.016	22.28
20	-4.226	0.872	0.019	50.32

AoA 12°

N panels	Min Cp	Cl	Cd	Max panel angle
494	-6.907	1.186	0.025	2.21
400	-6.912	1.186	0.025	2.73
325	-6.902	1.186	0.025	3.36
210	-6.916	1.186	0.025	5.2
160	-6.914	1.187	0.025	6.85
120	-6.911	1.187	0.025	9.12
80	-6.905	1.187	0.025	13.78
50	-6.984	1.184	0.026	22.28
20	-3.356	0.713	0.094	50.32

The effect the number of panels have on the pressure distribution is illustrated in figure 3.1. Only the pressure distribution obtained for 20 panels looks very segmented and deviates from the rest. The difference between the rest of the curves is negligible, the curves coincide. Based on these results the minimum number of panels would be 80. The default setting of Xfoil is 160 panels, for simplicity reasons this number of panels is adopted in this research.

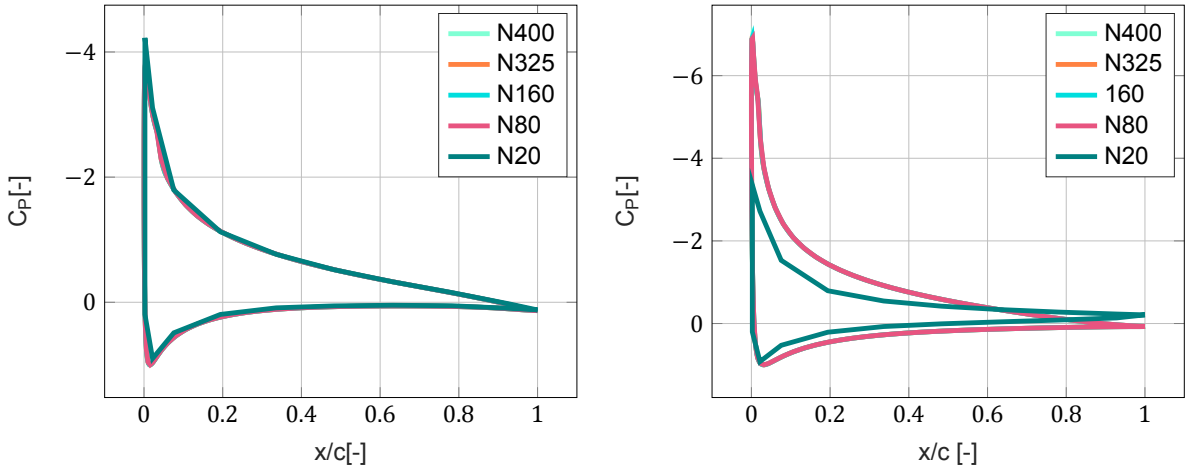

(a) AoA 8 ° (b) AoA 12°

Figure 3.1: Pressure distributions simulated with Xfoil for a NACA0012 at Re $3.42 \cdot 10^5$ for various number of panels

There is also a bunching parameter (BP), which dictates the ratio of panel distribution on the LE to the rest of the foil area. The default BP is set at 1. Bunching parameter from 0 to 3 is simulated, see figure 3.2. A BP of 0, indicates equal spacing between all the panels. Increasing BP leads to a decrease of the spacing between the panels toward the leading edge. In table 3.3 the minimum pressure coefficient, lift and drag coefficient and maximum panel angle are depicted. These results are simulated with the settings Ncrit = 3 and N = 160.

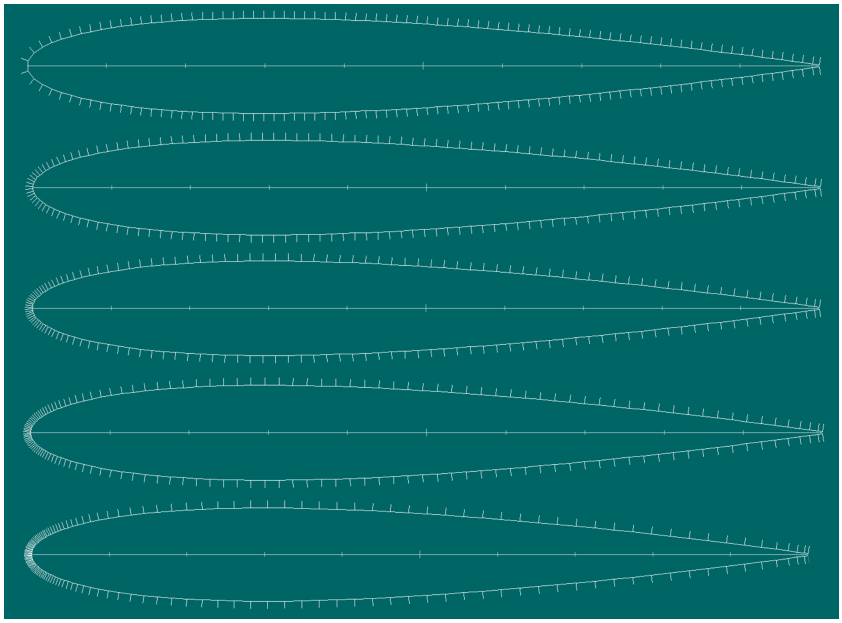

Figure 3.2: Visualisation of the bunching parameter in Xfoil on a NACA0012. From top to bottom BP = 0, 0.5, 1, 1.5 and 3

AoA 8				
BP	Min Cp	Cl	Cd	Max. panel angle
0	-4.01	0.871	0.016	38.04
0.5	-3.82	0.875	0.016	10.71
1	-3.807	0.875	0.016	6.85
1.5	-3.805	0.875	0.016	5.33
3	-3.802	0.875	0.016	3.7

AoA 12				
BP	Min Cp	Cl	Cd	Max. panel angle
0	-7.517	1.172	0.026	38.04
0.5	-6.951	1.187	0.025	10.71
1	-6.914	1.187	0.025	6.85
1.5	-6.916	1.187	0.025	5.33
3	-6.913	1.186	0.025	3.7

Table 3.3: Xfoil convergence based on the bunching parameter (BP), for AoA 8° and 12°, at Re $3.42 \cdot 10^5$ for a NACA0012 foil

The pressure distribution as simulated by Xfoil are shown in figures 3.3. From BP 1 or larger there is no significant difference anymore. Therefor the bunching parameter is set at 1.

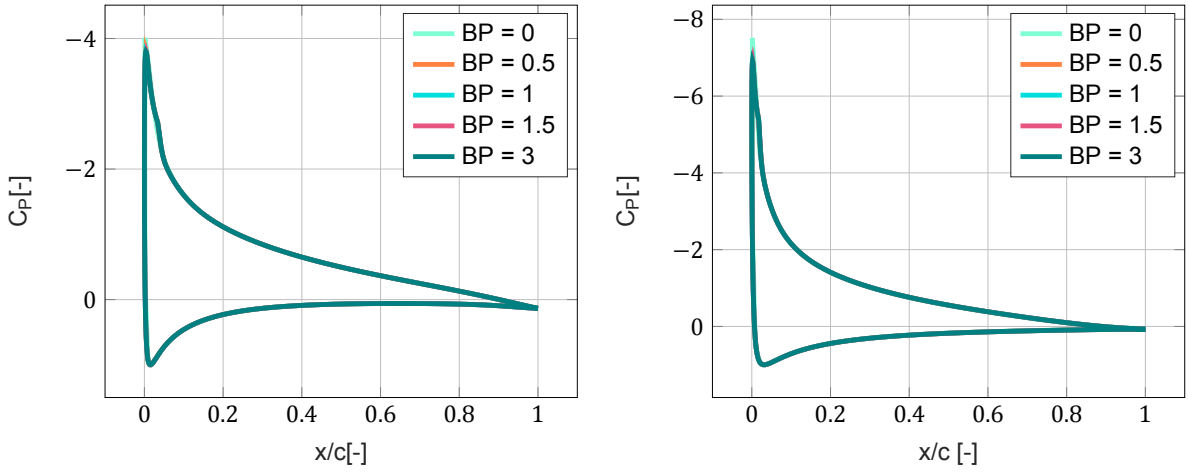

(a) AoA 8 ° (b) AoA 12°

Figure 3.3: Pressure distributions simulated with Xfoil for a NACA0012 at Re $3.42 \cdot 10^5$ for various bunching parameter (BP)

In Xfoil there is also an option XT, which dictates an area on the surface for which the panel spacing should be decreased. The influence of this parameter is checked, but it is concluded to not alter the result. Therefore this parameter is not used. In appendix C the results of this investigation are shown.

3.3. Test geometry considerations

The test geometry is a NACA0012 shaped surface-piercing hydrofoil (i.e. only a strut). This is a convenient shape, because there is extensive experimental data available for comparison. The shape is generally accepted as an overall okay performing foil. The symmetry of the foil makes alignment checks possible, by comparing the force results for equal but opposite yaw angles. This section is divided into four separate subsections which predominantly make up the design phase, the chord and span length, the extension pieces, the placement of the pressure tappings, and lastly some structural and mass properties are depicted.

3.3.1. Chord and span length

The chord is the characteristic length in regard to scaling. The chord also determines the available space inside the foil for tubing. The International Towing Tank Committee (ITTC) provides guidelines for model scale tests, but they are not relevant for hydrofoil testing. Since the primary scaling parameter is the Froude number, which does not relate to the physics of the flow around the foil. The flow properties around the foil are of interest, therefore the Reynolds number is a more appropriate parameter to use for scaling. Scaling according to the Reynolds number formulation (eq. A.4) would result in a larger model size than full-size, due to the lower test speed. This is not practical and would possibly lead to other problems in the tank such as reflection of the walls and bottom.

The critical Reynolds number (Re_{crit}) is used as the scaling parameter. The critical Reynolds number does not have a specific formula, because it is geometry dependent. It is generally considered to be reached after the major dip in the drag coefficient has occurred. The critical Reynolds number indicates the transition from laminar to turbulent flow near the leading edge and separation of the flow towards the trailing edge (Timmerman, 2017). The drag coefficient graph is therefore a good indicator of the critical Reynolds number, since the dip in drag is a result of the flow becoming turbulent instead of laminar.

The experiment must be conducted above the critical Reynolds number. Taking into account the towing tank carriage speed which can go up to 7 m/s (“Towing tank no. 1”, n.d.), this will give a chord length range. To avoid damaging the foil, the experiments will be performed at lower speeds within the available range. Future studies can examine the higher range of speeds.

For a NACA0012 foil, the drag coefficient is obtained over a range of Reynolds numbers for AoA 8° and 12° using Xfoil. It is expected that for increasing Reynolds number the drag coefficient will reduce drastically until the value becomes asymptotic. The critical Reynolds number is then taken at a point where the relative change in the drag coefficient is deemed small enough. The simulated results are plotted in figure 3.4.

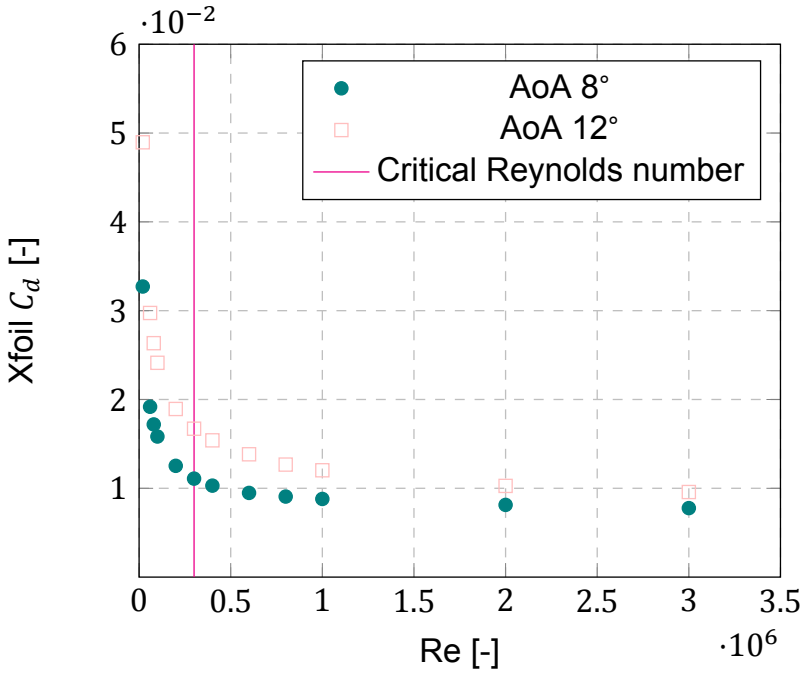

Figure 3.4: Exploratory runs using Xfoil to determine the critical Reynolds number of a NACA0012 foil, plotted is the drag coefficient as a function of the Reynolds number

The critical Reynolds number is a trade-off between the best flow characteristics and a usable velocity range for the experiments. Figure 3.4 illustrates the decrease in drag with increasing Reynolds number. The drag coefficient stabilises once the critical Reynolds number is surpassed. The critical

Reynolds number is chosen to be 300,000. From the plot is observed that the critical Reynolds number increases for an increasing angle of attack.

The chord length as a function of towing carriage speed and critical Reynolds number is as follows:

$$c = \frac{Re_{crit} \cdot \nu}{V} \tag{3.1}$$

The towing speed in this experiment is chosen to be 3 m/s. This yields a minimum chord length of 105 mm. Since there needs to be room for pressure tappings on the inside, a larger chord is preferable. It is chosen to use a chord length of 120 mm, at 3 m/s, this yields a Reynolds number of $3.42 \cdot 10^5$, which is a bit above the critical number. This scaling will ensure the same hydrodynamic behaviour in the model-scale as in the full-scale environment.

The span of the foil is determined by the maximum bending moment, the needed clearance from run-up/spray water to the sensors, and the h/c for which free surface effects are negligible.

Based on visual footage from previous experiments executed in the towing tank on hydrofoils an estimated maximum run-up height of 200 mm is established. Since the foil will be rotated for high roll angles the clearance from run-up to equipment must be kept also at an angle. Maintaining a 200 mm clearance at 60° angle makes a needed 400 mm clearance on the foil. Some significant submergence is wanted, to have a pressure reading which comes close to a 2D situation to compare. Some length is also wanted to get a reasonable aspect ratio comparable to foils used in the field, a minimum aspect ratio is determined at 2.5. Together, this already comes to a span of 700 mm. Taking into account there is some length underneath the lowest pressure tapping row and the translation range of the Hexapod, which requires some extra length the span is determined at 840 mm. The submerged span is 415 mm, this makes an aspect ratio of 3.46.

The foil is made of Aluminium-5083 (Alplan) material. Which has a yield strength is 195 MPa. The half thickness of the foil, and thus maximum distance from center to outer point material is 7.2 mm. The area moment of inertia is $14035.06mm^4$. The estimated load on the foil is 0.7 N/mm, which would come to around 600 N of side force on the foil. Following the basic equations for bending moment and bending stress the maximum allowable span will follow.

$$\sigma_y = \frac{M \cdot y}{I} \tag{3.2a}$$

$$M = \frac{1}{2} q \cdot s^2 \tag{3.2b}$$

$$Max\ span = \sqrt{\frac{2\sigma_y I}{qy}} = 1030mm \tag{3.2c}$$

The maximum span is 1030 mm, the determined 840 mm is well under this number and thus okay.

3.3.2. Extension pieces

There will be two rows of pressure tappings. A double row reduces the amount of needed runs for a full surface pressure plot. Whereas three rows would have been an overkill on channels for the DAQ system. The tappings are drilled at a fixed position. To make the full surface plot the foil is lifted a little out of the water between runs. Doing this decreases the submerged depth, making the hydrodynamics of each run different. The solution to this are fitted extension pieces, shown in figure 3.5. 3D printed extrusions are made to match the missing submergence. These are fitted underneath the foil and will be swapped in between runs to ensure constant submerged depth. The extension pieces are 3D printed with a SLA resin printer. There are two stainless steel bars fitted to transfer the load and maintain the structural integrity. The extension pieces are mounted to the foil, with three long screws.

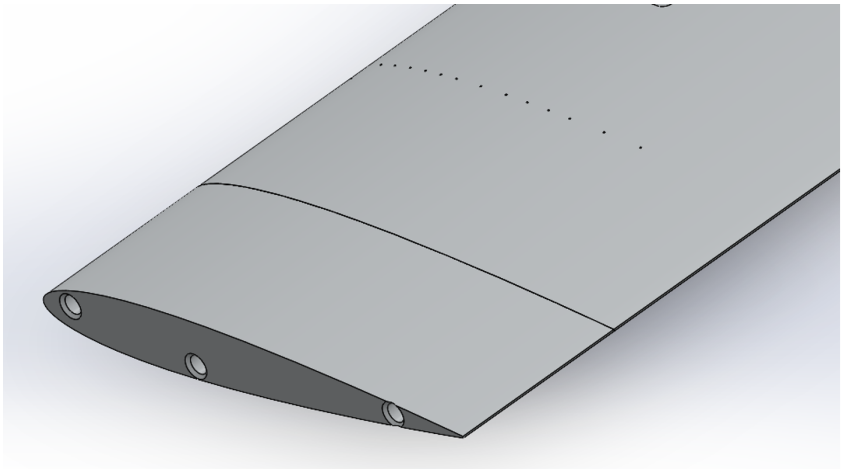

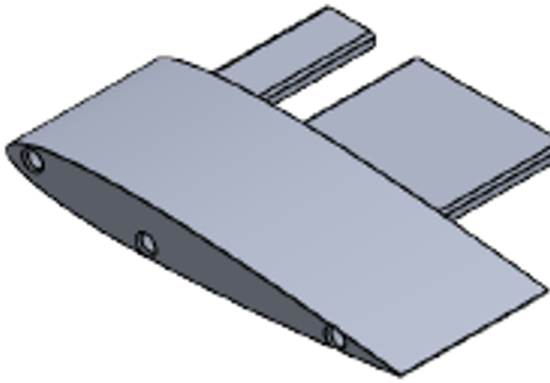

Figure 3.5: Extension pieces, left) fitted under the foil, right) the extension piece and stainless steel bars showing

The hexamove has a vertical translation range of 350 mm. The deepest pressure measurement is wanted at z/c of 3. Since a full surface pressure plot reconstruction is desired, the shallowest pressure measurement is very close to the free-surface. To leave enough slack in the pistons of the Hexamove for rotation of the foil, not the entire 350 mm of movement of the Hexamove is used on the Z direction. The amount of pressure readings in span-wise direction is set at 10, this means 5 runs and 4 extension pieces are needed. This is a trade-off between time, material costs and quality of the surface plot. Having the deepest submergence at 3 h/c, dividing the space by 10 gives an increment of 36 mm. This is rounded up to 40 mm increment per run. Four extension pieces are made of 40, 80, 120 and 160 mm in length. In appendix D.2, the technical drawings of the four made sizes are shown.

3.3.3. Placement of pressure tappings

In span-wise direction, the tappings are placed 175 mm apart from each other. The lower array is placed at 3 z/c (as low on the foil as possible), the upper array is at 1.54 z/c for the deepest measurement. This is shown in figure 3.6. Herein a distinction is made between h/c and z/c, since h/c is the submergence which is constant 3.46 throughout the entire experiment. Z/c denotes the depth ratio of the lower tapping array which varies between 1.67 and 3. On the left side the foil is shown in its deepest position, with no extension piece. On the right side, the highest position is shown, with the largest extension piece.

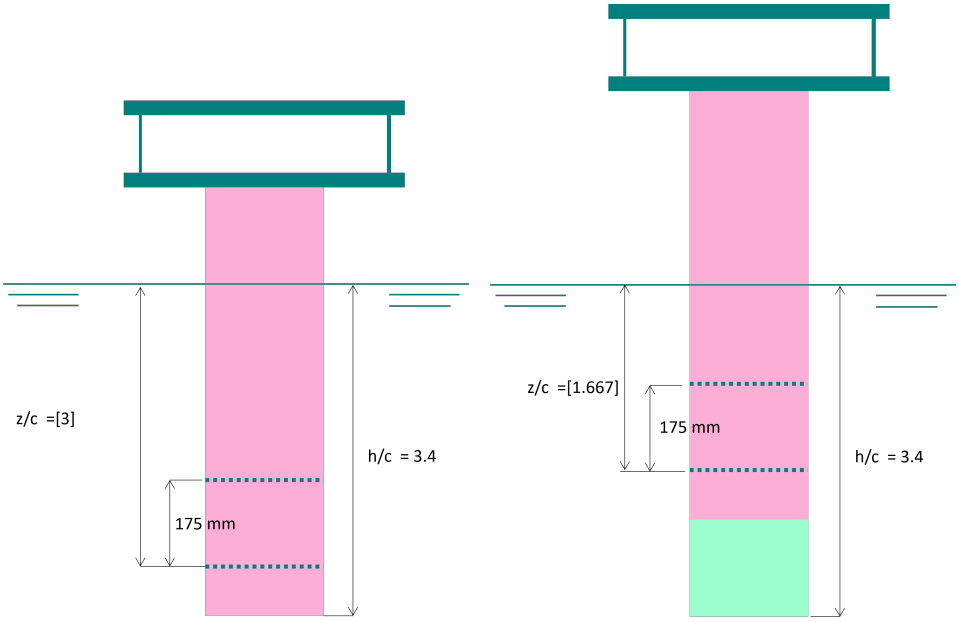

Figure 3.6: Side view of tapping placement with and without extension piece

The tapping placement in chord-wise direction is important to be able to reconstruct the pressure distribution after the measurements. The typical peak in the pressure distribution is expected towards the LE. To capture this tappings are wanted as far forward as possible. To test whether the tappings are in the right place Xfoil is used. This is done by taking the pressure distribution from Xfoil and taking the values at x/c location of the tapping, making a fit of just these 15 tappings should coincide as best as possible with the continuous plot from Xfoil. The result of this is shown in figure 3.7, from which is seen that the chosen tapping locations exist in the pressure peak and thus reconstruction is deemed possible.

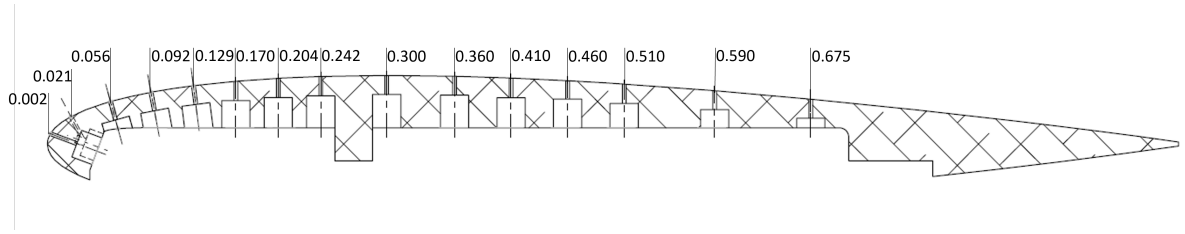

(a) Location of pressure tappings within the foil, distance to leading edge denoted as x/c [-]

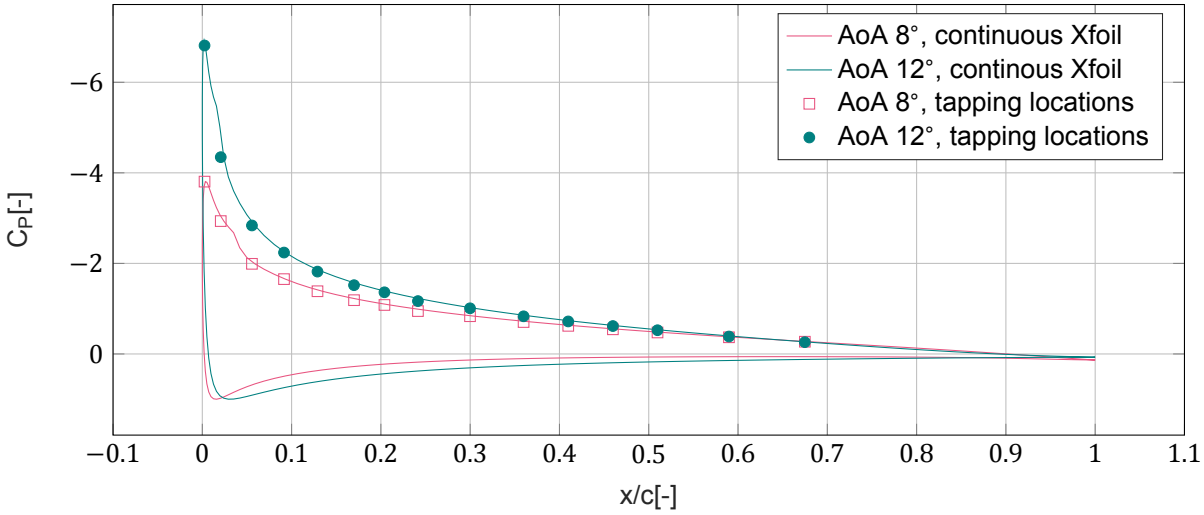

(b) Location of the pressure tappings within a predicted pressure distribution of Xfoil

Figure 3.7: The designed pressure tapping locations inside the foil and on the predicted pressure distribution curve (NACA0012, Re $3.43 \cdot 10^5$). Illustrating the expected results using this tapping sistribution.

The placement of the tappings inside the foil, is done as closely together towards the leading edge as possible whilst maintaining a minimum wall thickness of 2mm. The tappings through the outer surface are 0.4 mm in diameter, and on the inside the diameter is 3 mm, this is because little red 90 °fittings are glued inside the tappings to which the tubes can be connected and led up towards the foil to the pressure sensors.

3.3.4. Mechanical properties

The foil consists of two connecting parts, thus fastening points are required, and to ensure the structural stiffness an I beam-like section is created. The design is a delicate balance between enough wall thickness, structural strength and enough access for a milling machine to make the foil. The final design for the tappings on the inside is shown in figures 3.8 and 3.9.

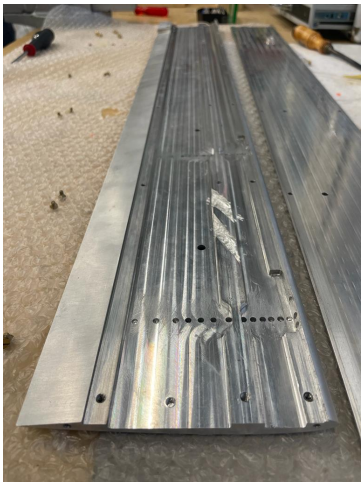

(a) Bare, prepped for assembly

(b) Fitting the connectors into the foil

(c) Tubes glued into the foil

Figure 3.8: Interior of the foil during assembly

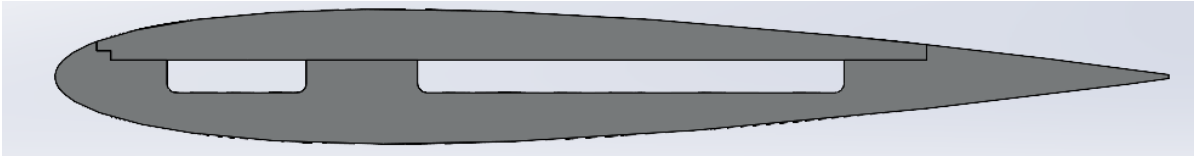

(a) Basic cross section

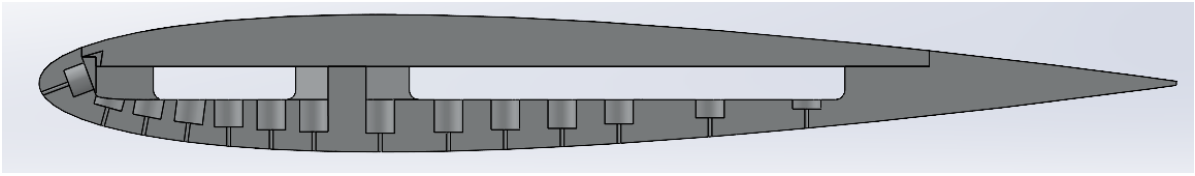

(b) Cross section at pressure tappings

Figure 3.9: Cross section view of foil for overall cross section, cross section for all longitudinal positions of screws and cross section for two longitudinal positions of the tappings

Aluminium-5083, has a density of 2.65 g/cm^3. The volume of the foil is 851 cm^3, the total mass comes to 2.3 kg. The center of mass is at (x,y,z) = (52.05, 0, -36.82) in mm. The transverse center of mass lies in the middle of the foil, the longitudinal center of mass lies 52.05 mm behind the leading edge, which is at 0.43 x/c., the z value is from the waterline if z/c is 3, thus this is 437 mm from the bottom of the foil.

Table 3.4: Mechanical properties of the designed test geometry

	Value	Unit
CoG_x	52.05	mm
CoG_y	0	mm
CoG_z	-36.82	mm
Volume	851	cm^3
Mass	2.3	kg
Ix	14,035	mm^4
Iy	819,189	mm^4
σ_y	195	MPa

3.4. Measuring equipment considerations

During the experiment force and pressure measurements are wanted, thus force and pressure sensors are needed. The force measurements will be carried out using the 6DOF frame facilitated by the TU Delft. The pressure tapping system is made in-house, whilst the pressure sensors are bought of the shelve.

3.4.1. Pressure sensors

The pressure sensors used are SM5420E from Silicon Microstructures. Due to availability, there is a mix of 30 and 60 PSI ranges. These sensors were chosen because of their price and their ability to withstand water. 36 sensors were needed, thus a reasonable price was necessary. The sensors need a supply voltage of 5V, the working principle is a Wheatstone bridge typical output is 70mV.

Figure 3.10: SMi pressure sensors

The pressure sensors are absolute pressure sensors. An attachment piece is made to fit the tubes on the sensor, and to ensure that during handling, the tubes remain in place. The sensors soldered on the PCB are shown in the left picture and the attachment pieces on the sensors are shown in the right picture of figure 3.11.

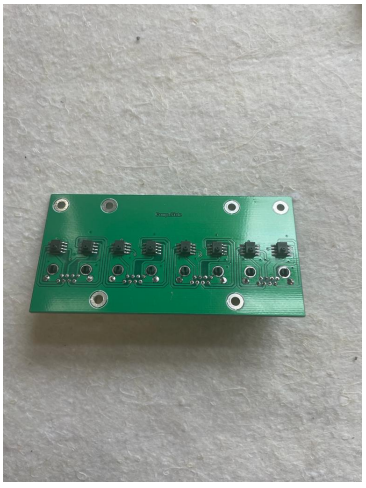

(a) Sensors soldered to PCB

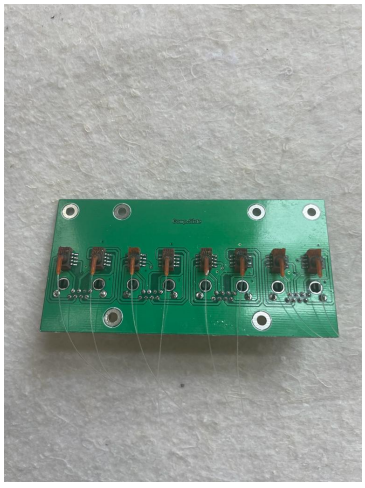

(b) Red attachment fitted on sensors

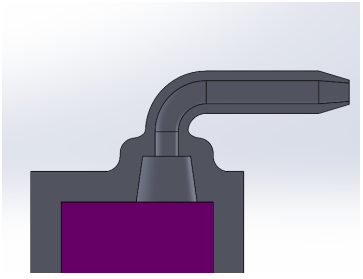

(c) Cross section of the attachment piece

Figure 3.11: Preparation of the pressure sensors to be used in the set-up.

3.4.2. Force transducers

The 6DOF frame has 6 force transducers. One in X direction, 2 in Y direction and 3 in Z direction. Based on the test program and the force predictions that will be made the strength of the force sensor is chosen. The force sensors are placed on the rigid plate of the 6DOF and connected to the plate on which the model is mounted. The transducers are load cells with elastic bands. When placed on the

6DOF frame, they need to be absolutely in-line with their working axis. The placement is done and checked using a square, bevel and laser.

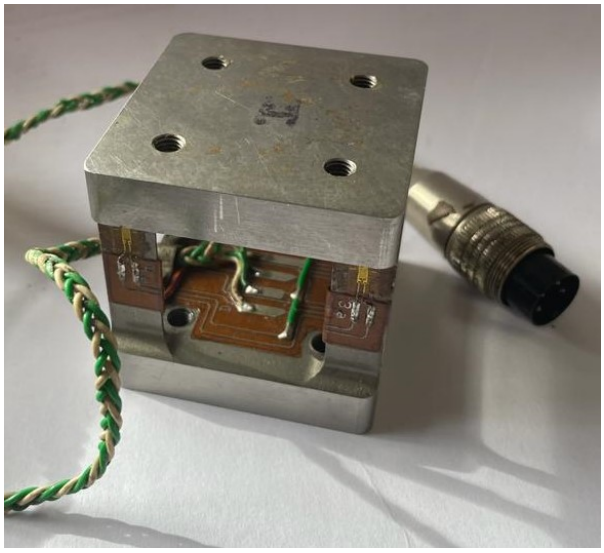

Figure 3.12: Single force transducer depicted to be mounted on to the 6DOF frame

From Xfoil the hydrodynamic coefficients for AoA 0°, 8° and 12° at Re $3.42 \cdot 10^5$ are obtained. The speed for all runs is 3 m/s and the wetted area remains constant, the forces and moment are calculated using equations 3.3.

$$L = \frac{1}{2} \cdot \rho \cdot V^2 \cdot Cl_{xfoil} \cdot A \tag{3.3a}$$

$$D = \frac{1}{2} \cdot \rho \cdot V^2 \cdot Cd_{xfoil} \cdot A \tag{3.3b}$$

$$M = \frac{1}{2} \cdot \rho \cdot V^2 \cdot Cm_{xfoil} \cdot A \cdot c \tag{3.3c}$$

These computed forces are in a coordinate system where the lift is perpendicular to the direction of speed and drag opposite and parallel to the direction of speed. The coordinate system of the 6DOF and the towing tank do not always coincide. Dependent on the operational condition of the foil these need to be transposed. Angles of rotation are yaw (angle of attack) and roll. The forces experienced by the 6DOF can be calculated. Note that the 6DOF rotates with the foil, thus the 6DOF is not in the world coordinate system.

$$Fx_{dof} = D \cdot \cos(AoA) + L \cdot \sin(AoA) \tag{3.4a}$$

$$Fy_{dof} = L \cdot \cos(AoA) - D \cdot \sin(AoA) \tag{3.4b}$$

The centre of effort does not coincide with the centre of the 6DOF frame. Additional moments caused are computed using the following equations:

$$Mx_{dof} = Fy_{dof} \cdot CoE_z \tag{3.5a}$$

$$My_{dof} = Fx_{dof} \cdot CoE_z \tag{3.5b}$$

$$Mz_{dof} = Fx_{Dof} \cdot CoE_y + Fy_{DOF} \cdot CoE_x + M \tag{3.5c}$$

Now all moments and forces in the center of the 6DOF are known. The distance from the centre of the 6DOF to a specific sensor is known. The calculation of the force as seen per sensor are given in

equations 3.6. These distances from center bottom plate to sensor are denoted by the direction and subscript to which sensor, for example x_{F1X} is the distance in x from center bottom plate to the F1X sensor.

$$F1X = Fx_{dof} \tag{3.6a}$$

$$F2Y = \frac{Fy_{dof}}{2} + \frac{Mz_{dof}}{x_{F2Y} \cdot 2} \tag{3.6b}$$

$$F3Y = \frac{Fy_{dof}}{2} + \frac{Mz_{dof}}{x_{F2Y} \cdot 2} \tag{3.6c}$$

$$F4Z = \frac{Fz_dof}{3} + \frac{Mx_{dof}}{y_{F5Z} \cdot 3} + \frac{My_{dof}}{x_{F6Z} \cdot 2} \tag{3.6d}$$

$$F5Z = \frac{Fz_{dof}}{3} + \frac{2 \cdot Mx_{dof}}{y_{F5Z} \cdot 3} + \tag{3.6e}$$

$$F6Z = \frac{Fz_{dof}}{3} + \frac{Mx_{dof}}{y_{F5Z} \cdot 3} + \frac{My_{dof}}{x_{F6Z} \cdot 2} \tag{3.6f}$$

Based on the test program the estimated loads per run and sensor are determined. The sensors are available in 100, 200 or 400 N strength. In figures 3.13, both a scatter and histogram plot are shown. The left hand side scatter plot shows the estimated force on a sensor and the right hand side figure shows the frequency of a value occurring, sorted based on available force ranges of the sensors.

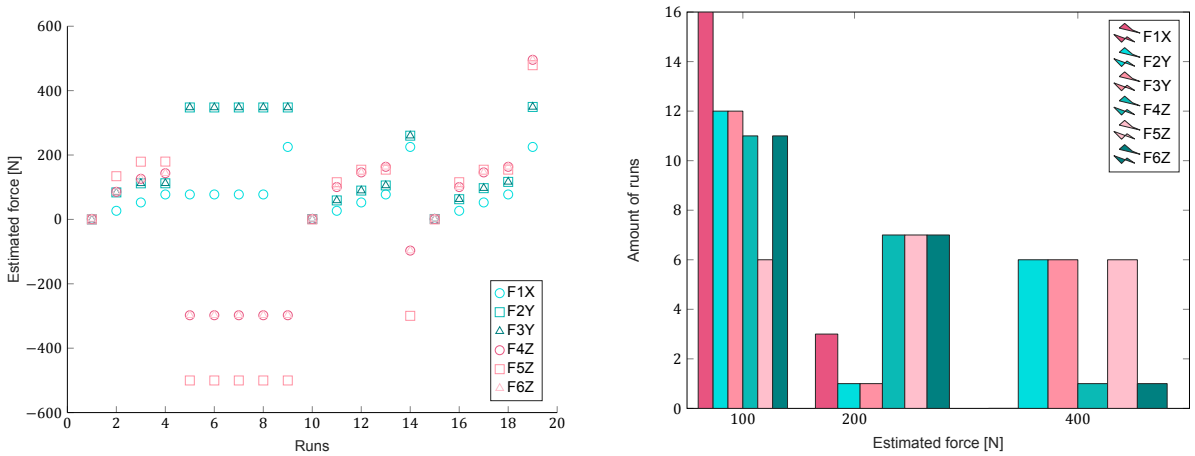

(a) Scatter plot of estimated force on sensor for runs

(b) Histogram of magnitude force on sensor

Figure 3.13: Scatter plot of predicted force on sensors based on test program

The maxima/minima dictate the specific range of the sensor. Looking at the right figure, starting from the right the sensors F2Y, F3y and F5Z have quite high frequency at the 400 N bin and are selected. Then moving to the lower range of 200 N, the F4Z and F6Z have a high frequency here. Lastly the F1X sensor is chosen to be a 100 N sensor.

In the figure 3.13 some values do go beyond the range of the sensor. However most of the runs will be within the range. During experimenting, the sensor response will be monitored. The sensors are known to still respond linearly till 150% of their capacity, thus there is margin for a little overshoot. The chosen sensor ranges are shown in table 3.5.

Table 3.5: Force sensor selection

F1X	200 N	F3Y	400 N	F5Z	400
F2Y	400 N	F4Z	200 N	F6Z	200

3.4.3. Amplifiers

Three types of amplifiers are used in this experiment. For the pressure sensors 36 amplifiers were needed, due to availability using one type was no option. Amplifiers used are the CPJ from Lorenz Messtechnik GmbH, the MA-UI from BMCM and two in-house amplifiers all three shown in figures 3.14.

(a) CPJ (b) MA-UI (c) Made in-house

Figure 3.14: Three types of amplifiers used to amplify pressure sensor signal

The purpose of the amplifiers is to increase the amplitude of the signal. The signal coming from the sensor is very small. This would limit the computer to read and process the signal. Next to the measuring signal, there is also electrical noise captured. If the amplitude of the wanted signal is small, the signal and the noise can get confused. The signal is amplified to a maximum of 10 V to be processed by the computer.

3.5. Total Set-up overview

The foil is mounted to the 6DOF frame with a bracket which allows for the foil to slide up and down manually. The ability for manual vertical translation is a precaution to ensure all operational conditions of the test program can be executed.

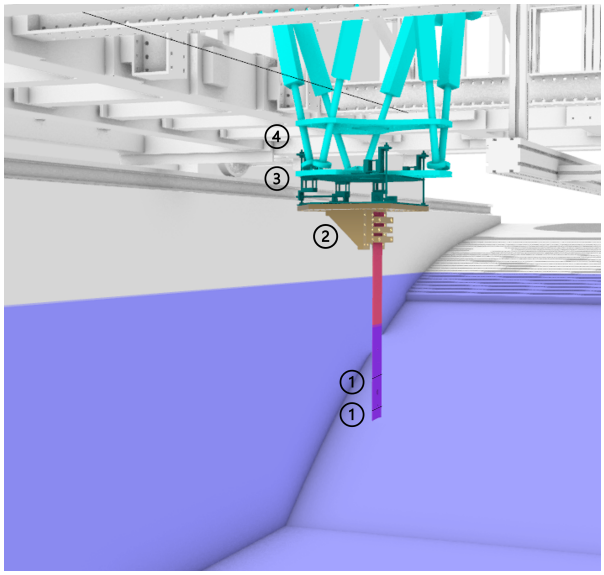

Figure 3.15: Render of foil underneath the carriage. 1) pressure tappings, 2) attachment bracket, 3) 6DOF frame, 4) Hexamove

For set 2, an angled spacer bracket is used, because the Hexamove cannot rotate this far. Using the spacer block, makes full range of freedom also in this condition. Technical drawings of the parts designed for this research can be found in appendix D

In figure 3.16 a schematic overview of all components used during the experiment are shown.

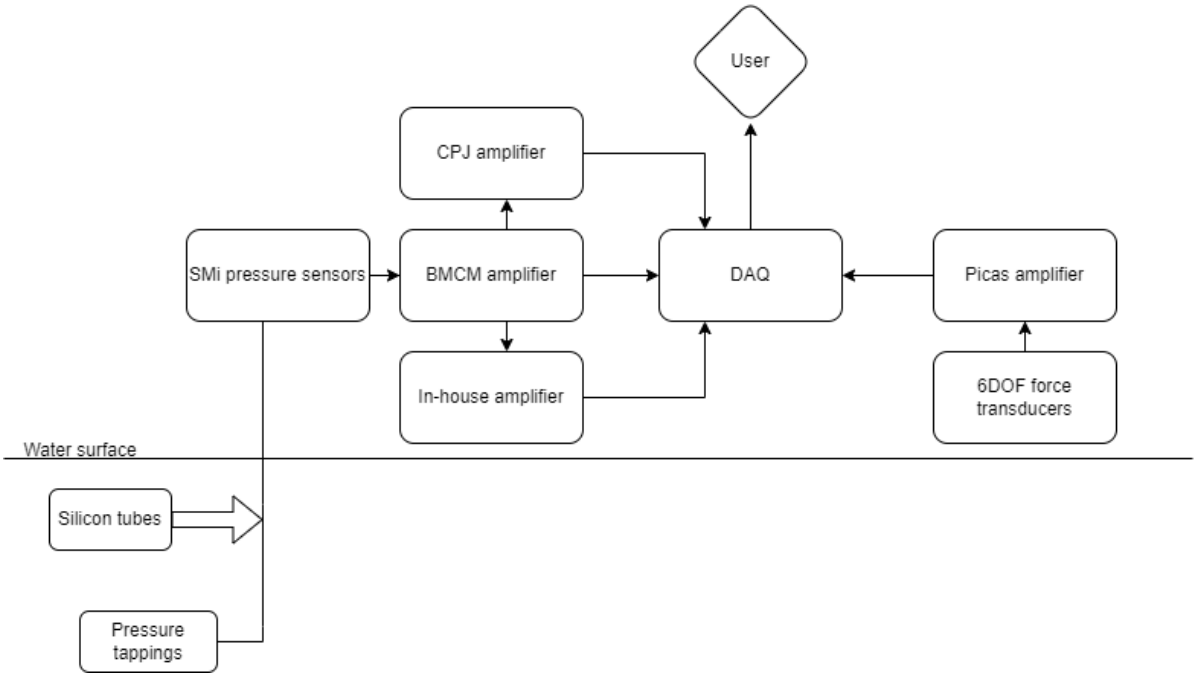

Figure 3.16: Schematic overview of experimental set-up

4

Method - Calibration

The calibration process of both pressure sensors and force transducers is discussed in this chapter. The calibration process for the force transducer is adopted from the towing tank facility. The process and results are depicted in section 4.1. In this experiment, many pressure sensors are used. A method in which all sensors can be calibrated accurately and at the same time is beneficial. Section 4.2 describes the pre-calibration of the pressure sensors, the method used here is a 9m water column. Section 4.3 discusses the re-calibration process, which is executed before each measurement run in the towing tank. The last section is a reflection on the calibration process.

4.1. Calibration force transducers

The forces are measured with the 6DOF frame, which measures all 6 degrees of freedom. It consists of 2 plates mounted on top of each other with 6 force transducers and 6 small connecting rods to make the frame rigid, see figure 4.1. All force transducers are calibrated separately by bolting a hanger to the sensor on a hook and gradually adding weight in steps. Depending on the range of the sensor, the weights are added in steps of 1, 2 or 5 kilos and then removed again. In this way, a roof-shaped signal is obtained. The calibration is executed in the positive and negative direction of the sensor. The signal provided by the sensor is averaged and tabulated along with the corresponding weight per step. When the calibration sequence is complete, the slope can be determined. The slope is already given in newtons per volt, which is the desired ratio for the force calibration factor. Accuracy is also measured as the error between the measured voltage times the calibration factor and the known imposed force (weight). An accuracy of over 98% has been found for all sensors, see appendix E.

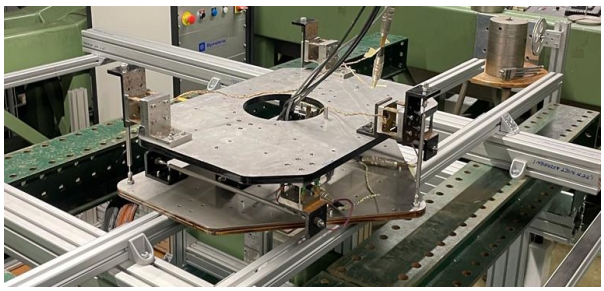

Figure 4.1: 6DOF frame ready to calibrate as a whole to check for any misalignment in the assembly

The frame, as shown in figure 4.1, was assembled after the calibration of each sensor. The frame was tested by attaching weights to a bracket. The bracket was attached to a small rope that was placed in the middle of the 6DOF frame and passed along a wheel that can be seen in the top right corner of the figure 4.1. A laser was used to ensure that the rope ran absolutely level and

perpendicular to the frame. With this set-up, where the 6DOF is assembled and weights are suspended over the x- and y-axis of the frame, it is possible to determine if there is any misalignment in the frame. The expected resulting forces and moments are calculated and compared with the response of the frame. The results of these tests agree. This means that the 6DOF is assembled correctly and can be mounted under the Hexamove.

The 6DOF is checked again after installation on the Hexamove, as a slight angular offset may occur during this process. By letting the Hexamove rotate plus and minus 25° around the X and Y axis and measuring the forces, they should be the same in both directions. No misalignment was detected during this routine.

After the foil was fitted underneath the 6DOF, the entire system is checked again. Since it is possible that the foil is mounted on the 6DOF with a slight angular misalignment. To check this, a few runs were made between -4° and 4°. The resulting forces were not symmetrical over 0° AoA. A misalignment of 0.8° was found, see appendix G to this process. The misalignment was corrected for in the data processing script as described in chapter 5. This misalignment must be taken into account in the rotation matrices, more on this in the next chapter.

4.2. Pre-calibration pressure sensors

The sensors have a typical span of 95 mV over their measurement range. Due to availability, two different ranges are used, either 0-30PSI or 0-60 PSI. The 30 PSI sensor has an output of $4.59 \cdot 10^{-4}$ mV/Pa and the 60 PSI sensor has an output of $2.30 \cdot 10^{-4}$ mV/Pa. Between the sensor and the computer, amplifiers are placed. The three different types of amplifiers have different gains either 50, 100 or 400. Each channel is a combination of a sensor and an amplifier. In table 4.1 the signal that a sensor delivers to the user (computer) is depicted.

Table 4.1: Signal of every sensor as seen by the user

Sensor	$x \cdot 10^{-2}$ [mV/Pa]	Sensor	$x \cdot 10^{-2}$ [mV/Pa]	Sensor	$x \cdot 10^{-2}$ [mV/Pa]	Sensor	$x \cdot 10^{-2}$ [mV/Pa]
P01	2.30	P10	1.15	P19	2.30	P28	2.30
P02	2.30	P11	1.15	P20	2.30	P29	9.19
P03	2.30	P12	1.15	P21	4.59	P30	9.19
P04	2.30	P13	2.30	P22	2.30	P31	9.19
P05	1.15	P14	2.30	P23	4.59	P32	9.19
P06	1.15	P15	2.30	P24	2.30	P33	9.19
P07	1.15	P16	2.30	P25	2.30	P34	9.19
P08	1.15	P17	2.30	P26	2.30	P35	9.19
P09	1.15	P18	2.30	P27	4.59	P36	9.19

The pressure sensors are calibrated with a 9-metre high water column that runs through three floors of the building. There is a water outlet at the bottom of the water column and a water inlet at the top of the column. During a calibration run, the steps correspond approximately to a change in the water column of 1.5 metres. With the ruler placed along the entire column, the intermediate water levels are noted down to the millimetre accurately. Three calibration runs are executed with 3, 4 and 6 steps. The maximum measured difference in the water column is 6.5 metres, which corresponds to a pressure difference of 650 kPa. The sensors are connected to the water column with tubes. These are also the tubes that will be connected to the fittings inside the foil.

The raw response of sensor P32 from a calibration run is shown in figure 4.2. There are distinct steps in this figure. The decreasing sloped line between the steps is the time that the tap at the bottom was opened. As the water column lowers, so does the pressure. The response of the sensor is balanced and has no slope, indicating that there is no leakage and the system is working properly. The spikes in the signal are the opening and closing of the tap, which causes a bounce in the water surface, after which the signal quickly stabilises.

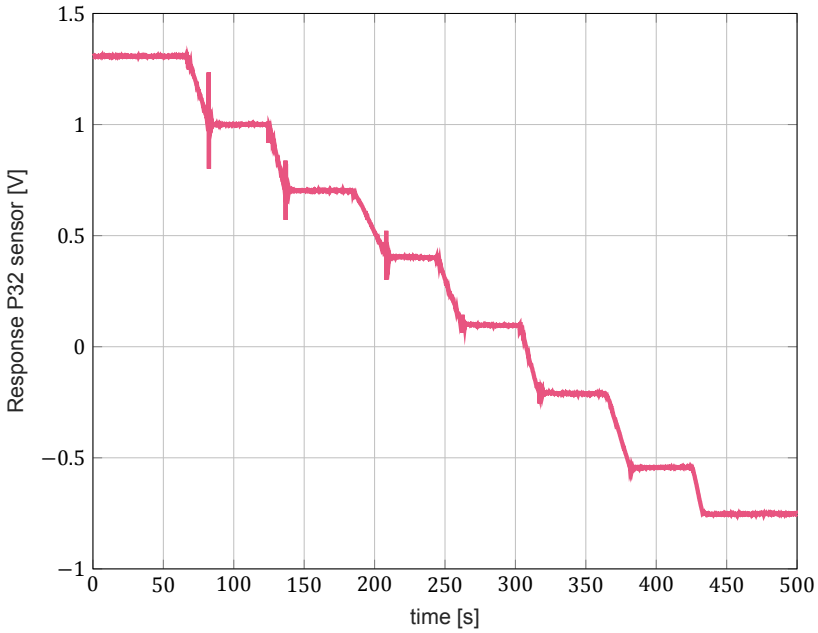

Figure 4.2: Output stepped calibration run

The measured response and the expected response are plotted together to visualise the mismatch in figure 4.3. The expected response is calculated by multiplying the observed height in millimetres by the signal each sensor gives to the user from table 4.1 and then factoring with $9.81 \cdot 10^{-3}$ to obtain the response in voltage. The calibration is relative, not absolute, thus the first measurement point is equalised to the expected response, hence the response at 9010 mm water column is equal.

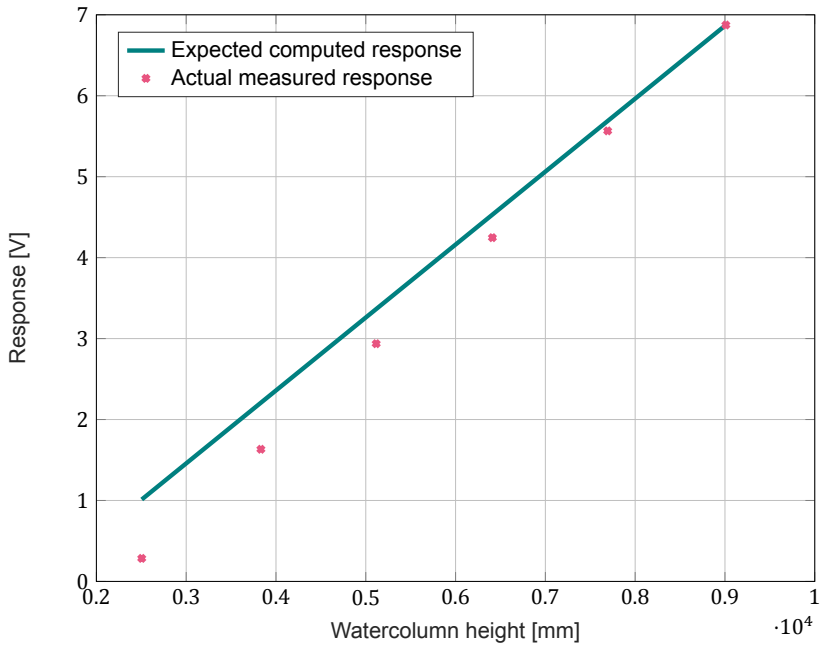

Figure 4.3: Computed expected response and actual measured response plotted against the measured water column height

The actual and expected response do not coincide. This is also not to be expected, as the calibration factor has not yet been imposed on the results. To obtain the calibration factor, the following steps are taken. Using the input voltage and the height in millimetres per step, the slope in V/mm is calculated.

The calibration factor is then determined using equation 4.1. The calibration factor is expressed in Pa/V and converts the sensor voltage into the desired pressure.

$$\text{Calibration factor}[Pa/V] = \frac{9.81}{slope[V/mm]} \tag{4.1}$$

The factor 9.81 in the equation results from the fact that 1 mm water column corresponds to 9.81 Pa. The method for determining the calibration factor is a form of linear regression. An R-squared value can be calculated from a regression. The R-squared value is a number between 0 and 1 that describes how well the data fits a model. In this case, the model is the calculated expected linear line. A value of 1 represents a perfect fit and a value of 0 represents a poor fit. All sensors have an R-squared value greater than 0.99997, result and R-squared values are depicted in F. Considering that electrical components introduce noise, it is safe to say that the sensors show a perfect linear response (see figure 4.2). All calibration factors calculated after these steps can be found in table 4.2.

Table 4.2: Calibration factors off all sensors

Sensor	Pre-Cal_fac [Pa/V]	Sensor	Pre-Cal_fac [Pa/V]	Sensor	Pre-Cal_fac [Pa/V]	Sensor	Pre-Cal_fac [Pa/V]
P01	53,978	P10	84,912	P19	42,758	P28	41,900
P02	43,626	P11	89,488	P20	41,869	P29	11,063
P03	44,034	P12	84,112	P21	80,587	P30	10,665
P04	44,851	P13	40,581	P22	44,540	P31	10,901
P05	87,374	P14	40,864	P23	80,357	P32	9,687
P06	84,491	P15	41,126	P24	42,769	P33	10,633
P07	86,430	P16	41,271	P25	42,689	P34	11,935
P08	88,919	P17	40,140	P26	42,091	P35	11,346
P09	84,511	P18	39,765	P27	80,475	P36	11,430

Now the calibration factors are known figure 4.3 can be redrawn factored for the calibration factor. In figure 4.4 the two are plotted again. Now the lines over-lay each other perfectly. Calibration clearly has been carried out correctly.

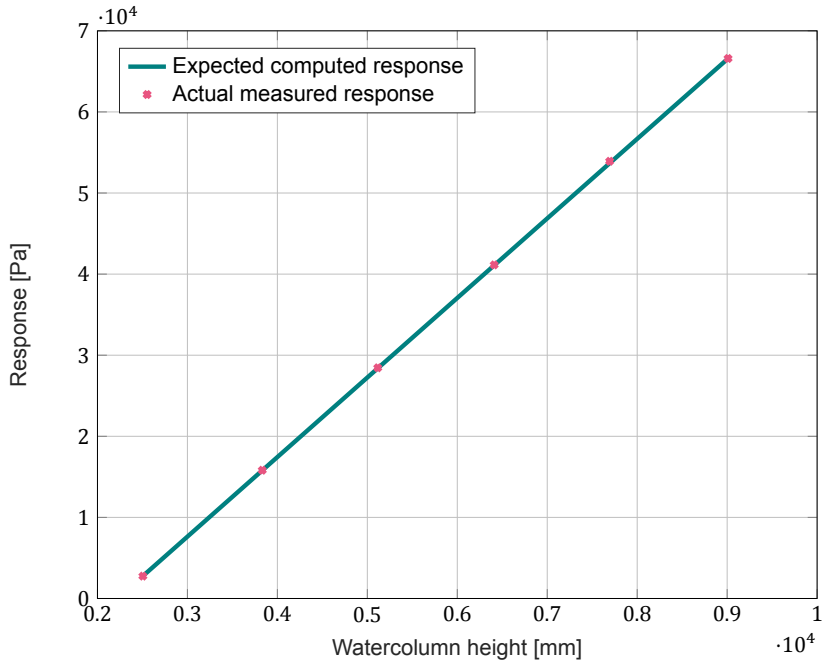

Figure 4.4: Measured response and expected response after calibration plotted against the measured water column height

The calibration set up is dismantled and the sensors are connected inside the foil. The sensors are

attached to the fittings inside the foil. The placement of the sensors from LE to TE are for the upper array:

$$P01 \;\; P32 \;\; P03 \;\; P04 \;\; P05 \;\; P06 \;\; P07 \;\; P08 \;\; P09 \;\; P31 \;\; P34 \;\; P12 \;\; P13 \;\; P14 \;\; P15$$

and for the lower array:

$$P16 \;\; P17 \;\; P18 \;\; P19 \;\; P20 \;\; P21 \;\; P33 \;\; P23 \;\; P24 \;\; P25 \;\; P26 \;\; P27 \;\; P28 \;\; P29 \;\; P30$$

.

4.3. Re-calibration of pressure sensors

During the actual experimental runs in the towing tank, stepped runs are carried out. These stepped runs are executed for the vertical configuration only. The stepped run is carried out between the null-run and the test-run. During a stepped-run, the carriage stands still and the model is translated in 40-mm steps from z/c 1.67 to z/c 3. This was originally done to check that all sensors were working satisfactorily before each run. Because the pressure tappings and tubes are prone to a little debris or small air entrapment. In addition, these stepped results give the ability to perform a re-calibration. The pressure range over which is tested, is much smaller than in the initial calibration, but the conditions of the system are more realistic. Meaning that the set-up is finalised: the tubes will not change in length and the water pressure now comes through a 0.4 mm tapping instead of a large hose.

Time has passed between the calibration outside the tank and these stepped runs inside the tank. The sensors and tubes have been glued and mounted on and in the foil. This can have caused a sensor to become faulty, a connection to leak or a tube to be clogged. Therefore, the stepped runs are first used to determine whether a sensor is working or not. Figure 4.5 shows the data output of a stepped run, the left sensor P08 and the right sensor P32 4.5b. A defective sensor can be easily detected and once detected removed from the data set. The sensor P32 that is working properly has a linear response. The green curve is the response, and the red segments indicate the length of the data sample averaged for each step.

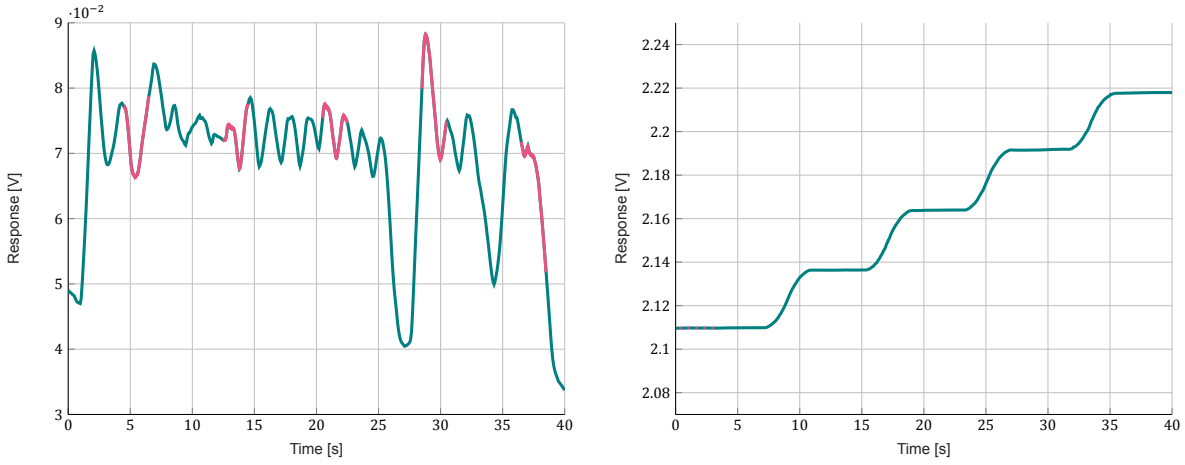

(a) Response of sensor P08, clearly faulty

(b) Sensor P32, working

Figure 4.5: Response of pressure sensors during a static stepped run

The same procedure as in the pre-calibration is now executed. The expected response is calculated using the known relative water depth (40mm increments) and plotted against the actual measured value in figure 4.6. The expected response is computed by equalising the first measurement (that is here at 0 mm relative submergence). Then the expected response is a linear line with a slope equal to 9.81 Pa/mm. The measured data is corrected using the calibration factors as shown in table 4.2.

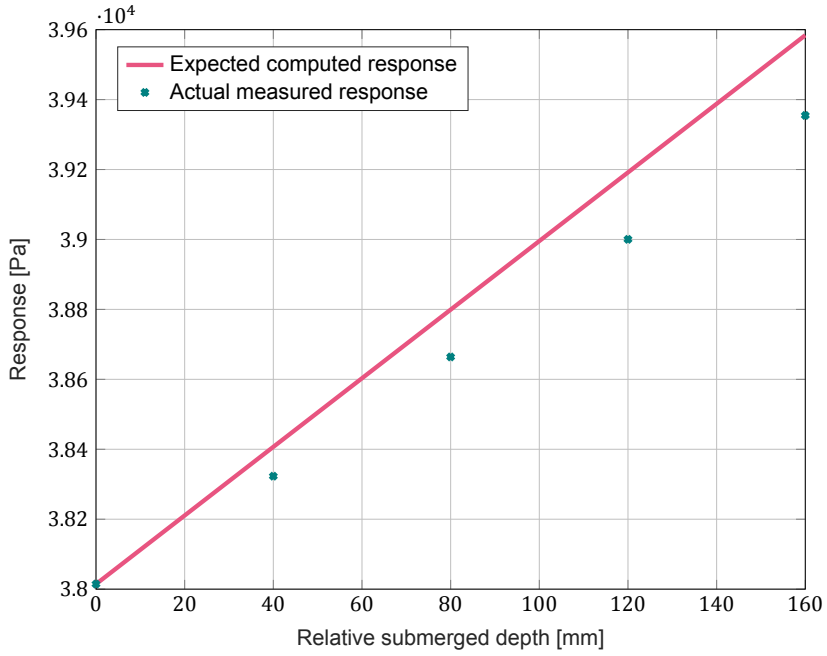

Figure 4.6: Measured response and expected response plotted against relative draft during stepped run, using pre calibration factors

The expected and actual values do not coincide. Between the period from pre-calibration to re-calibration a maximum difference in atmospheric pressure of 350 Pa is found (“Amsterdam Airport schiphol”, 2022). If in figure 4.6 a 350 Pa error band would be drawn around the expected computed response, the actual measured points would fall within the error band. Apart from the change in set-up, the change in atmospheric pressure also played a role. The calibration factor as determined in the pre-calibration is not completely satisfactory due to environmental factors and thus validating the importance of the re-calibration procedure.

Based on the stepped runs of all sensors, the calibration factor can be found in the same way as in the previous section. The height does not need to be noted, since the imposed height difference between each step is known 40 mm. For perfect conditions, no interference by the surroundings, the calibration factor of a specific sensor should be the same for all runs. This is however not the case. The calibration factors per run do differ, probably due to slight movement of the flow within the tank. The calibration factors found per sensor of the stepped runs are processed into a box-plot, see figure 4.7. The figure shows the median in light pink and the mean with a darker cross. The box marks the 25th to 75th percentile, and the whiskers mark the extreme calibration factor values. A wide box-plot indicates a lot of variation in the calibration factor. A narrow box-plot indicates a more constant calibration factor value.

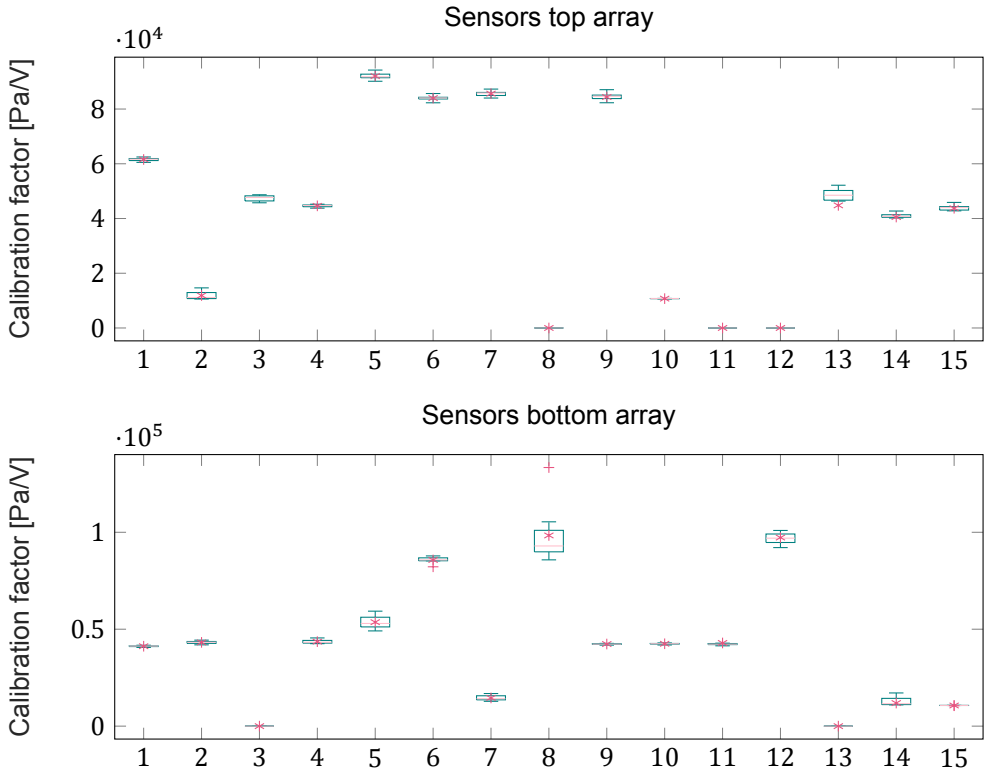

Figure 4.7: Box-plot showing variation of calibration factor per sensor for all stepped runs, stars indicate average value used

All sensors at 0, are faulty. The other sensors have a very narrow box, all computed calibration factors lie close togehter. The only exception is the sensor of the lower array at position 8, where the deviation is large. This is due to the one outlier denoted by a $+$. This outlier is a result of the first stepped run of the day. Every morning all sensors were bled to ensure that there were no air bubbles in the tubes. However, it could be that this step was overlooked.

The change in calibration factor per run is small. The maximum deviation from the averaged calibration factor is within 5%. The atmospheric pressure fluctuations might have played a role in the fluctuations. Within the period of the experiment, and thus the period of all re-calibration data, the maximum atmospheric pressure difference was 170 Pa (“Amsterdam Airport schiphol”, 2022). Looking at figures 4.7, this small fluctuation of ambient pressure would not have influenced the resulting averaged calibration factor. To provide greater continuity throughout the experiment the average calibration factor will be used in the post-processing of all data. These calibration factors can be found in table 4.3. Any sensor for which no calibration factor is given is either not functioning satisfactorily or is defective.

Table 4.3: Re-calibration factors off all sensors

Sensor	Re-Cal_fac [Pa/V]	Sensor	Re-Cal_fac [Pa/V]	Sensor	Re-Cal_fac [Pa/V]	Sensor	Re-Cal_fac [Pa/V]
P01	71,820	P10		P19	43,521	P28	46,638
P02		P11		P20	47,237	P29	11,912
P03	46,891	P12		P21	88,903	P30	10,652
P04	46,410	P13	44,802	P22		P31	10,722
P05	98,802	P14	40,545	P23	89,328	P32	11,509
P06	85,068	P15	43,749	P24	42,352	P33	14,549
P07	91,978	P16	41,932	P25	42,485	P34	
P08		P17	43,758	P26	42,903	P35	
P09	84,412	P18		P27	97,273	P36	

The pre- and re-calibration factors (tables 4.2 and 4.3) have a minor change for some sensors, with averaged difference of 6% and maximum difference of 26%. The difference can be caused by change in tube length, influence of the pressure tapping diameter, a minor air entrapment. With these new calibration factors the expected response can be overlaid with the measured response again, now the measured response is factored by its new calibration factor. The result of this is plotted in figure 4.3.

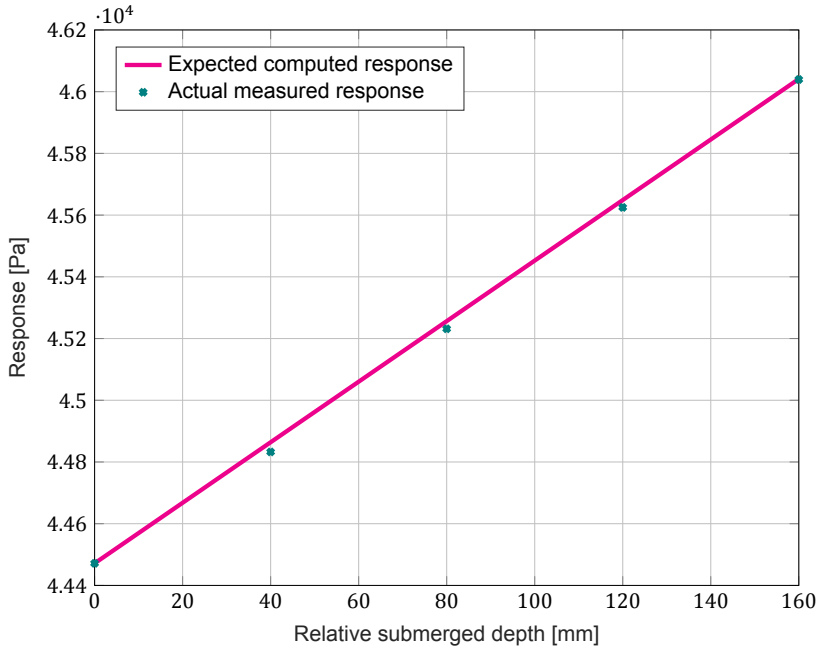

Figure 4.8: Measured response and expected response plotted against relative draft during stepped run, using re-calibration factors

Figure shows the measured data points are either on the expected regression line or very close, the biggest error is 0.6%. This error is deemed small enough, to say the re-calibration process was successful.

4.4. Reflection on calibration process

The calibration of each force transducer is done correctly. It is a simple method where not a lot can go wrong. The calibration of the assembled 6DOF, made sure that there was no misalignment after mounting everything together. When this showed to be correct the 6DOF was mounted underneath the Hexamove. A rotation of plus and minus 25° was used to check for any misalignment here. What has not been done is, imposing oscillating surge and sway motions to check for misalignment. At this stage, the rotation procedure was considered sufficient. If the experiment were to be repeated, it would be advisable to also perform the oscillating movements to be extra sure of the alignment.

There is a difference in accuracy between the actual and measured response in pre- and re-calibration (figures 4.4 and 4.3). The pre-calibration is more accurate. However, it is conceivable that this precise accuracy is not feasible in the towing tank. The pre-calibration is performed with a water column in a small, closed and controllable environment. Recalibration takes place in the tank. There is a greater chance of disturbances here. The vibration of the carriage, due to people working next to the tank, may slightly change the pressure reading. A possible residual flow velocity in the water of the tank also affects the reading. Even though a 20-minute waiting period was imposed between runs. These factors make the results not 100% accurate.

Note that calibrating the force sensor involved deleting a zero measurement. This means that the weight of the hanger itself is deleted and the results are absolute values. The pressure measurement calibration, on the other hand, does not involve an absolute measurement. It is based on the relative

difference. This is fine for the intended use of extracting the pressure coefficient.

One could argue that the pre-calibration has been of no use since these results are not being used in the end. However, it is an insightful step, since performance over the full range of sensors can be tested. Whereas inside the towing tank, only a small portion of the range can be tested. In this research these pressure sensors were used for the first time, so the pre-calibration was also a test to see if they were all working and how good.

5

Method - Data processing

In this chapter the data processing is explained. In the first section an evaluation of the data sample is given, by looking at the standard deviation. The evaluation of whether the data is useful is the first step of data processing. Before computations are done, all data is trimmed to match the operational condition that it is correlated with. Then the null-measurement is subtracted from the test-run. This way initial gravitational forces are not included in the data. For the pressure coefficient, this null-measurement resembles the free stream pressure value. Of the time-dependent response a moving average is taken. For the static runs, the mean value of the run data is taken. No special filtering is deemed necessary since the noise on the raw data is small and the response is static. Some dynamic sweeps are carried out as well. Since these results are time-dependent a moving average is taken. A more complex filtering technique does not improve the quality of the result. Because the sweep is intentionally carried out at such a slow angular speed that the measurement remains quasi-static.

In the second section, the post-processing of the force measurements is explained, to obtain the lift and drag forces. In the third section, the same is done for the pressure measurements. The post-processing of the pressure data includes the method of choice for the curve fitting to obtain the pressure distribution reconstruction.

5.1. Statistics on the sampled data

To express the error of the data sample the standard error (SE) is computed. The standard error expresses the precision of the measurement. Based on the plotted responses seen in chapter 4, the measurements look linear. The data depicted in this section is the raw data (response in V), of sensor P32 pre-calibration step 1 (see figure 4.5b). The data sample used is from second 1 to 60, this gives a data set of 60,001 samples (N). The mean (μ) response of this data set is 5.3979 V. In figure 5.1 the data is plotted in a histogram.

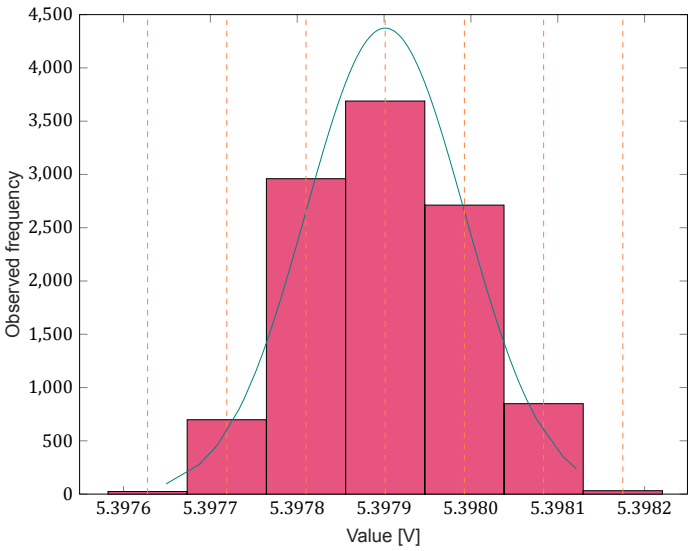

Figure 5.1: Histogram of data set, showing the data has a centred distribution, including the σ boundaries, results of first step shown in figure 4.5b for sensor P32

The standard deviation (σ) is a parameter which indicates whether all samples of a data set are close to the mean, or widespread from the mean. The formula to compute the standard deviation is given in 5.1, in which N is the number of samples, x_i the value of a data sample and μ the mean of all data samples.

$$\sigma = \sqrt{\frac{\sum_{i=1}^{n} (x_i - \mu)^2}{N}} \tag{5.1}$$

The standard deviation of the data set is $9.1214 \cdot 10^{-5}$, meaning the data set is very close to the mean of the data. Based on the histogram in 5.1 the data is assumed normally distributed. In this figure, the normal distribution is depicted as well, alongside one standard deviation bands in dashed lines. A few samples are found beyond the 3σ bounds seen in the most outward bins of the histogram. Again an indicator that all samples are really close to the mean. The standard error is computed lastly, which is the standard deviation divided by the number of samples squared. The error is $3.6055 \cdot 10^{-7}$, very low. For any random run selected from the experiment, the data shows a normal distribution as well. For example the standard error of sensor at T1 (P01), from a run at 0°roll and 8° AoA is 0.0841, with a mean of $7.47 \cdot 10^{4}$. The standard error is also very small, the large difference in standard error, is because the calibration factor has been imposed on this data sample before saved to the computer. The standard error is not dimensionless and the calibration factor is approximately 70,000 causing this difference. The sampling error computation gives insight into the quality of the measurement (the signal). It is found that the standard error is small, and only few sampling points fall outside the 3σ bounds.

5.2. Process to obtain lift and drag coefficients

The incoming force data is a time-trace of the response per force transducers. These six incoming forces are; F1X, F2Y, F3Y, F4Z, F5Z and F6Z. The goal is to compute the lift and drag coefficients. Measured forces of the sensors in the same direction are added together to obtain FX, FY and FZ force.

The measurement is in the coordinate system of the 6DOF, meaning the forces need to be rotated to the required coordinate system for analysis. The coordinate system in which the results will be presented is the pink coordinate system shown in figure 5.2, the coordinate system in which the force is measured is denoted by the teal arrows in the same figure. It is chosen to express the lift force in the Y axis, since this is perpendicular to the foil surface and the pressure measurements are also

measured perpendicular to the foil surface. This way the force in Z direction should be around zero since for a surface piercing strut there is little to no force acting in that direction. The Z axis is along the span of the foil, the Y axis is perpendicular to the foil and perpendicular to the direction of speed, the X axis is along the direction of speed and parallel to the water surface.

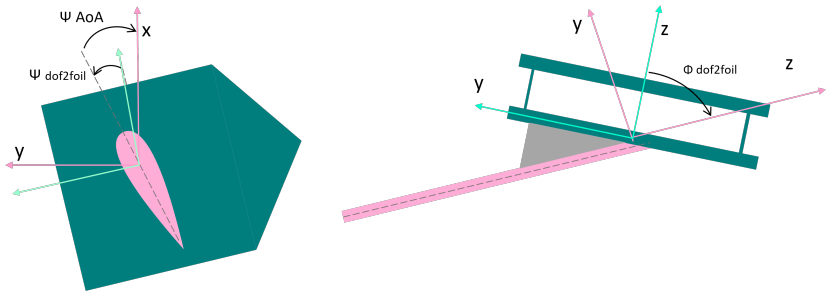

Figure 5.2: Graphic showing rotation of correction angles and operational condition

In figure 5.2 the rotation around Z axis $\psi_{dof2foil}$ and the angle around the X axis $\phi_{dof2foil}$ are noted. These are the correction angles, the first coming from the misalignment in experimental set 1, and the latter is the angle due to the angled bracket in experimental set 2. For post processing, runs of set 1 have a $\psi_{dof2foil} = 0.8°$ and set 2 an angle $\phi_{dof2foil} = 60°$. More on the misalignment of set 1 and how this was found is depicted in appendix G.

First the rotation matrix of the correction angles is imposed on the force vector, see equation 5.2a. Equation 5.2b shows the rotation used for experiments of set 1 and equation 5.2c for experiments of set 2. The result is an intermediate force vector.

$$\vec{F}_{intermediate} = \mathbf{R}_{6DOF2foil} \cdot \vec{F}_{6DOF} \tag{5.2a}$$

$$\vec{F}_{intermediate} = \begin{bmatrix} \cos\psi_{dof2foil} & -\sin\psi_{dof2foil} & 0 \\ \sin\psi_{dof2foil} & \cos\psi_{dof2foil} & 0 \\ 0 & 0 & 1 \end{bmatrix} \cdot \vec{F}_{6DOF} \tag{5.2b}$$

$$\vec{F}_{intermediate} = \begin{bmatrix} 1 & 0 & 0 \\ 0 & \cos\phi_{dof2foil} & -\sin\phi_{dof2foil} \\ 0 & \sin\phi_{dof2foil} & \cos\phi_{dof2foil} \end{bmatrix} \cdot \vec{F}_{6DOF} \tag{5.2c}$$

Now the force can be rotated to its final coordinate system by rotating along the Z axis, with the value of the angle of attack of the corresponding run. This final rotation is shown in equations 5.3.

$$\vec{F} = \mathbf{R}_{AoA} \cdot \vec{F}_{intermediate} \tag{5.3a}$$

$$\vec{F} = \begin{bmatrix} \cos\psi_{AoA} & -\sin\psi_{AoA} & 0 \\ \sin\psi_{AoA} & \cos\psi_{AoA} & 0 \\ 0 & 0 & 1 \end{bmatrix} \cdot \vec{F}_{intermediate} \tag{5.3b}$$

Now that the lift and drag forces are computed, the corresponding lift and drag coefficients are computed using equations 2.5

5.3. Process to reconstruct the pressure distribution

Of the incoming data from the pressure sensors the average value per operational condition of each sensor is noted. These values are sorted and placed in matrices per conditions at the correct span and chord-wise position. The goal is to obtain the pressure coefficient per measured location and operational condition. The subtraction of the null-measurement from the data is already the first step in computing the pressure coefficient, in which the null-measurement is the free stream pressure measurement. There is no need for any rotation of the data, because the measurements are from the pressure tapping directly on the foil. Equation 2.2 shows the equation used, in which P is the measurement and P_∞ is the null-measurement. The velocity is always 3 m/s and the density of the water is 998.86 kg/m^3

This the post processing of the discrete data points. To make a continuous pressure reconstruction, curve fitting is used, based on the obtained data points. Fitting of the data points can be done in multiple ways. It is chosen to fit using the least square method (LSQ). This method yields a smooth curve whilst trying to minimise the error to every measured data point. Required is an anomalous function to fit the data and an initial guess of the magnitude of the coefficients of said equation. The fitting of the data is kept as close to the data points as possible, since this is a research into the quality of the measurements.

Linear least square method will find the global minimum of squared errors and thus the best fit. With the nonlinear least squares method, it is possible that a local minimum of the squared errors is found, but not the global minimum. Therefore linear system is favourable over nonlinear, however it could be that the behaviour of the pressure distribution can only be caught using a nonlinear equation. To find the right assumed equation, several are tested on the data. In equations 5.4 the tested equations are shown. The functions are a form or combination of polynomials, exponential and pade approximation function. A pade approximation is a rational function of a certain order. A rational function is a polynomial divided by a polynomial and is able to express more diverse behaviour than regular polynomials. Here the order is 2 for the numerator and 3 for the denominator. The double exponential function is a nonlinear system, thus extra care must be taken in the analysis of these results.

$$f_{pol}(c,x) = c_1 + c_2 \cdot x^{-2} + c_3 \cdot x^{-1} + c_4 \cdot x \tag{5.4a}$$

$$f_{polexp}(c,x) = c_1 - c_2 \cdot x^{-1} + c_3 \cdot exp(c_4 \cdot x) \tag{5.4b}$$

$$f_{2exp}(c,x) = c_1 * exp(-c_2 \cdot x) + c_3 \cdot exp(-c_4 \cdot x) \tag{5.4c}$$

$$f_{pade23}(c,x) = \frac{(c_1 \cdot x^2 + c_2 \cdot x)}{(c_3 \cdot x^3 + c_4 \cdot x^2 + c_5 \cdot x + c_6)} \tag{5.4d}$$

To test the different functions first discrete Xfoil data is used. In which the pressure coefficient values are taken from Xfoil at the locations corresponding to the pressure tappings on the test geometry, like in figure 3.7. Every function that leads to a residual norm above 1 is eliminated. This leaves the double exponent and the PADE23 function. The fit is also tested on several measurements obtained from the experiments. From this was found that when the first data point is lower than the second data point, the double exponent fit is unable to produce a fit with a resnorm under 1. The PADE23 function is able to do so. Using the pade function as the anomalous function in the LSQ method leads to the minimum residual norm overall data sets. This is for the chord-wise pressure distribution.

To obtain the full surface pressure plot, the data must be fitted in span-wise direction as well. Over the span the assumed shape equation is a cubic function, described in the equation below.

$$f(x,y) = x_1 \cdot y^2 + x_2 \cdot y + x_3 \tag{5.5}$$

Following the above described procedure can yield the following results. Discrete data points, chord-wise pressure distributions along several span-wise locations and a full surface pressure plot.

6

Results

In this chapter, the results, analysis and a short discussion are given. The results in this chapter are from the test program shown in table 3.1. The aim of this chapter is to provide a basis to answer the sub-questions, which will lead to the answer on the main research question in the conclusion chapter.

In the first section, the repeatability of the method is verified. Repeat runs are collected of which the resulting data is compared to each other on sensor level and array level. A cross-check between the upper and lower pressure array is made as well. From this, the level of precision of the measured values is obtained using the percentage difference.

The aim of the second section is to provide the results of the vertical configuration. Which can be used to compare with known data, and thus verify the quality of the method. This is done using the results from set 1, the vertical configuration. Since both positive and negative angles of attack are run, a full surface pressure reconstruction can be made of both the pressure and suction side of the foil. From this pressure reconstruction, the 3D lift coefficient is obtained which is compared to the measured force data, empirical and numerical methods.

The third section contains the results of set 2, which is the high-rolled configuration of the surface-piercing hydrofoil. Here only the positive angles of attack are run, meaning only a suction side pressure reconstruction can be made. The aim is to show with these results, the capability of the method in high-rolled operational conditions.

There were two runs in which ventilation occurred, these are shown in section four. The aim of this section is to provide the basis for an answer to whether or not there is an indication found in the pressure measurements which can correlate to ventilation.

6.1. Repeatability of the pressure measurements

6.1.1. Precision of the pressure sensors during experiment

The results in this subsection originate from set 2. They are from two repeat runs at 60° roll angle and 12° angle of attack. The span-wise locations of the measurements are z/c=0.21 for the upper array and z/c=1.67 for the lower array. The results are given in figures 6.1.

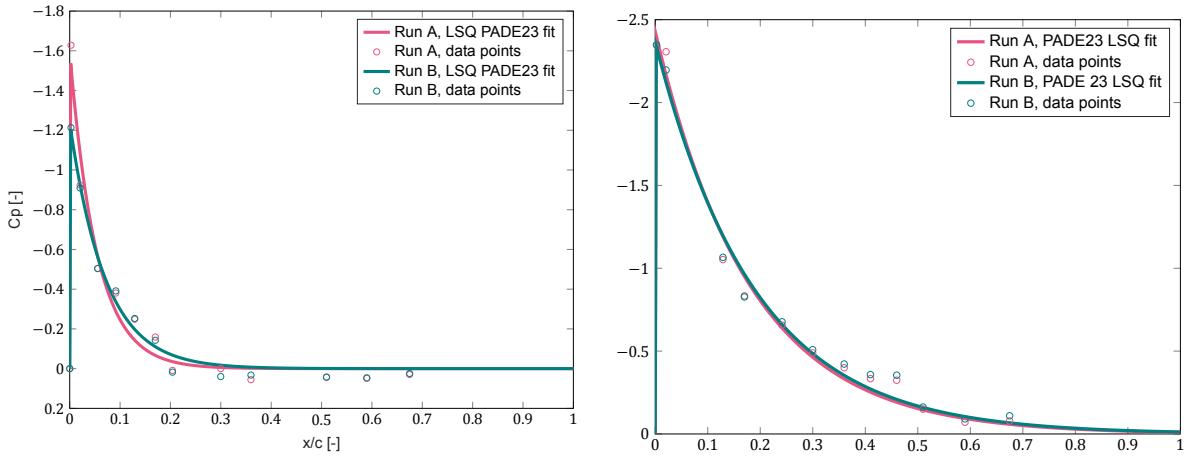

(a) Span-wise location z/c=0.21, upper array

(b) Span-wise location z/c = 1.67, lower array

Figure 6.1: Suction side pressure distribution at two span-wise locations from a run at 60° roll and AoA 12°. NACA0012 surface-piercing hydrofoil, AR 3.46, Re $3.42 \cdot 10^5$.

At first glance, the pressure distributions look to coincide. To be certain the discrete measuring points are depicted, together with the percentage difference between the measured values, in table 6.1. The percentage difference indicates the level of precision of the data.

Table 6.1: Results of 2 repeat runs, including percentage difference of the sensors. Measured at AoA 12°, 60° roll angle. For a NACA0012 surface-piercing hydrofoil, AR 3.46, Re $3.42 \cdot 10^5$

	Upper	array		Lower	array	
location	run A	run B	diff	run A	run B	diff
T1	-1.628	-1.213	29%	-2.348	-2.347	0%
T2	-0.925	-0.909	2%	-2.307	-2.196	5%
T3	-0.505	-0.504	0%			
T4	-0.381	-0.391	3%	-1.039	-1.046	1%
T5	-0.249	-0.252	1%	-1.052	-1.066	1%
T6	-0.159	-0.143	11%	-0.833	-0.827	1%
T7	0.009	0.018	67%			
T8				-0.657	-0.677	3%
T9				-0.489	-0.508	4%
T10	0.055	0.032	53%	-0.400	-0.422	5%
T11				-0.334	-0.358	7%
T12				-0.324	-0.355	9%
T13	0.044	0.042	4%	-0.150	-0.162	8%
T14	0.049	0.046	5%	-0.071	-0.091	25%
T15	0.030	0.024	19%	-0.078	-0.110	33%

First looking at the upper array the difference is significant at locations T1, T6, T7, T10 and T15. This is 5 out of 11 pressure sensors, this is almost half of the sensors of an array. A significant difference is one of more than 5% difference, this value of measurement error is copied from Jentzsch (Jentzsch et al., 2021). At T15, the percentage difference is a lot, but for pressure reconstruction and ventilation indicators, this location is of little importance. The same can be said of T10, although its magnitude has a little more impact on the total pressure distribution. A difference of 29% at location T1 is worrying. The pressure peak is important both to be able to indicate the ventilation cause and to compute the hydrodynamics. Looking at figure 6.1a, both pressure curves do lie very close together. In further computations it is expected this large difference in measurement at T1 will not influence too much. Of the upper array, the rest of the sensors close to the LE do have a negligible percentage difference.

Second, the lower array has a significant percentage difference only for the five last sensors towards the middle and trailing edge. The last two sensors do have a high percentage difference, however, the importance of these locations is less and the absolute difference is not a lot. The small measuring error towards the LE make that the lower array is deemed to work satisfactory.

The rather low precision of more sensors of the upper array compared to the lower array can be a cause of free-surface proximity. Close to the free-surface there are more disturbances. Based on this sensor level precision check, the upper array does not perform sufficiently, the lower array is satisfactory.

A comparison based on total array is made as well. For this the suction side contribution to the lift coefficient ($C_{L,S}$) is computed.

$$C_{L,S} = cos(\alpha) \cdot \int -Cp_s d(x/c) \tag{6.1}$$

Table 6.2: Suction side lift contribution ($C_{L,S}$) per array for repeat run at AoA 12°, for 60° roll angle. NACA0012 surface-piercing hydrofoil, AR 3.46, Re $3.42 \cdot 10^5$.

	Run A	Run B	Difference
Upper array	0.082	0.084	2.5%
Lower array	0.426	0.4336	1.8%

The lower array has a higher precision than the lower array. This was to be expected knowing the difference at sensor level was more towards the LE for the upper array and more towards the TE for the lower array. Based on this result, the precision of the measurements is high enough and the method is repeatable. However, the sample data is very slim. Only two repeat runs are executed. This means the accuracy of the measurements can not be judged. The accuracy of the measurements is partly covered by the calibration process. however, this was a relative calibration meaning the accuracy can still be off. To gain more confidence in this conclusion more repeat runs should be executed. The higher difference for the upper array can be a cause of free-surface proximity. The flow here is less constant than deeper submerged, therefore a 2.5% difference is actually thought to be small.

6.1.2. Cross checking upper and lower pressure array

The results in this subsection originate from set 2. The results are from the operational condition of 60° roll angle and 8° and 12° angle of attack. The results from the upper array are given at span-wise location z/c = 1.54 and the lower array at z/c = 1.67. The measurements are thus collected not at exactly the same location, the absolute difference is 15 mm. Still these results are able to give an indication of the potential differences between the two arrays. The results originate from different runs. Thus some minor errors due to different environmental disturbances can exist. The obtained pressure distributions from these results are given in figure 6.2.

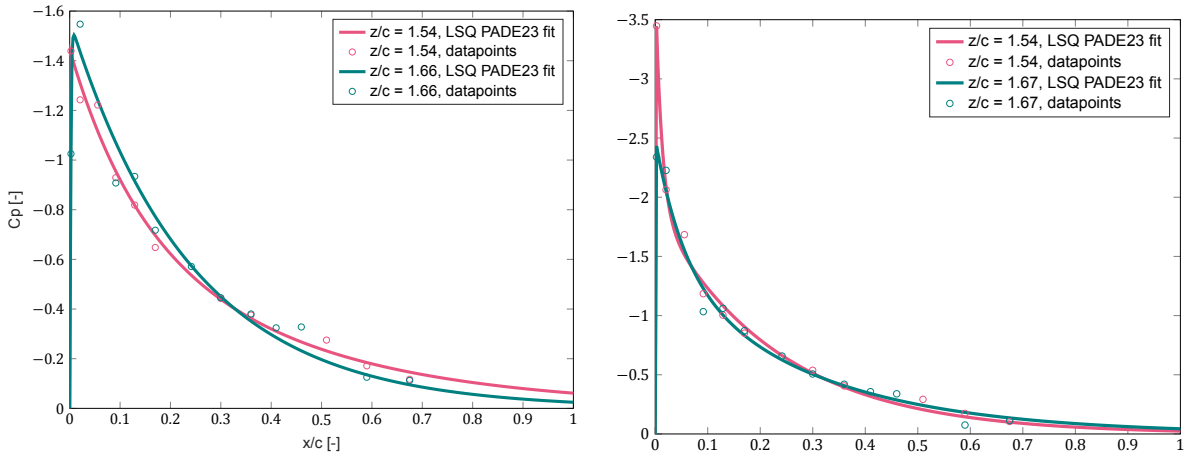

(a) Roll angle 60°, AoA 8°

(b) Roll angle 60°, AoA 12°

Figure 6.2: Pressure distribution from upper and lower pressure array close to each other. NACA0012 surface-piercing hydrofoil, AR 3.46, Re $3.42 \cdot 10^5$.

These discrete data point results are given in table 6.3. Per pressure tapping the value and percentage difference is depicted. The left side of the table shows the results for AoA 8° and the right side shows the data for AoA 12°. In this table more entries are left empty, than in table 6.1. If a sensor of either one of the arrays is faulty, no error percentage difference can be computed. The lower the percentage difference is the higher the precision of the measured values.

Table 6.3: Pressure coefficient values compared to each other for semi-repetitive run. At roll angle 60°, and AoA 8° and 12°. NACA0012 surface-piercing hydrofoil, AR 3.46, Re $3.42 \cdot 10^5$.

		AoA 8°			AoA 12°		
	x/c	z/c=1.54	z/c=1.67	%	z/c = 1.54	z/c=1.67	%
T1	0.0025	-1.44	-1.03	34%	-3.45	-2.34	38%
T2	0.02	-1.24	-1.55	22%	-2.06	-2.23	8%
T3	0.06	-1.22			-1.68		
T4	0.09	-0.93	-0.91	2%	-1.19	-1.03	14%
T5	0.13	-0.82	-0.93	13%	-1.00	-1.06	6%
T6	0.17	-0.65	-0.72	10%	-0.85	-0.87	2%
T7	0.20						
T8	0.24		-0.57			0.66	
T9	0.30	-0.44	-0.45	0%	-0.54	-0.51	6%
T10	0.36	-0.38	-0.38	1%	-0.41	-0.42	3%
T11	0.41		-0.32			-0.36	
T12	0.46		-0.33			-0.34	
T13	0.51	-0.27			-0.29		
T14	0.59	-0.17	-0.13	31%	-0.17	-0.08	79%
T15	0.67	-0.12	-0.11	4%	-0.11	-0.11	7%

In this comparison, a percentage difference threshold of 10% is chosen. Since the arrays are not on the same location and the measurements are made with a different extension piece. Swapping of the extension piece can have caused environmental changes, eventough precautions were taken during the experiments. On sensor level the differences between the two arrays are significant (more than 10%) at locations T1, T2, T5 and T14. For both AoA 8° and 12° the sensor at T1 of the lower array measures less than the upper array. It could be that there is a minor air entrapment or a little bit of debris in this tube causing the lack of measured pressure. The difference is too large to be the cause of environmental changes between the runs, or to be a cause of the 15 mm height difference between the measurements. T2 only has a large difference at AoA 8°, looking at figure 6.2a it is seen that for the lower array, this location marks the pressure peak, whereas the upper array is already past the

pressure peak. The difference at T2 is for AoA 12°, less than 10% but here also the lower array measures less than the upper array sensor. The nature of the set-up of this sensor is that the response cannot be more than the physical pressure. The response can be less than the physical pressure due to air entrapment or minor blockage due to debris in the water. T3 has a large difference at AoA 12°, but not at 8°. The influence of the large difference at T14 makes a small impact on the total array results because the magnitude of the Cp is in both cases low.

A comparison based on total array is made as well. For this the suction side contribution to the lift coefficient ($C_{L,S}$) is computed. These results are shown in table 6.4.

Table 6.4: Suction side lift contribution ($C_{L,S}$) for different arrays at AoA 8° and 12°, for 60° roll angle. NACA0012 surface-piercing hydrofoil, AR 3.46, Re $3.42 \cdot 10^5$.

	z/c=1.54	z/c=1.67	%
AoA 8°	-0.3683	0.3638	1.21
AoA 12°	0.4391	0.4407	0.35

On the array level, the percentage difference between the upper and lower array is negligible for both angles of attack. The maximum difference of 1.21% can be caused by environmental differences. On array level the precision is thus high. Where on the sensor level some locations showed significant differences, primarily the sensors towards the leading edge have a low precision. Based on these results the repeatability of a pressure reconstruction has proven to be successful, the precision on a sensor level is not satisfactory.

6.2. Characterisation of the foil and validation of method

This section contains the results of experiments all at 0°roll, for angles of attack 8° and 12° (pressure and suction side).

6.2.1. Characterisation of the foil

The hydrodynamic force plots are shown in figure 6.3. The results consist of static measurements and a dynamic sweep. The dynamic sweep is two sweeps merged together. Sweep 1 going from -4°to 18°and sweep 2 from 4°to -18° AoA. The sweep is cut into two, to be able to keep the rotational speed as low as possible. The rotational speed is 1.1 *s/deg*, to avoid adding dynamic effects to the measurements. With only two of these swept runs, the entire range from stall to stall angle is captured.

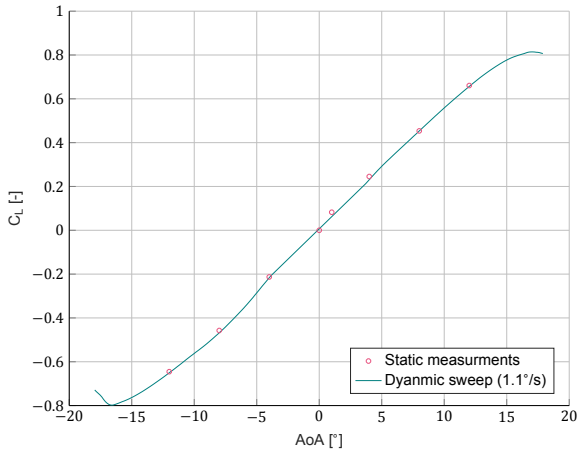

(a) Lift coefficient vs Angle of attack

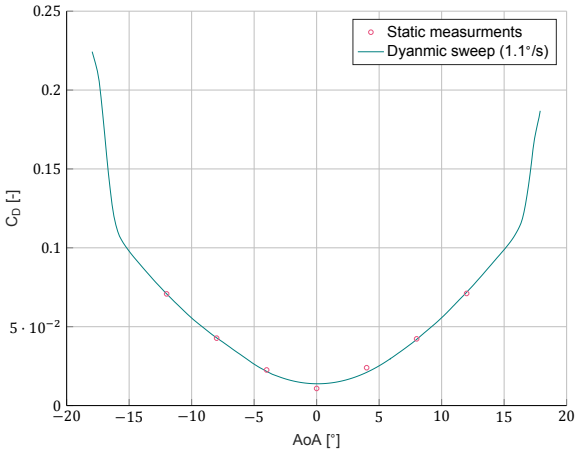

(b) Drag coefficient vs Angle of attack

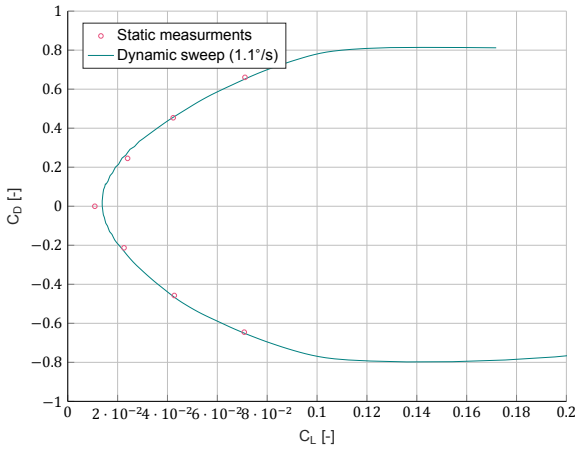

(c) Polar lift versus drag coefficient

Figure 6.3: Hydrodynamic coefficients of NACA0012, AR = 3.45, Re = 3.42·10^5 at 0° roll angle.

The lift curve, between the two stall angles, is not completely linear. The dynamic sweep has some minor bumps and hollows in the curve. The static measurements also have slight non-linearity. However, the trend is linear and symmetrical around AoA 0°. These results are all single shot results, these bumps are most likely due to the measurement errors. The stall angles are found at -16.6° and 17°. The slight difference in negative and positive side of the C_L, might be a result of the model geometry. Along the entire span there is a juncture between foil and lid, which is joint together very tight but could still effect the flow slightly. On that same side of the foil there are plasticine-filled screw holes which could also have slightly altered the symmetry of the forces from negative to positive angles of attack. This dissimilarity is more difficult to spot in the drag coefficient curve, since the forces are much smaller, thus the relative difference is less noticeable.

The drag curve shows the expected bucket-like shape and is symmetrical around the 0° AoA axis. The sharp increases in drag match the stall angles found from the lift curves at -16.6° and 17° AoA. The dynamic sweep results coincide with static measurements almost everywhere. Having verified the results of the dynamic sweep at a rate of 1.1°per second yields near identical results as static results. The dynamic sweep can be used to characterise the foil, and there is no need for additional static measurements at a larger AoA range than those already executed.

Comparing the results to other data demonstrates if the measurements are within the order of magnitude expected and if the trend coincides. This is done for the lift coefficient curve in figure 6.4, against three other methods. An empirical result (see equation 2.11), the thin airfoil theory 2π lift slope, and an Xfoil prediction. Both the thin air foil slope and Xfoil prediction are corrected to account

for finite length and free-surface interaction.

The finite length is corrected for with the AR correction (eq. 2.8) and an additional factor to correct for small AR (eq. 2.9). The free surface correction factor (F), based on the biplane effect was found to be 0.9006 (eq. 2.10). Another free-surface correction formula, proposed by Damley (2019), dependent on the mean submergence and chord length (eq. 2.13) is 0.9658. The free-surface correction based on the biplane effect is more generic, as it is also applicable to submerged foils. The factor proposed by Damley is empirically found specifically for vertical surface-piercing hydrofoils. It is found that using the free-surface correction of Damley, matches the results better.

All resulting curves are shown in figure 6.4). The empirical method takes into account finite length and free-surface interaction, but is an inviscid solution. The theoretical lift slope, of 2π, is corrected for finite length and free-surface interaction, but also inviscid. The theoretical lift slope is based on thin airfoil theory, the NACA0012 is not typically classified as a thin airfoil. The Xfoil prediction is a viscous solution, and is also corrected for finite length and free-surface interaction.

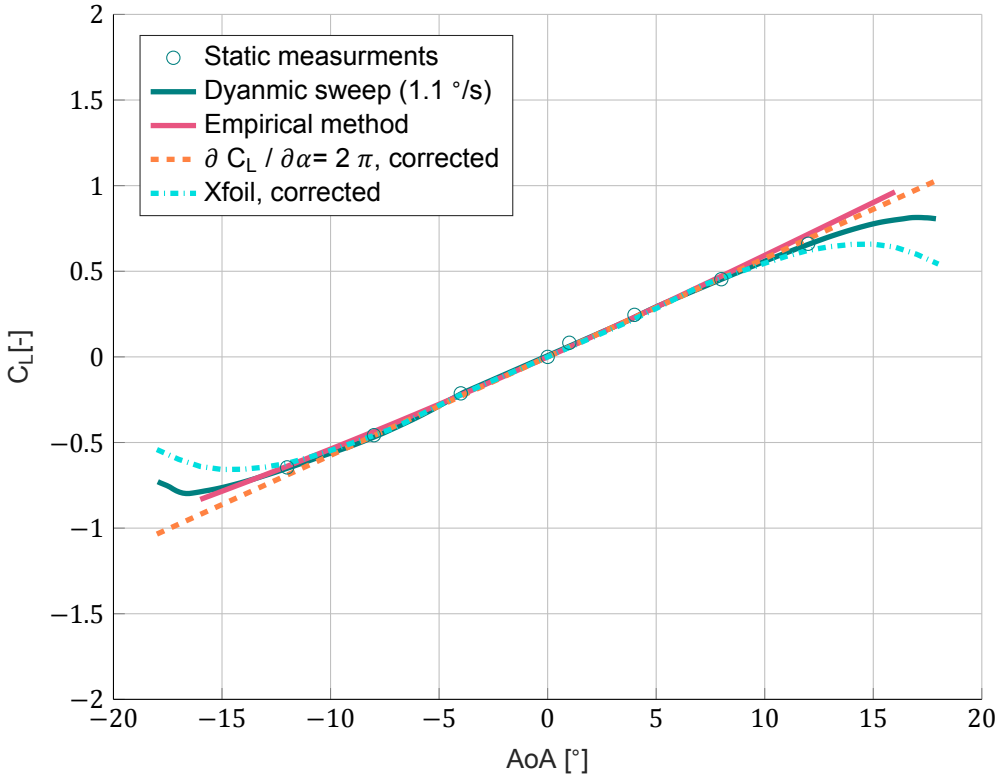

Figure 6.4: Comparison of the measured lift coefficient polar to the theoretical value, numerical simulation and an empirical method

The measured lift coefficient coincides with all three methods in the middle AoA range (from -8° to +8°). Thus the imposed correction factors on the thin airfoil theory and Xfoil simulation yield the 3D lift coefficient for a surface-piercing hydrofoil. For higher AoA the curves start to deviate. The empirical solution fits the data better than the thin airfoil theory slope, expected since the empirical solution is specifically designed for surface-piercing hydrofoils whereas the theoretical slope is generally applicable. At the outsides of the AoA range the measured lift is more comparable to the Xfoil simulation since here stall angles are observed as well. The measured stall angles are larger than those predicted by Xfoil. This is beneficial since the operational range of AoA is larger for this model. It is however more likely that it is the cause of the dynamic sweep. Acosta mentioned the dynamic stall angle to be larger than a static stall angle, and that is also the difference here. The rational speed of the sweep has been kept intentionally low, but no convergence study into the rotational speed has been carried out. The force measurements are in good agreement with the other methods.

6.2.2. Validation pressure measurements for 0°roll angle

In this section, the pressure measurements at 0° roll are depicted, and these results are compared to other known data.

First, the data points are plotted per span-wise location with a the PADE 23 least square method fitted curve in figures 6.5 and 6.6. In all figures, the error of the data point is plotted. For each discrete data point the standard error is computed as in section 5.1. The error is to small to plot an errorbar, thus the error is plotted as enlarged markers, of which the enlargement factor is noted in the figure title.

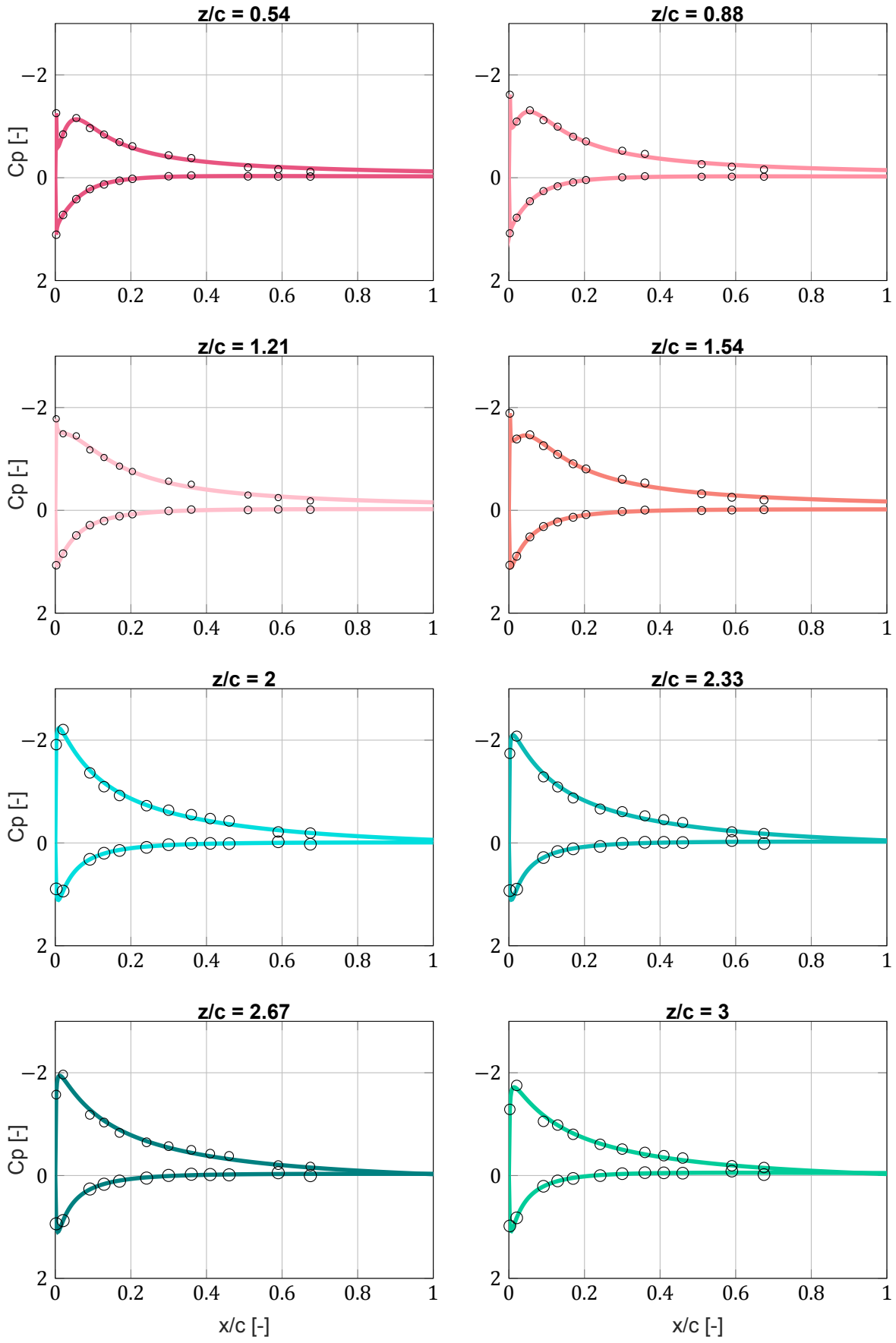

Figure 6.5: Roll angle 0°, AoA 8°. Pressure distribution over the chord for all span-wise locations. Showing the measured data points and computed PADE23 LSQ fit. NACA0012 surface piercing strut, AR 3.46, Re $3.42 \cdot 10^5$.Note: all error bars fall within the data point marker, with a factor 100 enlarged marker.

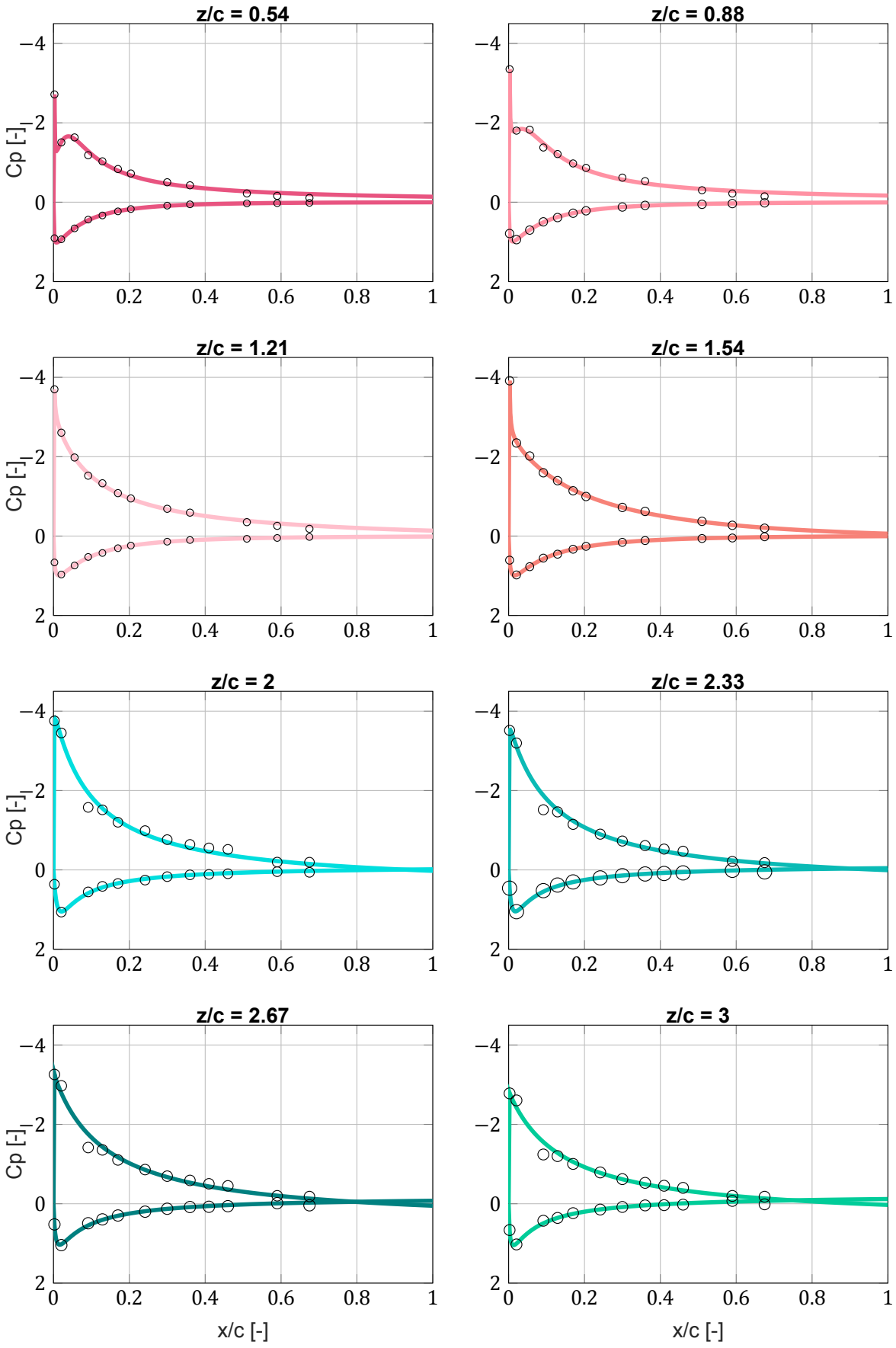

Figure 6.6: Roll angle 0°, angle of attack 12°. Pressure distribution over the chord for all span-wise locations. Showing the measured data points and computed PADE23 LSQ fit. NACA0012 surface piercing hydrofoil, AR 3.46, Re $3.42 \cdot 10^5$.Note: all error bars fall within the data point marker, with a factor 100 enlarged marker.

All measurement errors are computed as shown in section 5.1, the errors obtained from this are for all data points really small. So small that adjusting marker size to error size, the marker is not visible anymore. Therefore the marker size is enlarged.

In figure 6.5 the datapoint at position T2 makes a huge dip in the pressure reconstruction for z/c = 0.54, 0.88, 1.21 and 1.54. Those are all measured with the upper array. Is this a faulty sensor or is there a physical explanaiton for this? If the sensor at T2 of the upper array was faulty, this would have shown in the re calibration process. In figure 6.6 a huge dip also due to the datapoint at T2 is observed, but now only for z/c = 0.54 and 0.88. The reason for the dip does not lie in the working of the sensor. A physical explaination can be found in the laminar seperation bubble (LSB).

The laminar separation bubble forms where the flow transitions from laminar to turbulent on the foil surface. This turbulence creates vortices that cause a reduction in pressure on the surface. This reduction makes that the flow detaches momentarily. In a pressure distribution, the LSB is identified where a small plateau of the Cp is found (Sreejith and Sathyabhama, 2020, Jahanmiri, 2011). Delafin's (Delafin et al., 2014) experiment has shown the LSB location is rather close to the leading edge for angles of attack larger than 6°. This does match what is seen here.

The pressure reconstructions all have a high adverse pressure peak near the LE for the suction side and a minor peak on the pressure side approaching Cp = 1. Towards the trailing edge the curves smooth out towards Cp=0. This matches the standard characteristic of a pressure distribution.

The fitted curves shown in 2D in previous figures are now plotted in a 3D space, which mimics the foil surface in figures 6.7. From this figure the trend of the pressure measurements over the span is better seen.

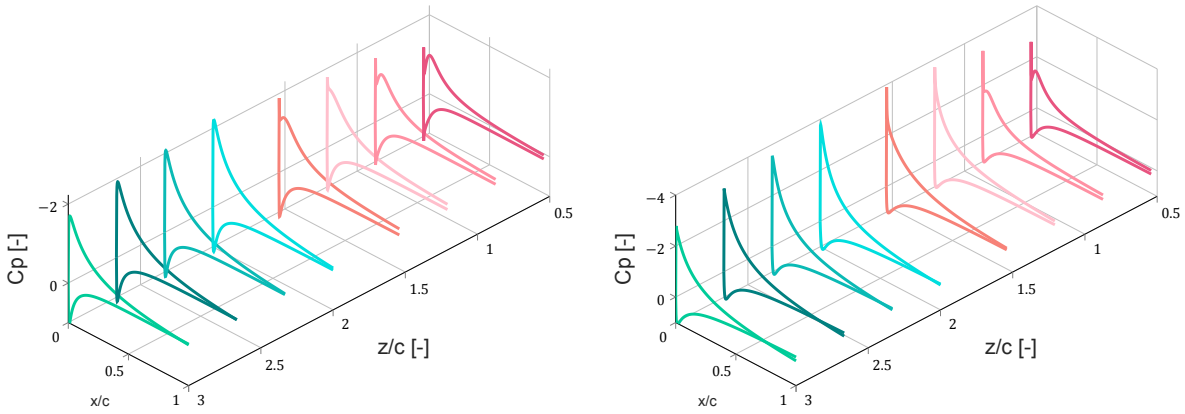

(a) Roll angle 0°, angle of attack 8°

(b) Roll angle 0°, angle of attack 12°

Figure 6.7: 3D representation of the pressure distribution over the chord for all span-wise location, illustrating the distribution over the surface. NACA0012 surface-piercing hydrofoil, AR 3.46, Re $3.42 \cdot 10^5$.

It is expected that the span-wise distribution is cubic with minima close to the end of the foil and approaching the free-surface. This is also seen from other research (Harwood et al., 2016, P.15). At the free-surface the free stream pressure and local pressure are both equal to the atmospheric pressure. Therefore the pressure coefficient is close to non-zero for the shallowest z/c reading. The highest pressure peak value is found for z/c = 2. The maximum Cp at this location is expected since here the interference from the free-surface and finite foil length are minimum.

The next and last step is the surface pressure distribution plot in 3D as shown in figures 6.8. In span-wise direction again the LSQ method is used, as described in chapter 5 a cubic relation is assumed.

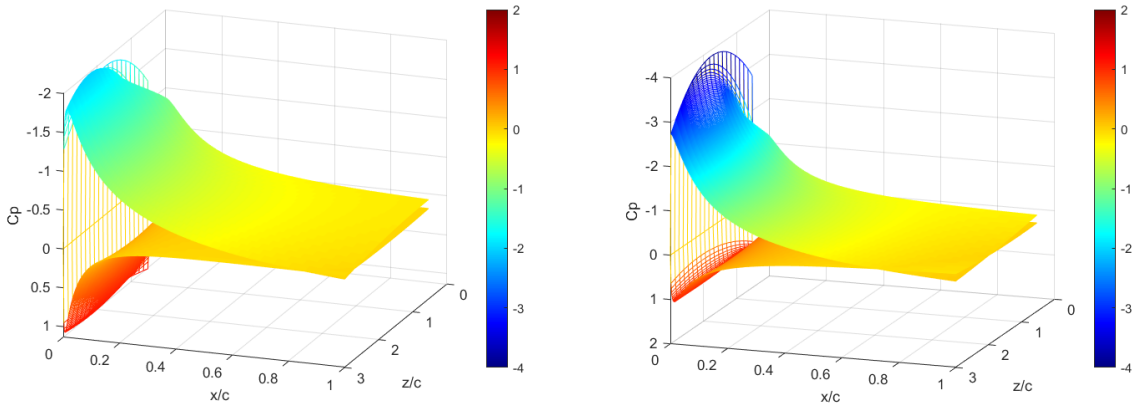

(a) R0A8 - roll angle 0°, angle of attack 8°

(b) R0A12 - roll angle 0°, angle of attack 12°

Figure 6.8: Full surface pressure plot. NACA0012 surface-piercing hydrofoil, AR 3.46, Re $3.42 \cdot 10^5$.

Integrating these figures and multiplying by the cosine of the AoA yields the three dimensional lift coefficient (C_L) based upon the pressure reconstruction method.

To gain insight into the accuracy of the magnitude of measured data, a comparison to a 2D pressure distribution from Xfoil is made. The experimental values measured at 2/3 (z/c = 2) of the submergence are the least affected by both free-surface as finite foil length. This measurement is plotted in figure 6.9 against the 2D pressure distribution from Xfoil. An additional curve is plotted, the Xfoil simulation is corrected for both finite length and free-surface interaction.

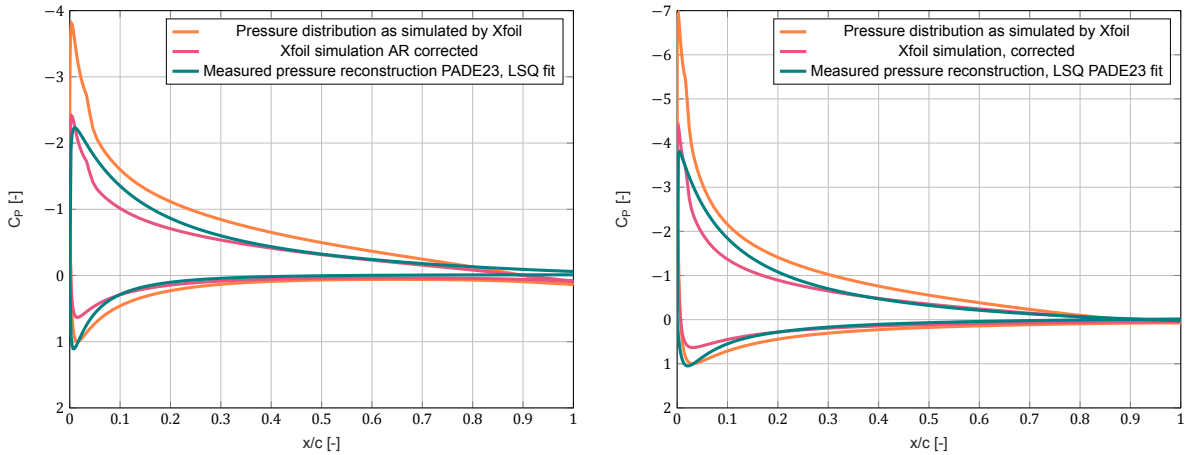

(a) Roll angle 0°, angle of attack 8°

(b) Roll angle 0°, angle of attack 12°

Figure 6.9: Pressure distribution of 2D viscous Xfoil simulation and the Xfoil simulation AR corrected compared to measured pressure distribution on 2/3 of the submergence, z/c = 2. NACA0012 surface piercing foil, AR 3.46, Re $3.52 \cdot 10^5$.

The Xfoil pressure distribution is overall higher than the measured pressure distribution. This is expected since the Xfoil pressure distribution is a 2D approximation, and the measured pressure distribution is although chosen at z/c=2 still under influence of free-surface and AR. The general shape of the measured curve matches that of Xfoil. In both cases, not the entire peak is captured. There is an experimental data point within the pressure peak, is significantly lower than the theoretical pressure peak. This means that (mis)capturing the pressure peak is in this research not due to the number of pressure tappings or their locations.

The difference in the area underneath the pressure curve is for AoA 8° it is 34% and for AoA 12° it is 35%. This difference is a result of comparing a true 2D lift coefficient (Xfoil) to a quasi 2D lift

coefficient. The measured pressure distribution is at z/c=2 least affected by the free-surface and tip of the foil. But the measurement is greatly affected compared to a 2D situation. Figure 6.9 shows whether or not the trend of the measured pressure distribution is in line with the expectancy. When the corrections have been applied to the Xfoil simulation the curves come rather close together. Still a discrepancy is visible, the difference in area underneath the curve is now -11% for both AoA. This is a Xfoil pressure distribution that would yield a 3D lift coefficient, whereas the measured pressure curve is a sectional pressure curve measured in a 3D environment. The measured pressure reconstruction depicted is a quasi 2D curve, the comparison is therefore not completely fair but it gives an indication. The fact that the area underneath the curve of Xfoil is now less than the measures quasi 2D ares, is therefore logical. The tendency of the curve and the pressure peaks, do come closer together.

The lift coefficient can be computed at every measured span-wise location from the pressure distribution using the following formula, where subscript p and s indicate pressure or suction side.

$$C_l = cos(\alpha) \int Cp_p - Cp_s d(x/c) \tag{6.2}$$

Applying this equation to the measured pressure distribution yields a sectional lift coefficient as well, but it is highly influenced by the free-surface or foil tip dependent on the location. This is seen in figure 6.10. The h/c = 2 location is the least influenced, it is the maximum value. Next to the measured curve, a fitted curve is depicted. This fitted curve is forced to have a zero lift coefficient at the end of the foil and at the free surface.

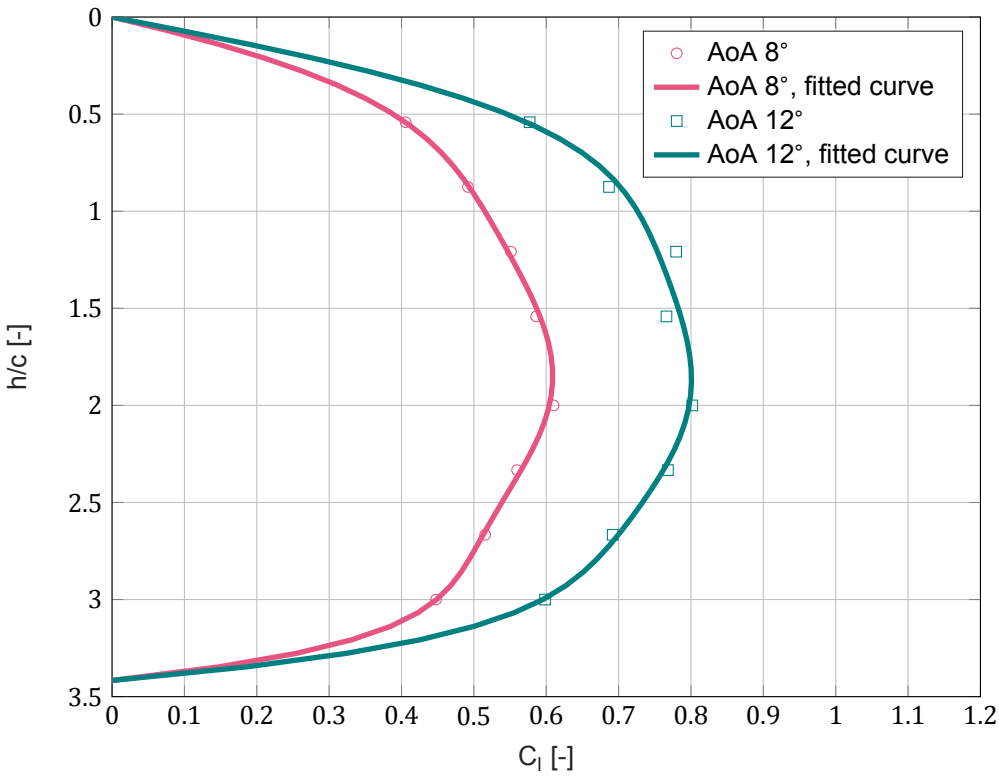

Figure 6.10: Quasi 2D lift coefficient computed from the pressure readings using equation 6.2. The distribution of the lift coefficient against the span is plotted. NACA0012 surface piercing hydrofoil, AR 3.46, Re $3.42 \cdot 10^5$.

Integrating the quasi-2D lift coefficients over the span yields the 3D lift coefficient based on the pressure measurement. This value is compared against the 3D lift coefficient based upon the force measurements, the empirical method (eq. 2.11) and, corrected Xfoil value (using eq. 2.8 and free-surface correction factor). In table 6.5 all measured/computed 3D lift coefficients for 8° and 12° AoA are depicted.

Table 6.5: Lift coefficient from force measurement and from pressure reconstruction and based on empirical model (by eq. 2.11) and Xfoil result AR corrected

C_L	Pressure measurement	Force measurement	Empirical computation	Xfoil corrected
AoA 8°	0.52	0.45	0.51	0.53
AoA 12°	0.69	0.68	0.77	0.72

The percentage difference from the C_L based on the pressure measurements to the rest is depicted in table 6.6. The force and pressure measurements are of the exact same foil in the same conditions measured at the same time. The empirical computation corrects for the free-surface and AR, but is non-viscous. And the AR corrected Xfoil simulation is corrected for AR and viscous, but doesn't take into account free-surface proximity.

Table 6.6: Percentage difference of C_L from pressure measurement to the other computations

	Pressure measurement	Force measurement	Empirical computation	Xfoil, corrected
AoA 8°	-	13.4%	2.5%	-2.1%
AoA 12°	-	1.7%	-10.1%	-4.9%

The lift coefficient as computed from the pressure measurements is higher than the one measured with the force transducers for AoA 8°. Theoretically, the C_L of the pressure readings and the force measurements must be equal, these are captured under the exact same conditions. Since the difference is highest at AoA 8°this is most likely not due to unloading of the foil caused by slight bending. Since then the difference would be expected to be higher for AoA 12°, there is more force acting on the foil in this condition.

Compared to the empirical prediction some discrepancy is expected, due to the solution being non-viscous. It is odd that the computed C_L is for AoA 8° a slight over-prediction (although in close agreement) and for AoA 12° a more significant under prediction. The larger mismatch for R0A12 with the empirical computation, could already have been seen from figure 6.4, where from AoA 8°the discrepancy between the measurements increased. The 1.7% difference for AoA 12° to the force measurement is deemed reasonable and the 2.5% for AoA° to the empirical computation as well. There is no clear reason why the pressure computation for the different angles of attack match with either force or empirical, but not both or the same method. The error between the methods is maximum 13.4%. The comparison to Xfoil is promising. The percentage difference for AoA 8° and 12° are in the same order of magnitude and relatively small. Based on the results shown in this section, the obtained pressure reconstructions are in good agreement too other methods.

6.3. Results of high angled experiments

This section aims to answer the question of what the quality of the pressure measuring method is under a high roll angle. This is done using the results of the experiment set 2. First, the results of the force measurements are given. The force measurements are also compared to other experiments that are somewhat similar to validate the outcome. Second, the pressure measurements are depicted and these are analysed to come to a sub-conclusion.

6.3.1. Force measurement results and analysis

The lift coefficient at 0°, 45°and 60°roll angles are plotted in figure 6.11. The lift coefficient decreases with increasing roll angle. Between the data points a curve is fitted. From this curve it can be seen that the lift tends to become asymptotic, meaning the maximum lift is achieved at 0° roll angle.

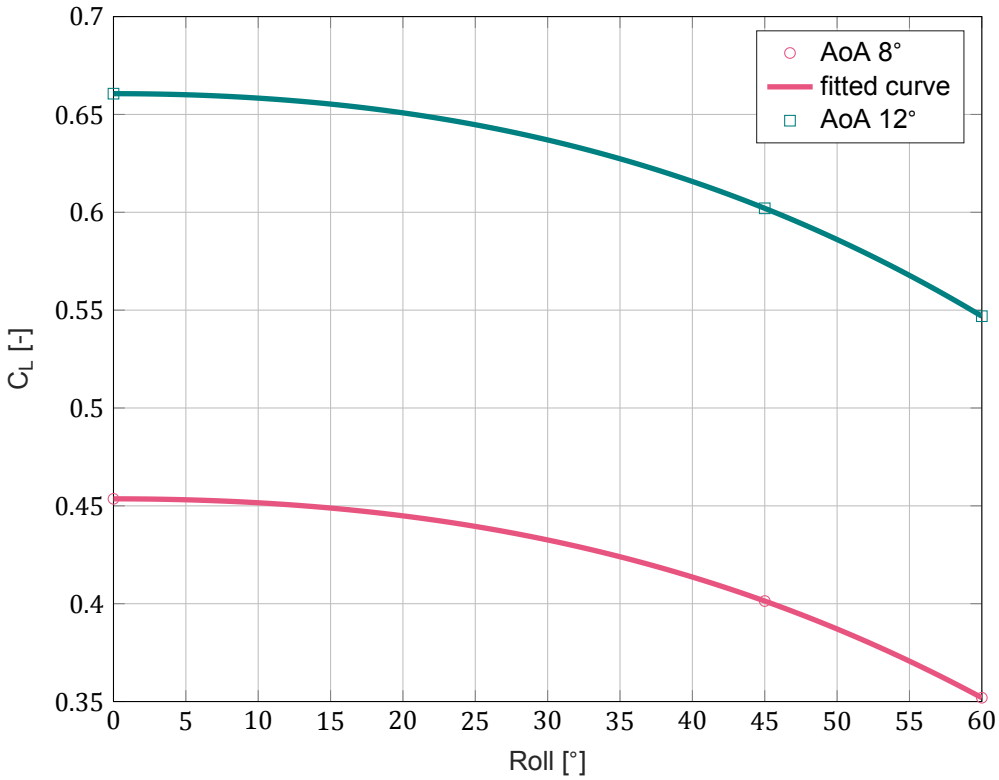

Figure 6.11: Lift coefficient perpendicular to foil surface measured at roll angle 0°, 45° and 60°. Including a fit to illustrate asymptotic tendency towards 0°roll. NACA0012 surface-piercing hydrofoil, AR 3.46, Re $3.52 \cdot 10^5$.

A decrease of lift with increasing roll angle is observed. This is expected since the lifting surface comes closer to the free surface decreasing the pressure over the surface. The curve tends to become asymptotic towards 0° roll angle. Maximum lift at 0° roll angle is logical, since at this angle the lifting surface (suction side) is as far from the free surface as it can be. The decrease in lift from 0° to 60° roll angle is -22% for AoA 8°and -25% for AoA 12°.

A direct comparison with other experiments is not found. Two quite recent experimental researches are found in which a NACA0012 T-foil is used, which note the effect of free-surface proximity on the lift coefficient (J. R. Binns et al., 2008, Ashworth Briggs, 2018 (pages 69-81)). These are horizontal foils that are lifted vertically to reach surface proximity, whereas in this experiment a surface-piercing foil is rolled to achieve surface proximity. To make a fair comparison, the distance from the middle of the submerged span to the free-surface is taken as the averaged h/c for the foil of this experiment. The mean submergence (f_m) for 0° roll is 208 mm, for 45° roll 147 mm and for 60° roll 104 mm. Since the initial values are different in the research, the relative differences are used and not the absolute C_L. The relation between roll and submergence is described below.

$$f_m = \sin(\phi) \cdot s/2 \tag{6.3}$$

To estimate a corresponding roll angle from the h/c values of Briggs and Binns the following equation is used. This equation is an approximation that relates h/c to a roll angle using the midspan location as an averaged submergence when under a roll angle.

$$\phi = 90° - \arcsin(2cs \cdot \frac{h}{c}) \tag{6.4}$$

Using this equation, the results of Briggs and Binns can be expressed using roll as well. These are plotted as discrete points in figure 6.12.

Together with the experimental values, the empirical method of Tinney (eq. 2.14 is plotted as well. This is a formulation that expresses the influence on initial lift coefficient due to roll angle. This empirical method is specially for surface-piercing hydrofoils, closest agreement to this curve is expected.

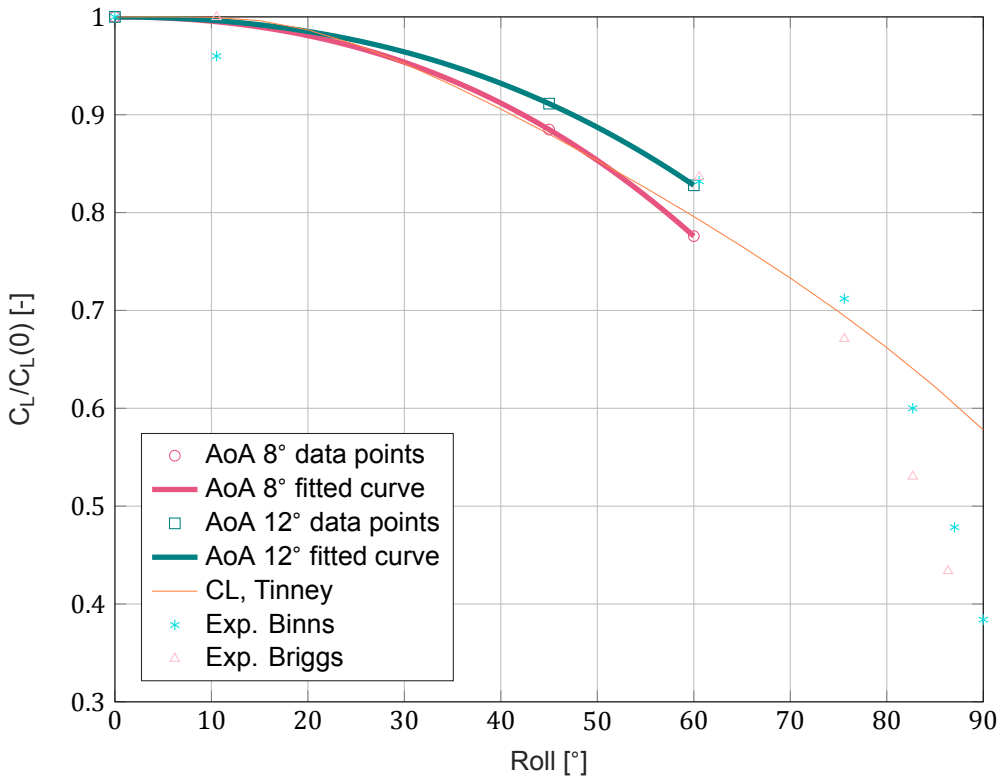

Figure 6.12: Comparison between expression Straub and experimental values, for influence roll angle of surface piercing hydrofoil on lift coefficient

After altering the results of Binns and Briggs, it is now seen that the h/c range tested are not really in range of these experiments. Of course, the roll angle is computed artificially. The operational conditions of these tests are also different. Binns' experiment is run at Re $2.4 \cdot 10^5$ and AoA of 8°. Briggs' experimental results are for an AoA 8and Re $4.55 \cdot 10^5$, at 4 m/s. Since the relative lift coefficient is plotted, this has already less of an impact. However, the trend of the lift decrease does depend on velocity and angle of attack. Comparing the measured results to these two experimental results of a tapered NACA0012 T-foil, proved to be difficult. And from the comparison, no real conclusion could be drawn.

The comparison to the analytical expression of Tinney gives a better indication to whether or not the obtained force results are reasonable. The initial value used here is the lift coefficient at 0° roll angle measured for the corresponding angle of attack. The analytical curve of Tinney lies between the experimental results of AoA 8° and 12°. The comparison to Tinney's work does give a good indication that the magnitude of reduction in lift versus roll angle is correct.

6.3.2. Pressure measurement results

For 60° roll angle, suction side surface pressure measurements are shown. The data points per span-wise location are shown together with the fitted curve using LSQ method in figure 6.13 for 8° angle of attack and in figure 6.14 for 12° angle of attack.

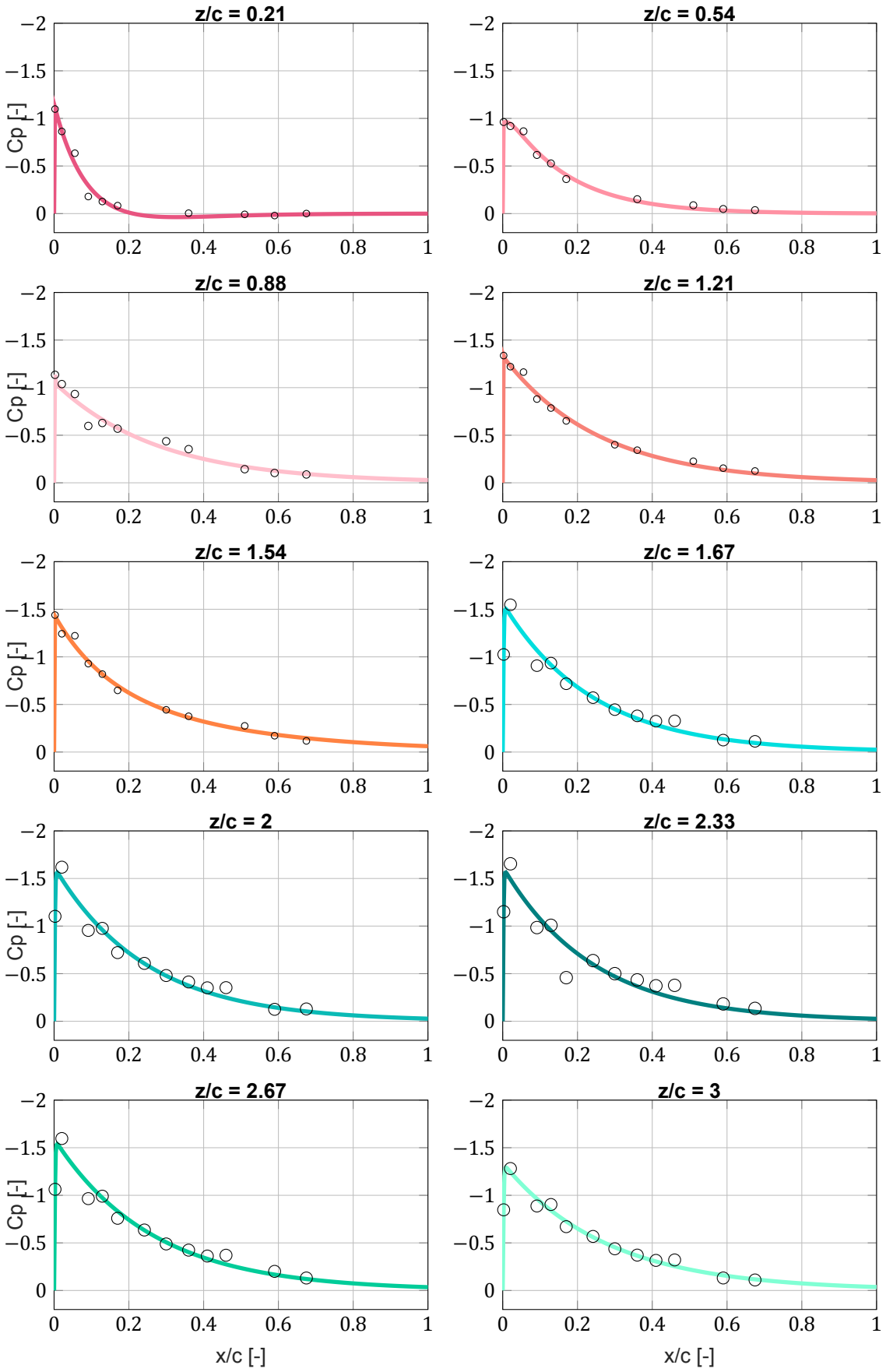

Figure 6.13: Roll angle 60°, AoA 8°.Pressure distribution over chord for all span-wise locations, showing the measured data points and computed PADE23 LSQQ fit. NACA0012 surface-piercing hydrofoil, AR 3.46, Re $3.42 \cdot 10^5$. Note: all error bars fall within the data point marker, with a factor 50 enlarged marker

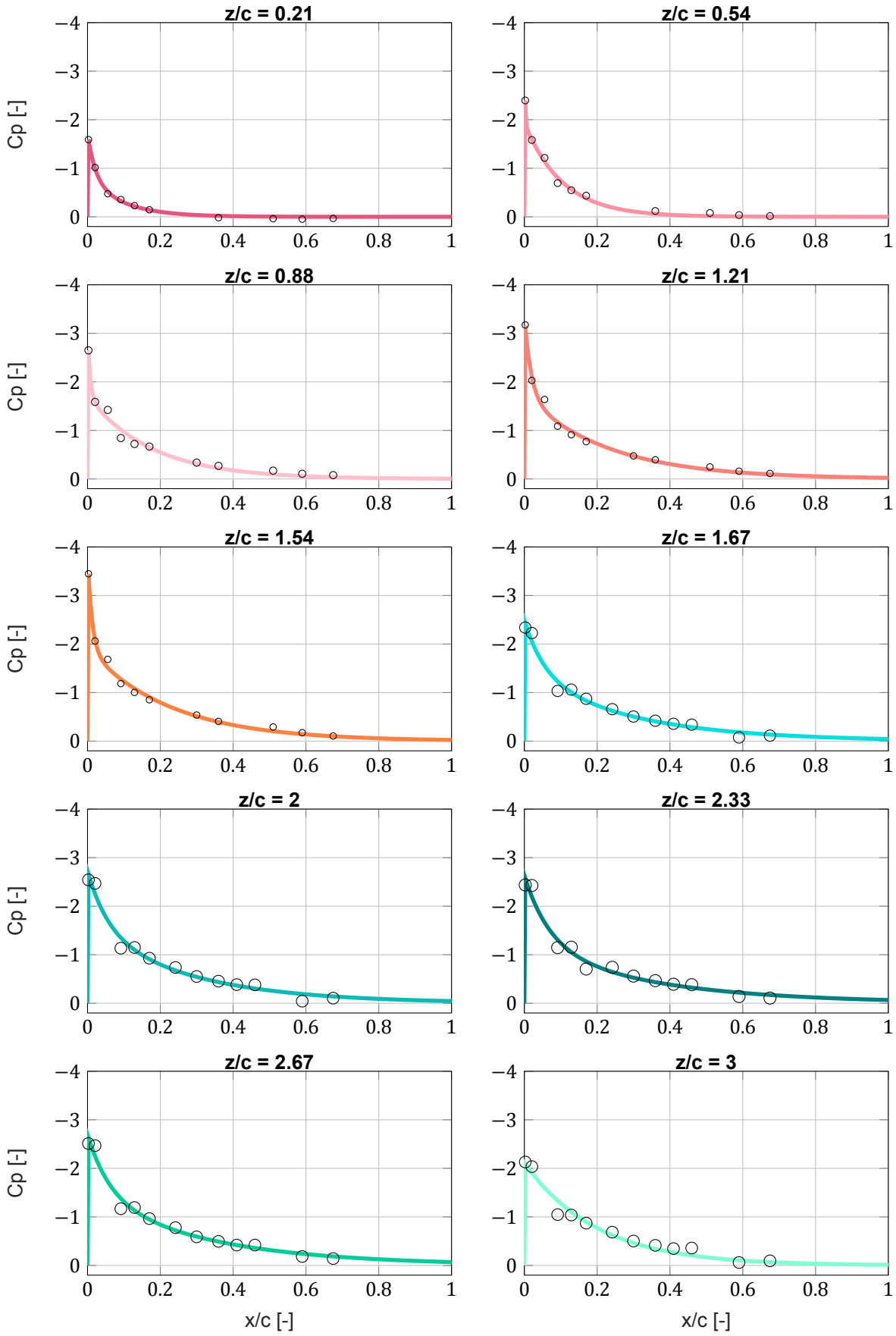

Figure 6.14: Roll angle 60°, AoA 12°. Pressure distribution over chord for all span-wise locations, showing the measured data points and computed PADE23 LSQQ fit. NACA0012 surface-piercing hydrofoil, AR 3.46, Re $3.42 \cdot 10^5$. Note: all error bars fall within the data point marker, with a factor 50 enlarged marker

Looking at the pressure distributions in figures 6.13 and 6.14, the uppermost reading has a Cp slope around zero for most of the chord. This is the reading in closest proximity to the free surface, with increasing submergence the pressure distributions become fatter. The pressure peak rises and the pressure decrease is more gradual than abrupt.

In figure 6.13, for z/c=1.21 and 1.54 indications of LSB are found between T2 and T3. For the five lowest readings of the lower array indications of a LSB is found between T4 and T5. The values measured by these sensors are near identical. The same two sensors have a near identical value at AoA 12°, see figure 6.14. That for 10 different runs two sensors have equal results to each other is strange. The suspicion is that these sensors somehow had cross-talk with each other. Unfortunately this is found after the set-up has been taken apart. Another data point is found, that is most likely an outlier. In figure 6.13 for z/c = 2.33 at T6 (Cp=-0.46). The same sensor looks to have worked properly in all other runs. No recalibration process was carried out for the high rolled set. Therefore, it is most likely that the sensor was faulty during this particular run due to a bit of water on the sensor board, or the tapping got temporarily blocked.

In figure 6.15 the pressure distributions are plotted in a 3D space from which the span-wise relation is observed.

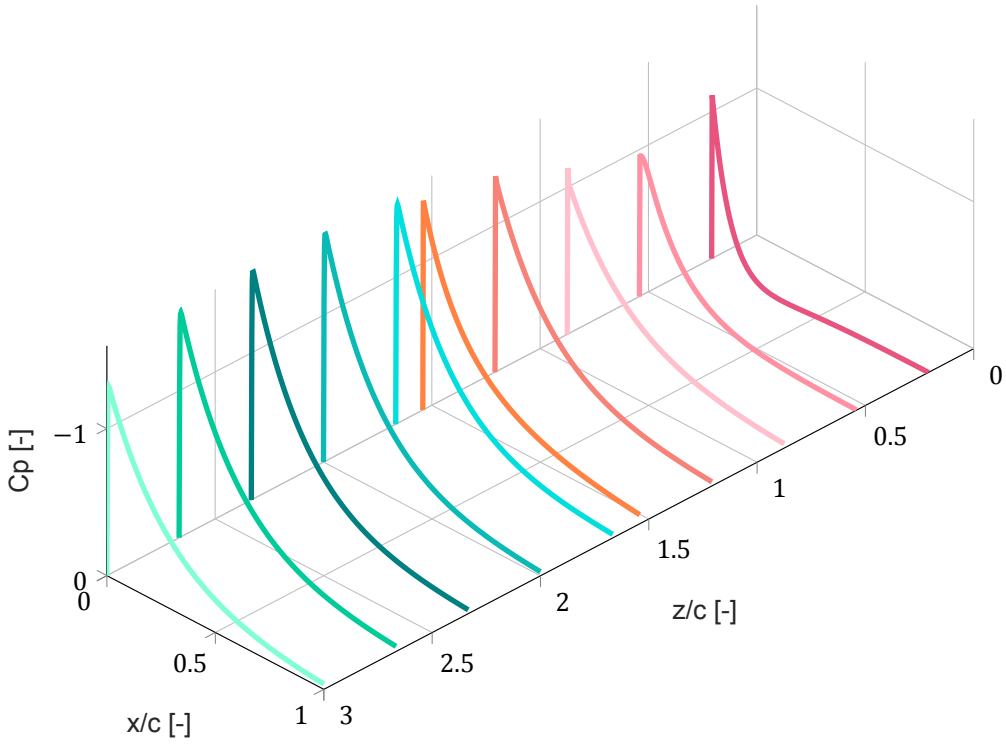

(a) Roll angle 60°, angle of attack 8°

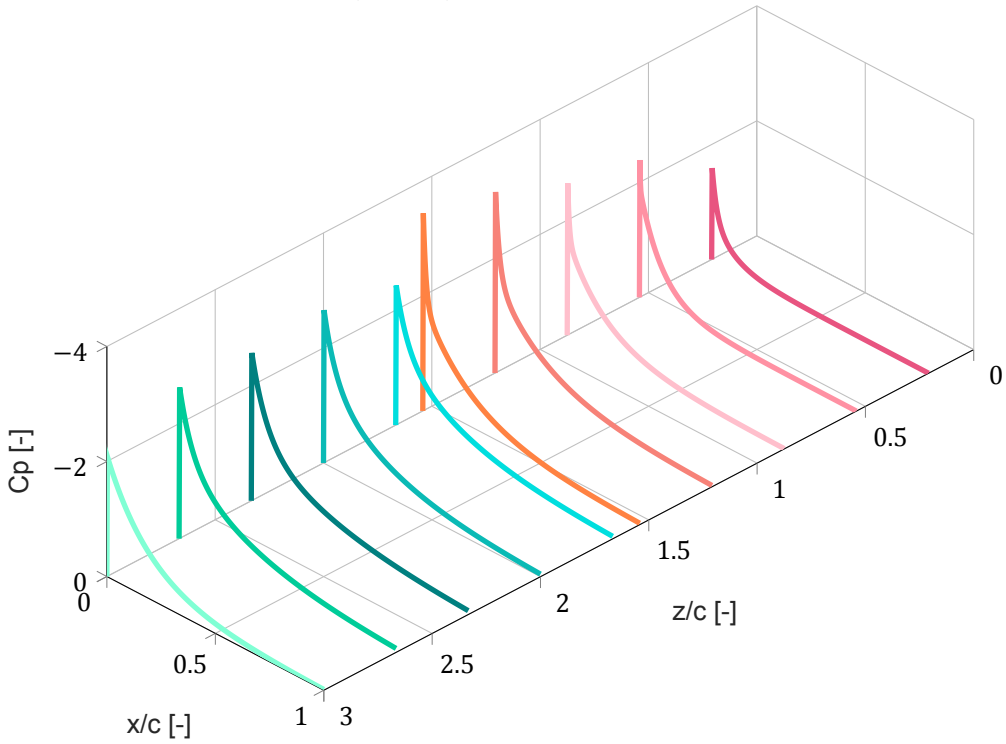

(b) Roll angle 60°, angle of attack 12°

Figure 6.15: 3D representation of the pressure distribution over chord for all span-wise location, illustrating the distribution over the surface. NACA0012 surface-piercing hydrofoil, AR 3.46, Re $3.42 \cdot 10^5$.

Where for 0° roll angle a cubic relation was easily observed is that not the case now. The pressure peak towards the free surface is lower than towards the tip of the foil. At AoA 8° (fig. 6.15a) the pressure peak follows a cubic relation, apart from the upper measurement which is all of the sudden

higher than the previous. For 60° roll and AoA 12°, the pressure peak from upper and lower array seem to deviate significantly. The lower array has not measured the pressure peaks as high as the upper array. The reason could be that the sensor in the pressure peak for the lower array was somehow a bit blocked. It are these two middle measurements that were discussed in section 6.1.

The same curves are also plotted in a 3D space, this mimics the lifting surface of the foil and it gives a better indication on the relation in span-wise direction. For angle of attack 8 and 12 the results are given in figure 6.15.

In figure 6.16, the data is represented as surface plots. This is a result of a span-wise fitting assuming a cubic relation.

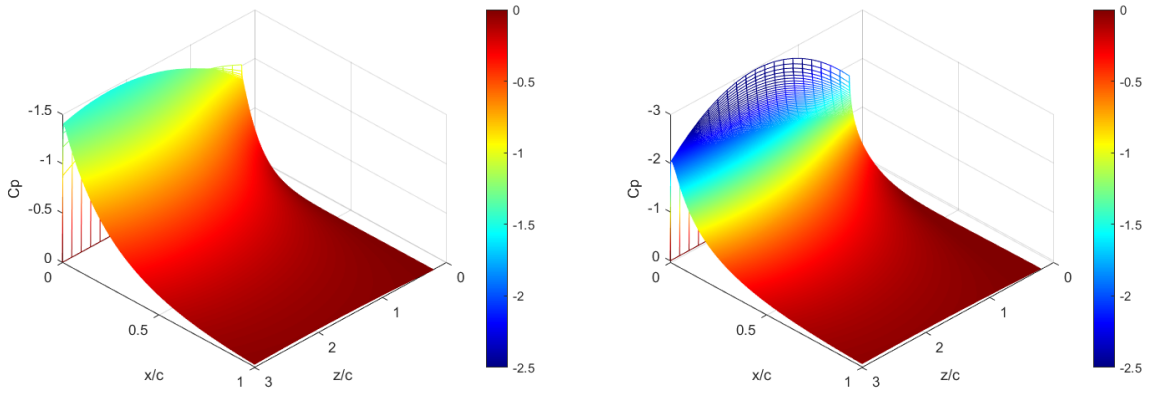

(a) R60A8 - roll angle 60°, angle of attack 8°

(b) R60A12 - roll angle 60°, angle of attack 12°

Figure 6.16: Full surface pressure plot

The aim of this section was to show the potential of the method under high roll angles. Based on the results, the method has proofed to yield equal quality results at 60° roll angle as at 0° roll angle.

6.4. Case study into ventilated experiments

During the experimental phase in the towing tank ventilation occurred during one of the runs. This run was then repeated five times, one more time ventilation occurred. The result of those two runs, annotated as A and B, are depicted in this chapter. The operational condition for which ventilation occurred, was at 60° roll and AoA 12°. Important note is that this chapter is advertised as a case study, since the supporting data is only from two identical runs.

6.4.1. Time traces of force measurements during ventilation

The first result given is a time-trace of the lift coefficient for both runs shown in figure 6.17. The lift coefficient drops from 0.5 to 0.175, this drop is measured in 0.2 seconds.

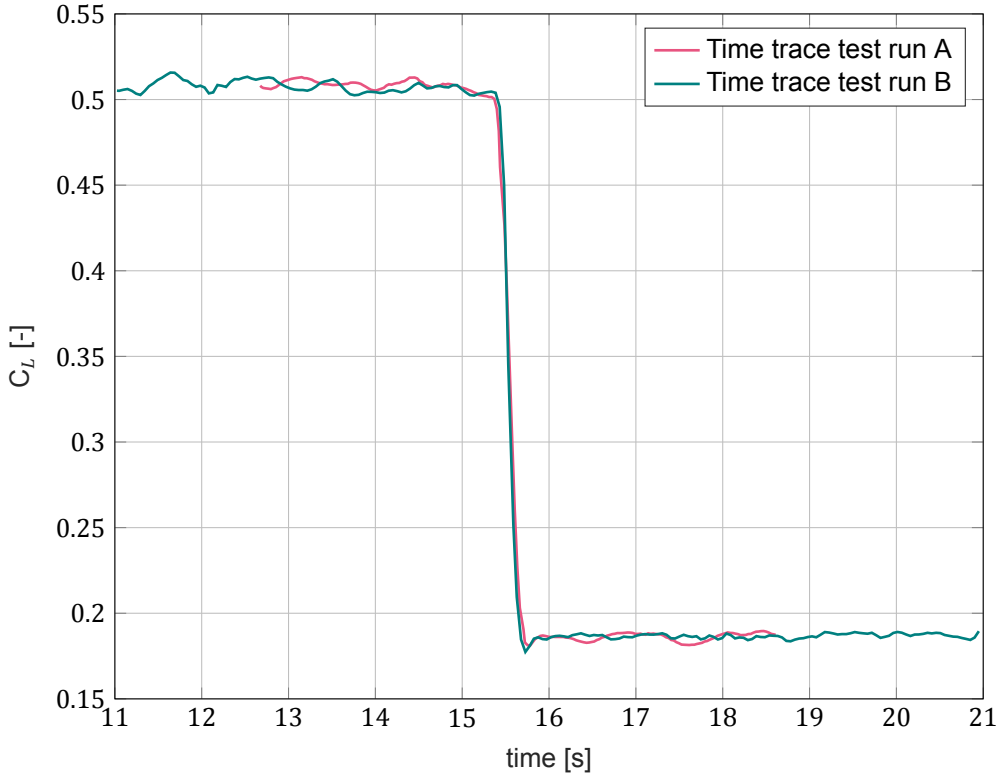

Figure 6.17: Lift coefficient over time measured by the force transducers, of identical ventilation runs A and B. NACA0012 surface-piercing hydrofoil, AR 3.46, Re $3.42 \cdot 10^5$.

The drop in lift as shown in figure 6.17 matches with the expectancy. Ventilating flow bursts over the foil and the hydrodynamic change happens almost instantaneously. The magnitude and behaviour of both runs is in great agreement. The drop in lift of both runs is computed which also gives the difference between the two runs. These results are shown in table 6.7.

Table 6.7: Result analysis of force transducer results of ventilation runs

C_L [-]	Pre	Post	Drop of C_L
run A	0.510	0.186	63%
run B	0.507	0.186	63%
mean	0.508	0.186	63%
Percentage difference	1%	0%	

Of run A and B the lift coefficient pre- and post-ventilation is denoted. Of both runs the lift coefficient is denoted the fourth column. Both run A and B, result in a lift coefficient drop of 63%. In the lowest row, the percentage difference of the measurement itself is given (qualitative control of force transducer). The difference in force measurement is either 1 or 0%. This error is very small and negligible, both before (FW) and during (FV) flows were thus very stable.

6.4.2. Pressure measurements during ventilation

The measured pressure distributions to those two runs are shown in figures 6.18. Both runs are carried out at the same submergence (h/c = 3.46). The extension piece used is 160 mm long, capturing the pressure data at z/c = 0.21 and z/c=1.67. The data points and PADE23 LSQ fit are shown.

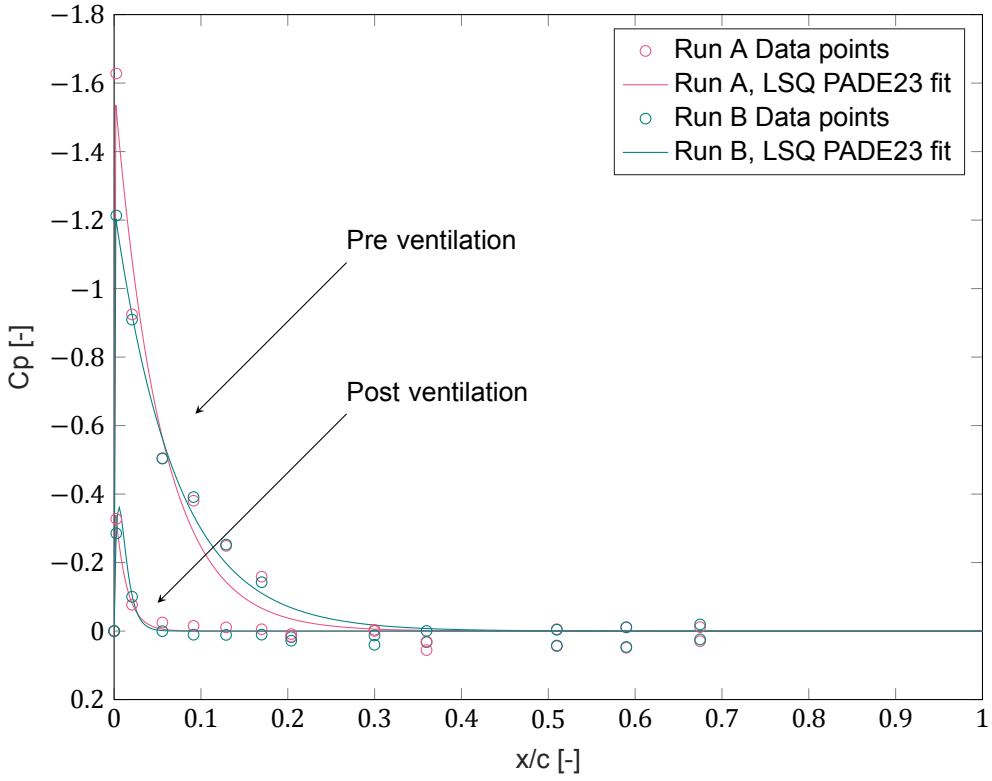

(a) Span-wise location z/c = 0.21

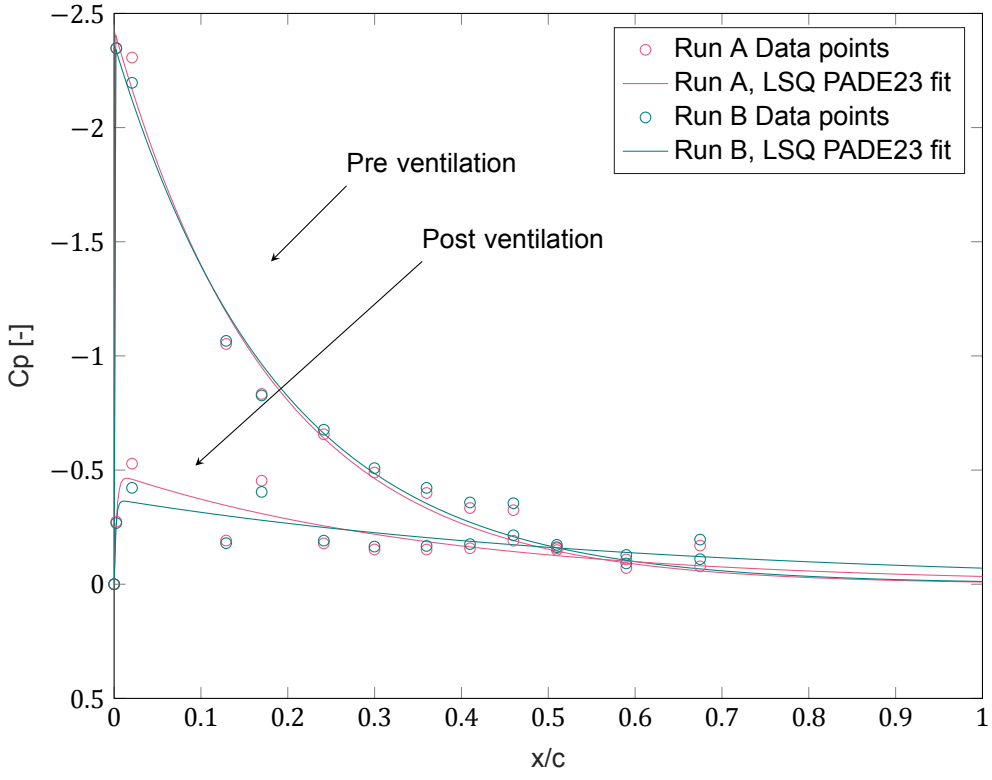

(b) Span-wise location z/c = 1.67

Figure 6.18: Suction side pressure distributions at two span-wise locations pre and post ventilation. This figure illustrates effect of ventilation and it gives insight into tapping measurement due to identical run. Data from runs at 60° roll and AoA 12°. NACA0012 surface-piercing hydrofoil, AR 3.46, Re $3.42 \cdot 10^5$.

At both span-wise locations a great pressure reduction is observed. For the upper measurement the post-ventilation pressure distribution has a small peak and a near-zero slope from x/c 0.09 towards the trailing edge. At z/c = 1.67 there is not so much a peak visible, there is a peak of only -0.5 after which the pressure really gradually decreases towards zero at the trailing edge.

The measurements from the two runs of the lower pressure array are in close agreement. The data points of the upper array seem to have a larger mismatch, than the lower array. This could be due to the fact that the flow fluctuates more in proximity of the free-surface than submerged. To quantify this the measured values are compared to each other in table 6.8.

Table 6.8: Analysis of pressure measurement values for 2 runs A and B, post ventilation. Goal of table to gain insight in error of measurement for repeat run in ventilating conditions

	Upper array			Lower array		
location	run A	run B	diff	run A	run B	diff
T1	-0.327	-0.285	14%	-0.274	-0.268	2%
T2	-0.077	-0.100	-27%	-0.528	-0.422	22%
T3	-0.025	0.000	204%			
T4	-0.015	0.011	1110%	-0.157	-0.161	-2%
T5	-0.011	0.011	-9121%	-0.191	-0.180	6%
T6	-0.005	0.010	-600%	-0.453	-0.404	11%
T7	0.016	0.028	-52%			
T8				-0.179	-0.191	-6%
T9	-0.004	0.013	-363%	-0.152	-0.165	-8%
T10	0.030	0.000	205%	-0.152	-0.168	-10%
T11				-0.157	-0.176	-11%
T12				-0.190	-0.214	-12%
T13	-0.005	-0.004	34%	-0.158	-0.172	-9%
T14	-0.011	-0.011	-4%	-0.109	-0.128	-17%
T15	-0.011	-0.019	-51%	-0.169	-0.196	-14%

From table 6.8 the individual sensor values are compared. The percentage differences are given. For the upper array these differences are substantial, there is also a change in sign of the pressure coefficient at some locations. The absolute values are very small, and the absolute values do not lie very far from each other (see figure 6.18a. Only 2 sensors of the upper array have a percentage difference lower than 15%. This is not a reliable outcome.

The lower array sensors show an increased percentage difference compared to the results in table 6.1. The percentage difference of the lower array is much lower than for the upper array. The pressure field is more stable at this span-wise location, fewer fluctuations due to free-surface. There are 2 sensors with a difference more than 15%. This is a reliable outcome.

Apart from the individual sensors, an analysis can be made after integrating the pressure distribution over the chord. This is a comparison made on array level. These results are given in table 6.9. In this table the values are given pre and post ventilation, including the drop in percentage. This drop is not the same as the force transducers have measured, because only the suction side of the foil is measured with the pressure tappings.

Table 6.9: Comparison of the area underneath the pressure curve, pre- and post-ventilation including the drop. NACA0012 surface-piercing hydrofoil, AR 3.46, Re $3.52 \cdot 10^5$, roll angle 60° and Aoa 12°.

	z/c=0.21			z/c=1.667		
$\int C_p$ d(x/c)	Pre	Post	Drop	Pre	Post	Drop
Run A	-0.0843	-0.0049	94%	-0.4275	-0.1509	65%
Run B	-0.0863	-0.0059	93%	-0.4337	-0.15	65%
Percentage difference	2%	19%		1%	-1%	

The drop of area underneath the pressure curves is for both runs equal. At z/c=0.21 the drop is

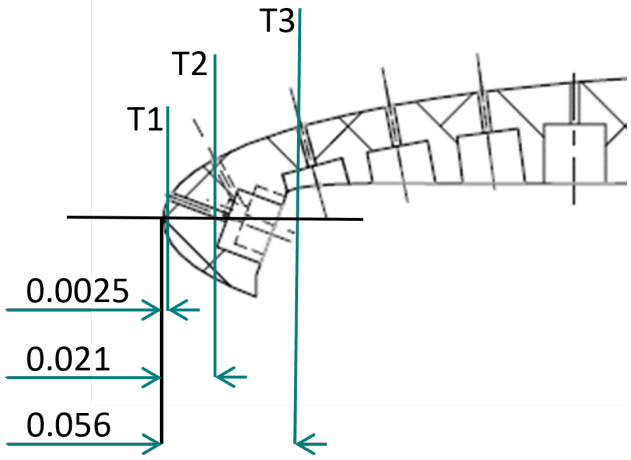

Figure 6.19: Tapping location of first three tapping locations including x/c distance to LE

around 94%. From the drawn pressure distribution in figure 6.18a, was already seen that almost instantly the pressure coefficient dropped to zero. At z/c=1.67, the drop in area underneath the pressure curve is 65%. In post-ventilation, the lower array has a negligible percentage difference (1%). The upper array has a too large percentage difference, the precision is low. Expected is that at array level, the differences average out a little which they did. But the difference for the upper array in ventilating conditions is also on array level too much (19%) to be reliable for any further hydrodynamic computations.

A closer look into the pressure sensor response is done by plotting the time trace of the first three sensors around the time ventilation started. Figure 6.19 is a close up drawing of the locations of these tappings. These time-traces for the two runs separately are shown in figures 6.18. The lower array has a faulty third sensor, thus only the first two are shown. This time trace of the pressure sensors, shows a significant change in pressure, just like the force measurement.

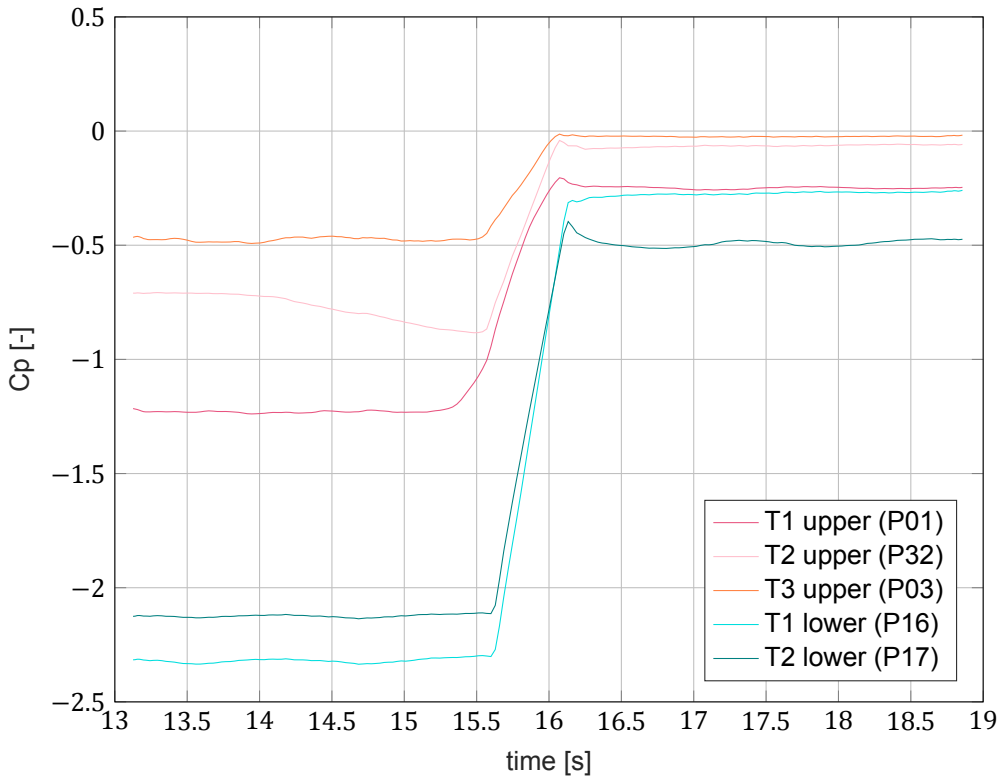

(a) Run A

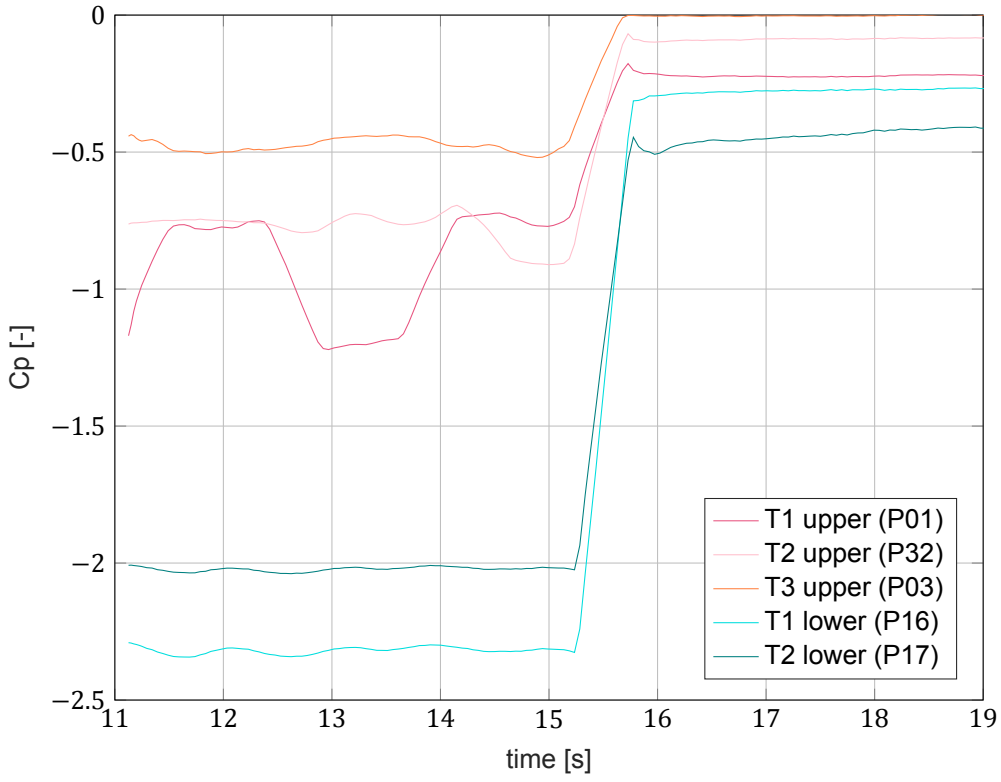

(b) Run B

Figure 6.20: Time trace of the pressure sensors near leading edge, during ventilation. Results given for 60° roll and 12° AoA. NACA0012 surface-piercing hydrofoil, AR 3.46, Re $3.42 \cdot 10^5$.

Interesting to look at is the first and second pressure tapping of the upper array. For run A, it is only the second tapping of the upper array which shows a dip just before ventilation. The rest of the sensors have a stabilised response, both before as after ventilation occurred. The dip in the sensor can be due to a local decrease of water height around the second tapping location, see the blue dashed line. For this there is no clear indication captured on video, see figure 6.21a. Looking at the time trace of run B, it is again the second tapping which has a dip just before ventilation, this time a bit more aggressive. And the first tapping is fluctuating a lot just before ventilation. From the video material of this run, it is seen that there is some shedding happening just before ventilation. Tried to make visible in figure 6.21b inside the blue ellipses. A bit similar to the decreased or fluctuating water height hypothesis, it can be that it is an indication of the rupture of the free-surface (path of ingress). After ventilation, the sensors do balance out to a stable response as well. In the pressure distributions post ventilation from figure 6.18 towards the leading edge a minor peak is still visible. This peak is more pronounced at the upper than at the lower array. Now looking at a snapshot taken for both runs during ventilation in figure 6.22. Here is is seen that towards the leading edge along the span there is attached flow indicated by the dashed orange lines. After it separates and ventilated cavity exists. It is in this small strip attached flow along the span this minor pressure peak exists.

(a) Run A

(b) Run B

Figure 6.21: Video snapshot just before ventilation, for 60° roll and AoA 12°. NACA0012 surface-piercing hydrofoil, AR 3.46, Re $3.42 \cdot 10^5$

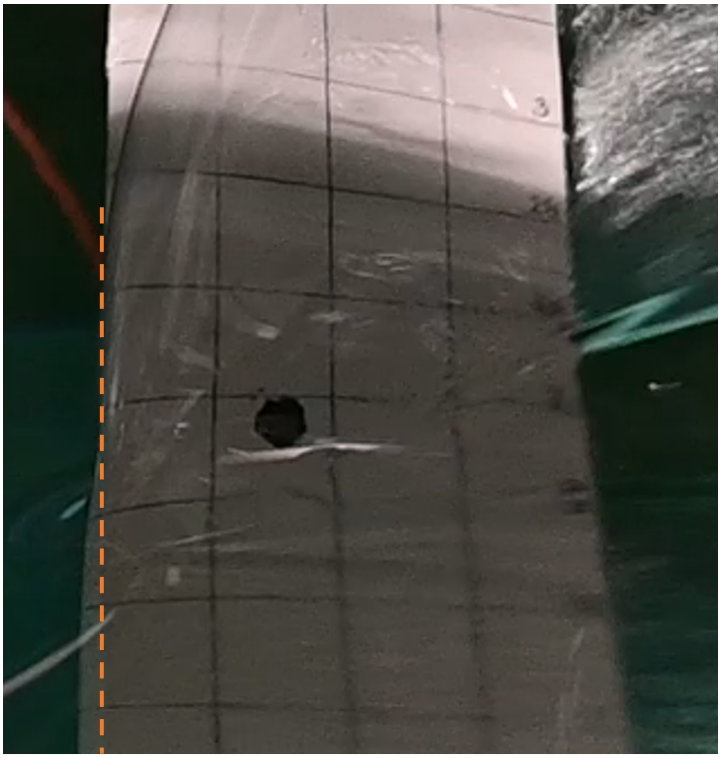

(a) Run A

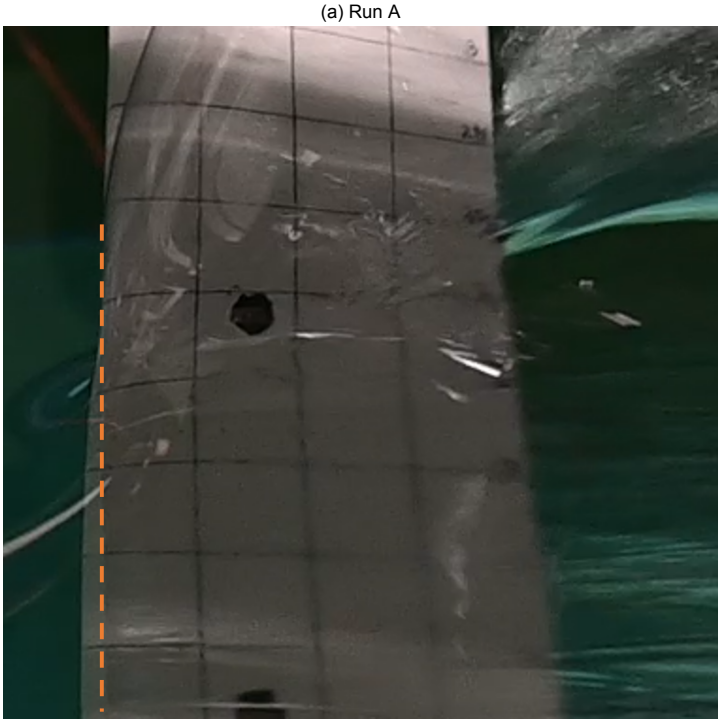

(b) Run B

Figure 6.22: Snapshot of video pre- and post-ventilation for identical runs A and B. Operational condition 60° roll and 12° AoA. For a NACA0012 surface-piercing hydrofoil, AR 3.46, Re $3.42 \cdot 10^5$

Based on the results shown in this section no correlation between pressure and ventilation is found. The response of pressure sensors close to the free-surface is too unstable. At this point, it is not known if this is due to a measuring error or has a physical explanation. Too little ventilation runs exist to verify this. The fact that from the time trace of the pressure sensors, the response showed

fluctuations and a dip in response is promising that in the future a correlation to ventilation can be found.

7

Discussion

The overall tendency is that with a larger data set the analysis would have been better and the conclusion stronger. At times the results themselves are ambiguous making it difficult to draw the correct conclusion. The results are almost all one-shot results. The fact that the chord-wise pressure reconstruction for all span-wise locations yields a similar and reasonable resemblance to Xfoil, indicates that the method is working.

The high roll experiments are executed without specific stepped-runs before each measuring run. There is not enough space to translate the foil that much, without placing the pressure tappings above the waterline, to be prevented at all times. The calibration factor imposed is the averaged found calibration factor of all stepped-runs of the vertical configuration. There is no prior check carried out to see if for some reason a sensor became faulty in between swapping from vertical to high angled bracket. Apart from the one outlier data point mentioned in the results chapter, the results do not indicate a faulty sensor. It would be better to be able to say this with certainty.

Based on the results of ventilation runs the percentage difference of the upper and lower array are depicted in table 6.8. The percentage difference between the two runs is significantly smaller for the lower array. This suggests that for increased submergence the results become more stable. For increased submergence, the disturbance of the free-surface is less. Interesting to investigate when more ventilation runs are available is the reliability of a pressure array plotted against its submergence. One of the proposed benefits of the use of pressure tappings was the larger operational condition range than PIV. The PIV method is not suitable to scan a high rolled model due to the camera and laser angles and close to the free-surface due to reflection. If this method does not yield reliable results in the proximity of the free surface, it loses value.

During the experimental phase, the model was taken out of the water each night to prevent corrosion. Every morning all tubes and sensors were bled by hand. The last part of the tube is not see-through, it can be that a tiny air bubble was left in there at times. Even though great care was taken in this bleeding, and also checks were carried out before starting the experimental runs. Having a system that bleeds all sensors the same, would be a benefit. Having a model that does not need to be taken out of the water would be even better.

The potential effect of tube length on the pressure reading is not tested. Based on the time trace of the ventilation run, it appears that the length of the tubes does not have a negative effect on the response as it is rapid. In this test set-up now the PCB’s with sensors were mounted outside, but rather close, to the foil. There was approximately 20 cm slack in the tubes, reducing the slack could possibly already make a difference in the response. Since in other research, the effect of tube length is mentioned, it might be worth it to check if it matters.

Increasing the robustness of the method would be an improvement. This can be done by including more pressuring tappings in the model in both chord-wise and span-wise pressure distribution. The downside of this is a model that becomes really large and the incoming data might become an

overload. Now only having 15 pressure tappings per array and needing to exclude some outliers left few data points to make a fit trough. Now only two data points exist inside the pressure peak. If this pressure sensor or connecting tube for some reason is damaged or the connection becomes a bit lose during a run, the consequence is serious. Adding more tappings would benefit the post-processing, but might not change the results.

In the future, instead of fitting with LSQ compressed sensing can be used to reconstruct the pressure distribution. With the use of compressed sensing, a high-resolution reconstruction can be obtained from a very sparse data set. Within the time frame of this thesis, this was not feasible. Another paper has shown promise of pressure reconstruction of a sparse data set using compressed sensing (Zhao et al., 2022). Based on the results presented in this thesis the possibility of using CS can already be explored.

8

Conclusion

This study examined if *"a full surface pressure reconstruction made with pressure tappings aid the search to correlate pressure and ventilation"*. The answer is found with the use of four supporting sub-questions.

The first sub-goal, was to determine how repeatable this method is. On sensor level it was found that too many sensors had a percentage difference above 10%. On array level the maximum difference found is 2.5%. The cross-check between the upper and lower array yields a too large difference for 5 out of 18 checked sensors, this is more than a quarter and thus this is not a reliable result. On array level the cross-check yielded a maximum difference of 1.21%. Based on the available results, the conclusion is drawn that for the purpose of finding a correlation to ventilation, the difference is too large and thus the precision too low. Using this method to make further computations on the hydrodynamics, array level, the precision is deemed high enough.

The second sub-question 'How do the experimental results compare to known data?', is answered based on the data from section 6.2. It was found that the pressure measurements show the same trend as comparable data does, but a pressure peak is lower. The pressure measurements from the experiments are under predictions of Xfoil pressure distribution. After correcting the Xfoil results for finite length and free-surface interaction, the resulting pressure peak value came close together. The trend of the pressure reconstruction over the chord matches the numerical prediction of Xfoil. A comparison based on C_L is made, using the pressure reconstruction, the force measurement, an empirical method and the Xfoil prediction. The result of comparing the C_L with force measurements and empirical method is ambiguous as for AoA 8° or 12° one of the methods matches and the other is off by a maximum 13.4%. The comparison to the corrected Xfoil simulation yielded a mismatch of 2 and 5%. This is for both operational conditions in the same order of magnitude. Based on the available results it is concluded that the pressure reconstruction at 0 °roll angle is in good agreement with known data.

The sub-question *"Does the method yield valid results when the foil operates under high roll angles?"*, is answered based on results of section 6.3. The made pressure reconstructions are comparable to those of the vertical configuration. For shallow measurements (z/c=0.21 and z/c=0.54) the pressure coefficient rapidly approaches zero. This close to the free-surface little suction pressure is expected. The quality of the pressure readings at 60° roll are not inferior to those at 0° roll. It is not the operational condition which influences the quality of the measurements, the answer to this sub-question is thus "yes".

The last sub-question 'If there is ventilation, can a correlation to the pressure distribution be found?' is answered using the data from section 6.4. There is no correlation found, which indicated ventilation. It was seen that the three sensors closest to the leading edge either showed fluctuation just before the pressure rises massively due to the ventilation. This was either a dip in pressure, and one-time trace showed an oscillating measurement. A correlation based on these results is not found.

The results of this study cannot confirm the hypothesis that a full-surface pressure reconstruction made with pressure tapping can aid in the search to correlate ventilation to pressure. The results do show a high promise that this will be possible in the future, with a follow-up research. The precision of the sensor response is not satisfactory. Pressure reconstructions showed to be in enough agreement to known data and the quality of the measurement has proven to not be affected by the operational condition. The large promise for the future is shown by the time-trace of the sensors during ventilation runs. The answer to the research question *”Can a full surface pressure reconstruction made with pressure tappings aid the search to correlate pressure and ventilation?”* is a no for now.

Bibliography

Abbott, I. H., & Von Doenhoff, A. E. (2012). *Theory of wing sections: Including a summary of airfoil data*. Courier Corporation.

Acosta, A. (1973). Hydrofoils and hydrofoil craft. *Annual Review of Fluid Mechanics*, *5*(1), 161–184.

Akhlaghi, H., Soltani, M., & Maghrebi, M. (2020). Laminar-turbulent intermittency measurement based on the uncalibrated hot-film data. *Measurement*, *156*, 107575.

Amsterdam airport schiphol. (2022). https://meteostat.net/en/station/06240?t=2022-06-22%5C%2F2022-07-15

Ashworth Briggs, A. J. E. (2018). *Free surface interaction of a 't-foil'hydrofoil* (Doctoral dissertation). University of Tasmania.

Bani-Hani, E. H., & Assad, M. E. H. (2018). Boundary-layer theory of fluid flow past a flat-plate: Numerical solution using matlab. *International Journal of Computer Applications*, *975*, 8887.

Barden, T., & Binns, J. (2012). On the road to establishing ventilation probability for moth sailing dinghies barden. *18 th Australasian Fluid Mechanics Conference*, *2012*.

Bartesaghi, S., Provinciali, G., & Lovato, F. (2022). Kite foil mast ventilation study. *The 9th Conference on Computational Methods in Marine Engineering (Marine 2021)*.

Binns, J. R., Brandner, P. A., & Plouhinec, J. (2008). The effect of heel angle and free-surface proximity on the performance and strut wake of a moth sailing dinghy rudder t-foil.

Binns, J., Albina, F., & Burns, I. (2009). Looking for "laminars": Measuring intermittency on the america's cup race course. *Experimental thermal and fluid science*, *33*(5), 865–874.

Breslin, J. P., & Skalak, R. (1959). *Exploratory study of ventilated flows about yawed surface-piercing struts* (tech. rep.).

Cfd support. (n.d.). https://www.cfdsupport.com/OpenFOAM-Training-by-CFD-Support/node334.html

Chakroun, W., Al-Mesri, I., & Al-Fahad, S. (2004). Effect of surface roughness on the aerodynamic characteristics of a symmetrical airfoil. *Wind Engineering*, *28*(5), 547–564.

Damley-Strnad, A., Harwood, C. M., & Young, Y. L. (2019). Hydrodynamic performance and hysteresis response of hydrofoils in ventilated flows. *Sixth International Symposium on Marine Propulsors (SMP'19)*.

Delafin, P., Deniset, F., & Astolfi, J. (2014). Effect of the laminar separation bubble induced transition on the hydrodynamic performance of a hydrofoil. *European Journal of Mechanics - B/Fluids*, *46*, 190–200. https://doi.org/https://doi.org/10.1016/j.euromechflu.2014.03.013

Drela, M. (1989). Xfoil: An analysis and design system for low reynolds number airfoils. In *Low reynolds number aerodynamics* (pp. 1–12). Springer.

Drela, M., & Giles, M. B. (1987). Viscous-inviscid analysis of transonic and low reynolds number airfoils. *AIAA journal*, *25*(10), 1347–1355.

Drela, M., & Youngren, h. (2001). Xfoil user primer. https://web.mit.edu/drela/Public/web/xfoil/xfoil_doc.txt

Durst, F. (2008). *Fluid mechanics: An introduction to the theory of fluid flows*. Springer Science & Business Media.

Editor. (2020). Charal imoca 60: V2 foils in action. https://www.catsailingnews.com/2020/06/charal-imoca-60-v2-foils-in-action.html

Ellsworth, W. M. (1967). *The us navy hydrofoil development program.* (tech. rep.). DAVID TAYLOR MODEL BASIN WASHINGTON DC.

Fridsma, G. (1963). *Ventilation inception on a surface-piercing dihedral hydrofoil with plane-face wedge section* (tech. rep.). STEVENS INST OF TECH HOBOKEN NJ DAVIDSON LAB.

Harwood, C. M., Brucker, K. A., Miguel, F., Young, Y. L., & Ceccio, S. L. (2014). Experimental and numerical investigation of ventilation inception and washout mechanisms of a surface-piercing hydrofoil. *30th Symposium on Naval Hydrodynamics*.

Harwood, C. M., Young, Y. L., & Ceccio, S. L. (2016). Ventilated cavities on a surface-piercing hydrofoil at moderate froude numbers: Cavity formation, elimination and stability. *Journal of Fluid Mechanics*, *800*, 5–56.

Hoerner. (1976). Fluid-dynamic drag: Practical information on aerodynamic drag and hydrodynamic resistance. sf hoerner. hoerner fluid dynamics, brick town, new jersey. 1965. 455 pp. illustrated. 24.20.. *The Aeronautical Journal*, *80*(788), 371–371.

Hoerner & Borst, H. V. (1975). Fluid-dynamic lift: Practical information on aerodynamic and hydrodynamic lift. *NASA STI/Recon Technical Report A*, *76*, 32167.

Jacobi, G., Thill, C., & Huijsmans, R. (2016). The application of particle image velocimetry for the analysis of high-speed craft hydrodynamics. *Conference on Hydrodynamics-ICHD*, 62.

Jahanmiri, M. (2011). Laminar separation bubble: Its structure, dynamics and control.

Jentzsch, M., Schmidt, H.-J., Woszidlo, R., Nayeri, C., & Paschereit, C. (2021). Challenges and procedures for experiments with steady and unsteady model velocities in a water towing tank. *Experiments in Fluids*, *62*. https://doi.org/10.1007/s00348-021-03151-5

Kermeen, R. W. (1956). Water tunnel tests of naca 4412 and walchner profile 7 hydrofoils in noncavitating and cavitating flows.

Kiceniuk, T. (1954). A preliminary experimental study of vertical hydrofoils of low aspect ratio piercing a water surface.

Kuester, M. S., Borgoltz, A., & Devenport, W. J. (2016). Pressure tap effects on the lift measurement of an airfoil section. *32nd AIAA Aerodynamic Measurement Technology and Ground Testing Conference*, 3654.

Michel, W., Hoerner, S., Ward, L., & Buermann, T. (1954). *Hydrofoil handbook. volume 2. hydrodynamic characteristics of components* (tech. rep.). GIBBS and COX INC NEW YORK.

Moran, J. (2003). *An introduction to theoretical and computational aerodynamics*. Courier Corporation.

Muratoglu, A., Yuce, M., & Eşit, M. (2016). Foil generation inspiring from nature.

Parkin, B. R., Perry, B., & Wu, T. Y.-t. (1956). Pressure distribution on a hydrofoil running near the water surface. *Journal of Applied physics*, *27*(3), 232–240.

Perry, B. (1954). Experiments on struts piercing the water surface.

Pinkerton, R. M. (1938). *The variation with reynolds number of pressure distribution over an airfoil section* (tech. rep.). US Government Printing Office Washington, WA, USA.

Pope, A. (1951). *Basic wing and airfoil theory*. McGraw-Hill.

Ragni, D. (2012). Piv-based load determination in aircraft propellers.

Rothblum, R. S. (1969). *Ventilation, cavitation and other characteristics of high speed surface-piercing struts*. Department of the Navy, Naval Ship Research; Development Center.

Russell, J. M. (1979). Length and bursting of separation bubbles: A physical interpretation. *NASA. Langley Res. Center The Sci. and Technol. of Low Speed and Motorless Flight, Pt. 1*.

Schreier, S., & Poelma, C. (2018). A new generation of sloshing pressure sensors. *The 28th International Ocean and Polar Engineering Conference*.

Schwerter, M., Leester-Schädel, M., & Dietzel, A. (2017). Waterproof sensor system for simultaneous pressure and hot-film flow measurements. *Sensors and Actuators A: Physical*, *257*, 208–215.

Speer, T. (2004). Xfoil for hydrofoils. https://www.boatdesign.net/threads/xfoil-for-hydrofoils.2909/

Sreejith, B., & Sathyabhama, A. (2020). Experimental and numerical study of laminar separation bubble formation on low reynolds number airfoil with leading-edge tubercles. *Journal of the Brazilian Society of Mechanical Sciences and Engineering*, *42*(4), 1–15.

Swales, P., Wright, A., McGregor, R., & Rothblum, R. (1974). The mechanism of ventilation inception on surface piercing foils. *Journal of Mechanical Engineering Science*, *16*(1), 18–24.

Timmerman, N. (2017). 4. pressure distributions and flow separation. https://ocw.tudelft.nl/course-lectures/4-pressure-distributions-flow-separation/

Tinney, E. R. (1954). Experimental and analytical studies of dihedral hydrofoils, 13–17.

Towing tank no. 1. (n.d.). https://www.tudelft.nl/3me/over/afdelingen/maritime-and-transport-technology/research/ship-hydromechanics/facilities/towing-tank-no-1

Traub, L. W., & Cooper, E. (2008). Experimental investigation of pressure measurement and airfoil characteristics at low reynolds numbers. *Journal of aircraft*, *45*(4), 1322–1333.

Wadlin, K. L. (1958). Mechanics of ventilation inception.

Wadlin, K. L., Ramsen, J. A., & Vaughan Jr, V. L. (1954). *The hydrodynamic characteristics of modified rectangular flat plates having aspect ratios of 1.00 and 0.25 and operating near a free water surface* (tech. rep.).

Waid, R. L. (1968). *Experimental investigation of the ventilation of vertical surface-piercing struts in the presence of cavitation* (tech. rep.). LOCKHEED MISSILES and SPACE CO INC SUNNYVALE CA.

Wetzel, J. (1957). Experimental studies of air ventilation of vertical semi-submerged bodies.

Williams, M., Kawakami, E., Amromin, E., Hambleton, W., & Arndt, R. (2008). Effects of surface characteristics on hydrofoil cavitation.

Winslow, J., Otsuka, H., Govindarajan, B., & Chopra, I. (2018). Basic understanding of airfoil characteristics at low reynolds numbers (104–105). *Journal of Aircraft*, *55*(3), 1050–1061. https://doi.org/10.2514/1.c034415

Young, Y. L., Harwood, C. M., Miguel Montero, F., Ward, J. C., & Ceccio, S. L. (2017). Ventilation of lifting bodies: Review of the physics and discussion of scaling effects. *Applied Mechanics Reviews*, *69*(1).

Zhao, X., Deng, Z., & Zhang, W. (2022). Sparse reconstruction of surface pressure coefficient based on compressed sensing. *Experiments in Fluids*, *63*(10), 1–18.

A

Fluid mechanics

Fluid mechanics is the term given to a field of studies on motions and forces in fluids. A fluid being all gasses and liquids of which air and water are the fluid materials at interest regarding surface piercing hydrofoils. To visualize a fluid, streamlines are used. These show the motion (direction) of fluid (particles) in space. Note that in fluid mechanics, terms are often described per unit volume. The forces on a set control volume or object in a fluid are divided into surface and body forces. The surface forces are either normal or tangential, of which the normal force is often referred to as pressure and the tangential force as shear stress or viscous stress. A body force can be gravity, cordials, magnetic, etc. however these are commonly not present in hydrofoil analysis.

In fluid mechanics, two perspectives for analysis exist (1) the Lagrangian where the moving particle is followed, and (2) the Eulerian where there is a fixed box through which the particles pass. The Eulerian method is used because it resembles the testing environment even though it yields more complex equations (Durst, 2008). To describe a fluid, the following terms are often used: compressibility and viscosity. A fluid, to an, extend is, always compressible. Gas is very compressible, water is not that compressible and an object is even less compressible. Water is in this study deemed incompressible. When exerting a force on the water the volume does not shrink significantly, which makes the assumption of an incompressible fluid viable, at least for the practical purposes of this research. Viscosity expresses the capability of a fluid to resist against a deformation, as will be highlighted in this section viscosity cannot be neglected in a boundary layer, but far away from a surface, the flow may be assumed inviscid. The sectrefsec:fluidmechanics:fluidnumbers will show the importance of the Reynolds number regarding viscosity.

In sectionA.0.1, some fluid numbers are described which are used throughout the report. The governing equations, from the Eulerian perspective, are given in section A.0.2. Lastly a fluid flow can be categorised as laminar or turbulent. What this comprehends and the importance of it, is given in section A.0.3.

A.0.1. Fluid terms

A quick description and equation is given on four fluid numbers named after their inventor.

Euler number

The Euler number gives the ratio of pressure versus inertia. The formula of the Euler number is given in equation A.1, where Δp denotes the change in pressure, ρ the density of the fluid and u the velocity of the fluid. In the formulations of lift and drag coefficients the Euler number is visible.

$$Eu = \frac{\Delta p}{\rho u^2} \tag{A.1}$$

Froude number
The Froude number relates the weight to the inertia, to describe the behaviour of the free surface as waves and wake. In equation A.2 the Froude number based on length is given, in which g represents the gravitational acceleration and L is the characteristic length of the object.The Froude number is famously known for it's scaling capabilities, and often used when making ship models on scale for scientific research. Froude number is also often used as a way to express velocity in research, since this is a dimensionless number.

$$Fn = \sqrt{\frac{u^2}{gL}} \tag{A.2}$$

Weber number
The Weber number describes the surface tension based on the inertia, the formulation is given in equation A.3. At the junction of two types of fluid, there is a surface. The force it takes two break trough this surface is called the surface tension and it is denoted by σ. The Weber number is of interest since it is the breaking of a surface which enables a pathway for the ingress of air in ventilation.

$$We = \frac{\rho u^2 L}{\sigma} \tag{A.3}$$

Reynolds number
Lastly a very important number, the Reynolds number relates viscosity to inertia and the formulation is given in equation A.4. The dynamic viscosity is denoted by μ, and L is the reference length of an object and u the speed.

$$Re = \frac{\rho u L}{\mu} \tag{A.4}$$

A fluid has viscosity, but often a fluid is deemed inviscid for simplification. By making this assumption some of reality gets lost. The Reynolds number can give an idea of the importance of viscosity, at very high Reynolds numbers the viscosity becomes of lesser importance. Reynolds number aids scaling from full scale to model scale tests, to ensure fair comparison. Reynolds number determines some physic effects, thus when computing or experimenting the result may not be extrapolated beyond the tested Reynolds number range. Michel et al., 1954

A.0.2. Conservation laws/governing equations

The three basic principles in fluid mechanics are the conservation of mass, conservation of momentum and the conservation of energy, all three often recalled as the conversation laws. Moran, 2003

Conservation of mass
In a fixed observation volume in a fluid flow, the amount of flow entering the volume equals the amount of flow leaving the volume, thus a fluid is continuous. The conservation of mass is therefore sometimes referred to as the continuity equation. The conservation of mass states as much as that within a controlled volume, mass can not be created nor destroyed. A controlled volume zone is shown in figure A.1, which will help illustrate how the continuity equation is built up.

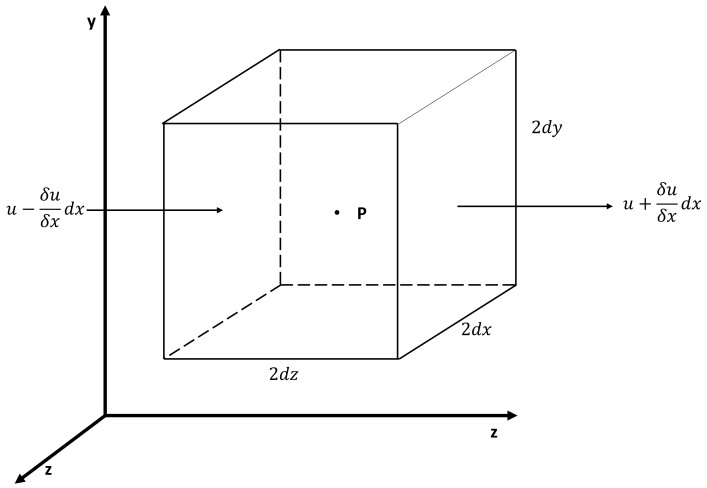

Figure A.1: Visualisation of the conservation of mass using a controlled volume around a fixed point Pope, 1951

The velocity of the fluid is u,v,w in respectively the x,y and z direction. A 1D fluid flow is drawn in x direction and the volume size is $dx \cdot dy \cdot dz$. For mass not to be created nor destroyed the outgoing mass flow rate minus the incoming mass flow rate must be the negative change in volume mass. The simplification for a 1D flow is shown in equation A.5

$$\dot{m}_2 - \dot{m}_1 = -\dot{m}_{volume} = u_2\rho_2 dxdy - u_1\rho_1 dxdy = -\frac{d\rho}{dt} dxdydz \tag{A.5a}$$

$$\Delta(\rho u)dydz = -\frac{d\rho}{dt} dxdydz \tag{A.5b}$$

In a control volume, the flow can enter and exit in x, y and z direction, whilst the mass of the volume must stay the same. This gives the 3D conservation of mass equation as below, after simplification by dividing through the volume the continuity equation is obtained.

$$\Delta(\rho u)dydz + \Delta(\rho v)dydx + \Delta(\rho w)dydx = -\frac{d\rho}{dt} dxdydz \tag{A.6a}$$

$$\frac{\Delta(\rho u)}{\Delta x} + \frac{\Delta(\rho v)}{\Delta y} + \frac{\Delta(\rho w)}{\Delta z} = -\frac{\Delta\rho}{\Delta t} \tag{A.6b}$$

To further simplify this, two additional assumptions are made. The cube has a finite size, now the cube is thought of as infinitesimally small, which turns the derivatives into partial derivatives. Next to that we assume an incompressible flow, meaning density stays constant over time and all derivatives of the density can be set to one. This leads to the equation (eq. A.7) for the conservation of mass for an incompressible flow.

$$\frac{\partial u}{\partial x} + \frac{\partial v}{\partial y} + \frac{\partial w}{\partial z} = 0 \tag{A.7}$$

Note: in a 2D problem the z components are eliminated from the equation.

Conservation of momentum

The conservation of momentum is based on Newtons third law ($F = m \cdot a$), where the change in momentum is the density multiplied by the change of velocity over time and the force is made up of a

pressure force, a viscosity force and a body force. In short, this boils down to the equation shown in A.8

$$\rho \frac{Du}{Dt} = -\nabla \rho + \mu D^2 u + \rho g \tag{A.8}$$

In equation A.9 the conservation of momentum for an incompressible fluid is given. These equations are also known as the Navier-Stokes equations. These equation are not solvable, after making the needed assumptions a close approximation can be made.

$$\rho\left(\frac{\partial u}{\partial t} + u\frac{\partial u}{\partial x} + v\frac{\partial u}{\partial y} + \omega\frac{\partial u}{\partial z}\right) = -\frac{\partial P}{\partial x} + \mu\left(\frac{\partial^2 u}{\partial x^2} + \frac{\partial^2 u}{\partial y^2} + \frac{\partial^2 u}{\partial z^2}\right) + \rho a_x \tag{A.9a}$$

$$\rho\left(\frac{\partial v}{\partial t} + u\frac{\partial v}{\partial x} + v\frac{\partial v}{\partial y} + \omega\frac{\partial v}{\partial z}\right) = -\frac{\partial P}{\partial y} + \mu\left(\frac{\partial v}{\partial x^2} + \frac{\partial v}{\partial y^2} + \frac{\partial^2 v}{\partial z^2}\right) + \rho a_y \tag{A.9b}$$

$$\rho\left(\frac{\partial v}{\partial t} + u\frac{\partial w}{\partial x} + v\frac{\partial v}{\partial y} + \omega\frac{\partial v}{\partial z}\right) = -\frac{\partial P}{\partial z} + \mu\left(\frac{\partial w}{\partial x^2} + \frac{\partial^2 v}{\partial y^2} + \frac{\partial^2 w}{\partial z^2}\right) + \rho a_z \tag{A.9c}$$

In vector notation for a 3D space the conservation of momentum is written in equation A.10

$$\frac{\partial \rho}{\partial t} + \nabla \cdot (\rho \vec{V}) = 0 \tag{A.10}$$

Conservation of energy
The conservation of energy is not as commonly referred to in fluid dynamics, but better known under the name ”Bernoulli equation”. The conversation of energy means that energy cannot be destroyed or created. The equation states that the potential plus kinetic energy at one moment in time must equal the potential plus kinetic energy at another moment in time. In other words, the change kinetic plus potential energy is zero, which results in the following equation.

$$KE_1 + PE_1 = KE_2 + PE_1 = \frac{1}{2}mv_1^2 + mgh_1 = \frac{1}{2}mv_2^2 + mgh_2 \tag{A.11a}$$

$$\Delta KE + \Delta PE = constant \tag{A.11b}$$

The conservation of energy holds for a solid and a fluid, but the famously known Bernoulli equation only holds for a perfect fluid.

$$p + \frac{1}{2}\rho v^2 + \rho g z = constant \tag{A.12}$$

Bernoulli’s equation holds for incompressible, irrotational, inviscid flow.

A.0.3. Flow regime

An external flow is open on one or more sides and often exhibits a change in the stream wise direction. External flows exist in the form of a boundary layer (a velocity gradient near a solid surface), wakes (a velocity deficit region often unsteady and downstream of a body moving in fluid) and shear layers (where two flows with a different velocity come together). The boundary layer will be discussed in greater detail for both laminar and turbulent flows. Figure A.2 shows both the laminar and turbulent flow.

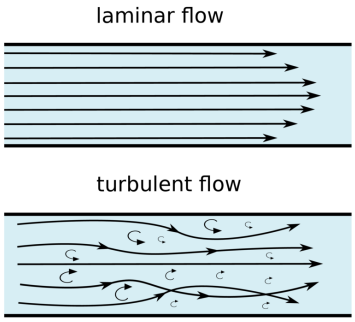

Figure A.2: Laminar vs Turbulent flow over a cylinder (“CFD support”, n.d.)

A laminar flow is recognised by parallel and smooth streamlines. Laminar flow is assumed to be irrotational and has a predictive behaviour which can be captured analytically. It is also called a steady flow, which means as much as when a velocity or pressure gradient is made trough the fluid on a certain plane this will be equal at two different time incidents. A turbulent flow is recognised by being highly chaotic and looking random, and may not be assumed irrotational. Turbulent flow is however not random, since it does follow laws and rules of physics. A flow transitions to turbulent when the inertia of the flow exceeds the ability to respond. The critical Reynolds number (Re_{crit}) gives a value for a specific geometry at which the flow around it turns turbulent. A turbulent flow, opposite to laminar flow, is unsteady, the velocity profile is not smooth and continuous.

Solving turbulent flow analytically is not possible since from the Navier-stokes equation only the body force can be assumed zero thus the following equation is left.

$$\rho\left(\frac{\partial u}{\partial t}+u\frac{\partial u}{\partial x}+v\frac{\partial u}{\partial y}+\omega\frac{\partial u}{\partial z}\right)=-\frac{\partial P}{\partial x}+\mu\left(\frac{\partial^2 u}{\partial x^2}+\frac{\partial^2 u}{\partial y^2}+\frac{\partial^2 u}{\partial z^2}\right) \tag{A.13}$$

In theory turbulent flow is solved with the combination of computational fluid dynamics (CFD), model scale experiments and full scale tests. This combination aids in building predictive/empirical models.

Boundary layer

The boundary layer is the space around the fluid which is effected by viscosity. Viscosity introduces friction at the surface which effects the fluid velocity. Fluid at the surface has zero velocity due to the no-slip boundary condition (due to friction the first layer of fluid and the body must have the same velocity at the surface), moving away from the surface the velocity gradually increases due to the decrease of the friction effect. This leaves a velocity gradient within the boundary layer as shown in figure A.3 for a laminar and turbulent flow.

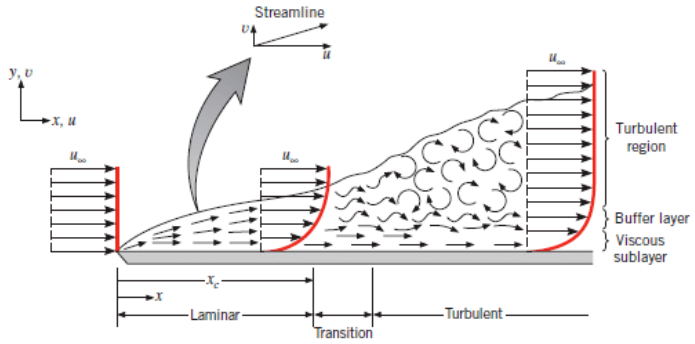

Figure A.3: Boundary layer velocity field (Bani-Hani and Assad, 2018)

Note that the turbulent velocity field is a time averaged one, since a single snapshot would show high

unsteadiness. The turbulent flow has a fatter profile (seen in the more rapid velocity increase) than the laminar one. A physical explanation for this faster increase of velocity moving up from the surface lies in the chaotic behaviour of turbulent flow. The whirling characteristic act as a mixer of flow, leading higher velocity moving particles downward. With, as a result, an increased velocity gradient compared to the laminar profile. The boundary layer is smaller for a turbulent flow than a laminar flow. Durst, 2008

The friction introduces shear stresses at the foil surface. For laminar flow this can be computed as the partial derivative of the fluid velocity over the boundary layer thickness multiplied by the viscosity as shown in equation A.14.

$$\tau_{wall} = \mu \frac{\partial u}{\partial y}|_{y=0} \tag{A.14}$$

For a turbulent flow, empirical models are used to estimate the shear stresses. It is not possible to compute the transition point from laminar to turbulent analytical, thus this must be tested via experiments or computed with CFD.

B

Analytical methods

Analytical methods are of use to compute hydrodynamic loads and behaviour of foils. In analytical analysis 2D potential flow is assumed, which means an idealised flow: inviscid, irrotational and incompressible. A potential flow is written as follows, where φ must satisfy the continuity equation.

$$V = \nabla\varphi \tag{B.1}$$

Several analytical methods exist to compute the pressure distribution over a foil, all with their own assumptions and limitations. In this chapter, some of them are discussed. First the Kutta-Joukowski transformation is explained since this transformation forms the base for the ”thin” and ”thick” foil theory. The thin foil theory can be used for calculations on symmetrical foils and the thick method also for cambered foils. The 2D panel method is also discussed. This forms the base of the program Xfoil.

B.0.1. Kutta-Joukowski transformation

The Kutta-Joukowski transformation, transorms a circle into a foil shape. Since the equation to describe the flow around a circle is known (eq. B.2), this transformation will yield an equation to describe the flow around a foil. Equation B.2 shows the potential function in which *a* is the radius of the circle and Γ the circulation.

$$w = -V\left(z + \frac{a^2}{z}\right) - \frac{i\Gamma}{2\pi}\ln\frac{z}{a} \tag{B.2}$$

The velocity of a point on the surface of the circle as a function of the angle in a uniform incoming flow is given in equation B.3.

$$q_z = q_\theta = 2V\sin\theta + \frac{\Gamma}{2\pi r} \tag{B.3}$$

Both Kutta and Joukowski independently came up with the idea to find a way to transform a circle into a foil geometry and with that transform the flow equation. The result being an expression for the flow around a foil. The transformation is given in equation B.4, where the circle is given in the z-plane and the transformed foil in the ζ-plane.

$$\zeta = z + \frac{c_1^2}{z} \tag{B.4a}$$

If, $z = re^{i\theta}$ and $\zeta = \xi + i\eta$ (B.4b)

$$\xi + i\eta = re^{i\theta} + \frac{c_1^2}{r}e^{-i\theta} \tag{B.4c}$$

(B.4d)

This can be rewritten into a real and an imaginary part in the two unit vectors;

$$\xi = \left(r + \frac{c_1^2}{r}\right)\cos\theta \tag{B.5a}$$

$$\eta = \left(r - \frac{c_1^2}{r}\right)\sin\theta \tag{B.5b}$$

The placement of the circle center in the z-plane determines the output geometry of the foil. When the center is at $(x, y) = (0, 0)$, the transformation will yield a flat plate. When the origin is at $(x, y) = (> 0, 0)$ a symmetrical foil will be generated. For origin $(x, y) = (0, > 0)$ a circular arc is generated and a cambered foil is computed hen the origin of the circle is at $(x, y) = (> 0, > 0)$. Pope, 1951

For a symmetrical foil, the transformation is graphically displayed in figure B.1. Since the foil is transformed from a circle of which each point can be described by $theta$, all points on the foil can be described by theta. The upper surface going from 0 to 180 degrees and the lower surface from 0 to -180. Once the velocity in the transformed point is known, the corresponding pressure coefficient can be computed.

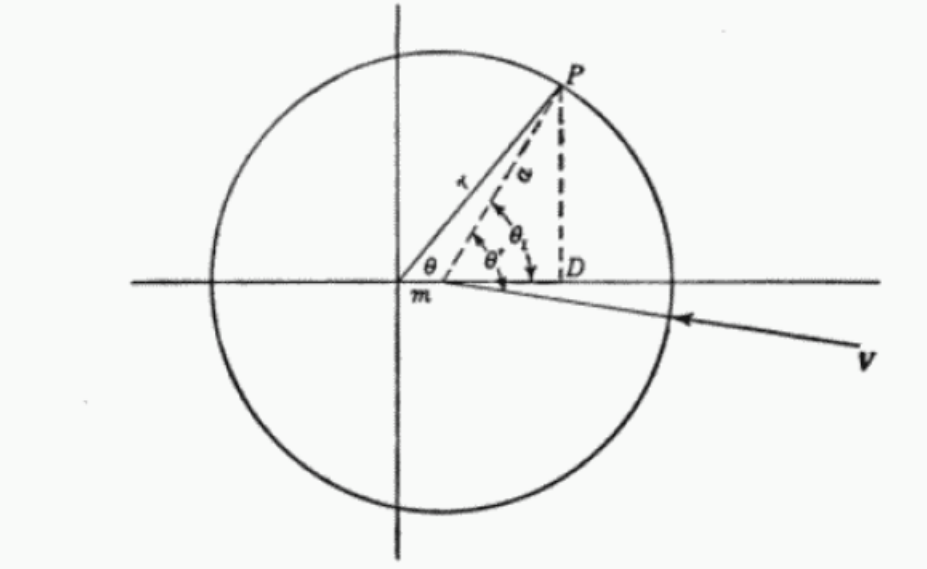

Figure B.1: Graphic display of needed cicrcle geomtery to obtain a symmetrical foil

The computational method for the symmetrical foil is explained here. The velocity of the circle is known (eq. B.3, only the radius r doesn't equal a anymore since the circle is translated a bit. Thus, the velocity equation of the circle becomes of term a, also the angle is corrected for the angle of the inflow. In the equation of the circulation the difference in angle due to the angle of the inflow is the

angle of attack denoted by α. The velocity in the $zeta$-plane is obtained when $d\zeta/dz$ is known, after which the pressure coefficient at all points on the surface of the foil can be calculated. This is shown in equations B.6, in which V is the speed of the foil, and q_ζ the velocity of the transformed point.

$$q_z = 2V \sin\theta' + \frac{\Gamma}{2\pi a} \tag{B.6a}$$

$$\text{With, } \Gamma = 4\pi a V \sin(\alpha + \beta) \tag{B.6b}$$

$$q_\zeta = \frac{|q_z|}{\left|\frac{d\zeta}{dz}\right|} \tag{B.6c}$$

$$\left|\frac{d\zeta}{dz}\right| = \left|\sqrt{1 - \frac{c_1^4 \cos(2\theta)^2}{r^4} + \frac{c_1^4 \sin(2\theta)^2}{r^4}}\right| \tag{B.6d}$$

$$\text{With, } r = c_1 + m + m \cdot cos(\theta) \text{ and } c_1 \approx c/4 \tag{B.6e}$$

(B.6f)

$$Cp = 1 - \left(\frac{q_\zeta}{V}\right)^2 \tag{B.6g}$$

This theory can provide shape and pressure distributions. Based on a method which only requires 4 geometry parameters to yield a pressure distribution: chord length, percent thickness, camber factor and angle of attack. The downside is that there is a limit on the shapes that can be generated, only symmetrical, circular arc, and simple cambered foils. Thus the exploration into more complex shapes is not possible in this method.

B.0.2. Thin foil theory

Munk, Glauert and Birnbaum are responsible for the thin foil theory, which states that the thickness of the foil contributes very little to the lift. Thus in the thin foil theory, a foil is described by a single curve Pope, 1951. This mean line is for a symmetrical foil equal to the chord line, otherwise it is the camber line. In figure B.2 the foil as represented by a mean line is shown. The thin foil method yields a fast prediction of the lift of a foil since it was found that the lift with respect to the angle of attack is proportional to a ratio of 2π.

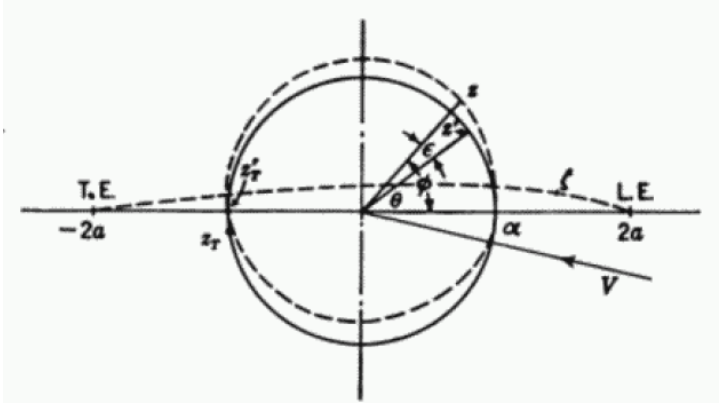

Figure B.2: Transformation of foil for thin foil theory. Pope, 1951

Note that in this figure two circles are drawn, a true circle described by z and a pseudo circle described by z'. For the transformation, the cambered mean line is transformed into a pseudo circle, which in its turn is transformed into a circle (of which we know the velocity equation). The angle related to the pseudo circle is Φ and to the circle is θ. The difference between those angles to describe a corresponding point is ϵ, which is assumed to be small. Also the difference in radii (r) is assumed to be small. The velocity at any point on the foil (q_ζ) is described by equation B.7

$$q_\zeta = V\left[1 + (\alpha + \epsilon)\cot\theta + (\alpha + \epsilon_T)\csc\theta + \frac{d\epsilon}{d\theta}\right] \tag{B.7}$$

The value of ϵ_T depends on constants which are found in empirical tables/graphs. To obtain the pressure distribution, the thin foil theory requires tables and charts, therefore the thick foil theory might be of better use.

B.0.3. Thick airfoil theory

The thick foil theory is the extended work of Theodorsen based on the thin foil theory. The thin foil theory requires prior knowledge on the shape in the form of charts and tables, the thick foil enables to solve for arbitrary foil shapes. It is a more complex method, but worth it in the end. Let the foil be in the ζ plane, then by using the Joukowski method in reverse a psuedo circle in the z' plane is obtained, which is than transformed to the circle in z plane. This is graphically shown in figure B.3.

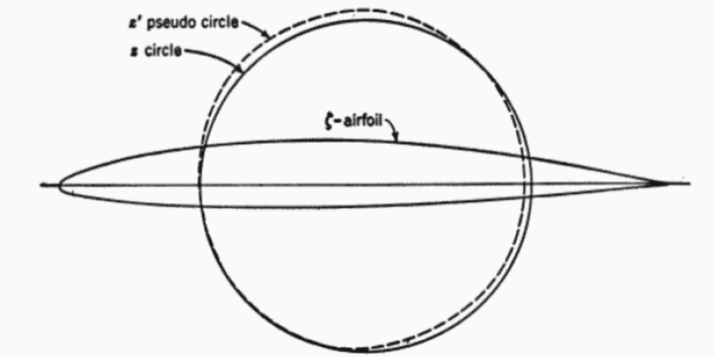

Figure B.3: Graphic display of tranformation used in thick airfoil theory Pope, 1951

Let the foil be described by $\zeta = x + iy$ and the circle by $z = ae^{\Psi_0}e^{i\varphi}$ of which *a* is a constant and Ψ_0 is assmued so small that the exponent of it is equal to 1 that the psuedo circle is described by $z' = ae^{\Psi}e^{i\theta}$.

To relate θ of the psuedo circle to the foil, the following equation is used.

$$2\sin^2\theta - p = \sqrt{p^2 + \left(\frac{y}{a}\right)^2} \tag{B.8}$$

In which p is represented by the formula :

$$p = 1 - \frac{x^2}{4a^2} - \frac{y^2}{4a^2} \tag{B.9}$$

For every point on the foil expressed in x,y the corresponding angle θ can be found. As the circle angle Ψ is assumed to be small ($\Psi < \ln 2$), it can be expressed as follows;

$$\psi = \frac{y}{2a\sin\theta} - \frac{1}{6}\left(\frac{y}{2a\sin\theta}\right)^3 \tag{B.10}$$

These equations are used for transforming, however at the leading edge Ψ becomes undetermined, since both y and θ are zero.

The velocity on the circle is $\frac{dw}{dz}$, psuedo circle $\frac{dw}{dz}\cdot\frac{dz}{dz'}$, and foil $\frac{dw}{dz}\cdot\frac{dz}{dz'}\cdot\frac{dz'}{d\zeta}$, the velocity on the foil can also be written as $\frac{dw}{dz}\cdot\frac{d\zeta}{dz}$.

$$\frac{d\zeta}{dz} = \frac{(y\cot\theta + x\psi'\tan\theta) + i\,(x\tan\theta - y\psi'\cot\theta)}{z\,(1+\epsilon')} \tag{B.11}$$

All primes are differentiated against theta. Now the absolute velocity at a point on the foil is described by v.

$$v = \left|\frac{dw}{dz}\right|\left|\frac{dz}{d\xi}\right| = \frac{V\left[\sin(\alpha+\theta+\epsilon)+\sin\left(\alpha+\epsilon_T\right)\right](1+\epsilon')\,e^{\psi*}}{\sqrt{\left(\sinh^2\psi+\sin^2\theta\right)\left[1+\left(\psi'\right)^2\right]}} \tag{B.12}$$

Lastly the local pressure coefficient can be found:

$$C_p = 1-\left(\frac{v}{V}\right)^2 \tag{B.13}$$

Following this procedure, a pressure distribution can be generated on any foil geometry which is translated from a circle.

C

Xfoil convergence study of XT parameter

The XT parameter dictates between which chord locations the panel spacing is decreased. The different locaitons for XT tried are: 0-0.05, 0.05-0.1, 0.1-0.15, 0.15-0.2, 0.2-0.25, 0-0.1, 0.1-0.2, 0-0.2 and 1-1. All values are given in x/c and XT 1-1, which means no location for bunching is given. This is visualised in figure C.1.

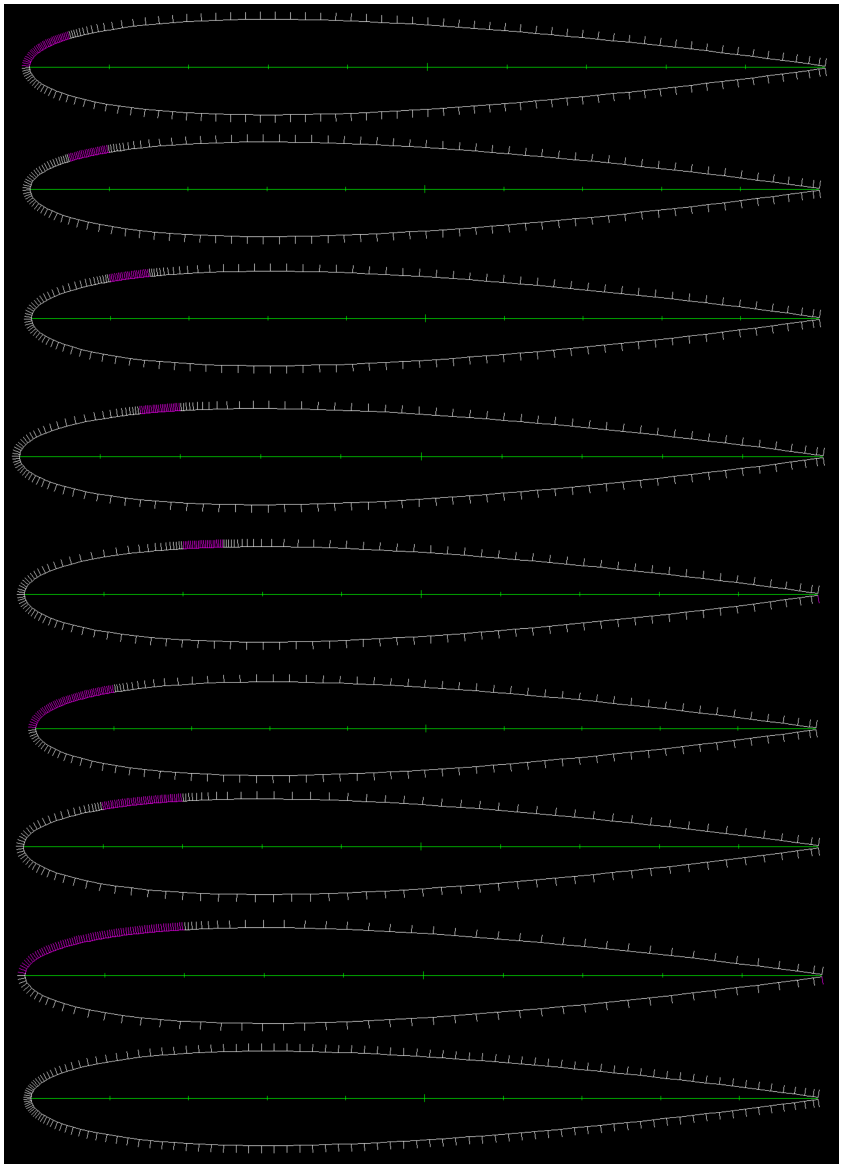

Figure C.1: Visualisation of increased panels for certain locations on a NACA0012. From top to bottom the location is XT = 0-0.05, 0.05-0.1, 0.1-0.15, 0.15-0.2, 0.2-0.25, 0-0.1, 0.1-0.2, 0-0.2 and 1-1.

The pressure distributions resulting from these different settings are plotted in figure C.2. All pressure distributions overlap, the influence of the parameter XT is negligible and therefor not used.

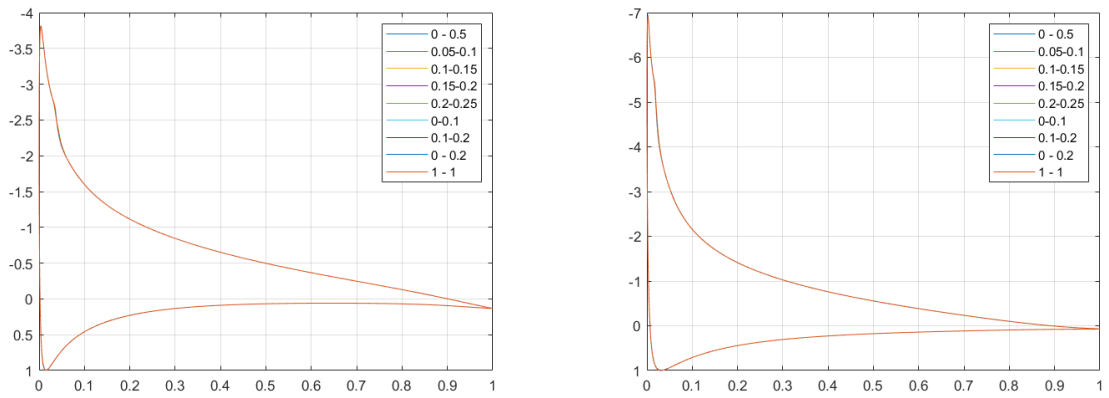

(a) AoA 8°

(b) AoA12°

Figure C.2: Pressure distributions from Xfoil to see the effect a prescribed location for increased panel density has on the result

D

Technical drawings

D.1. Foil

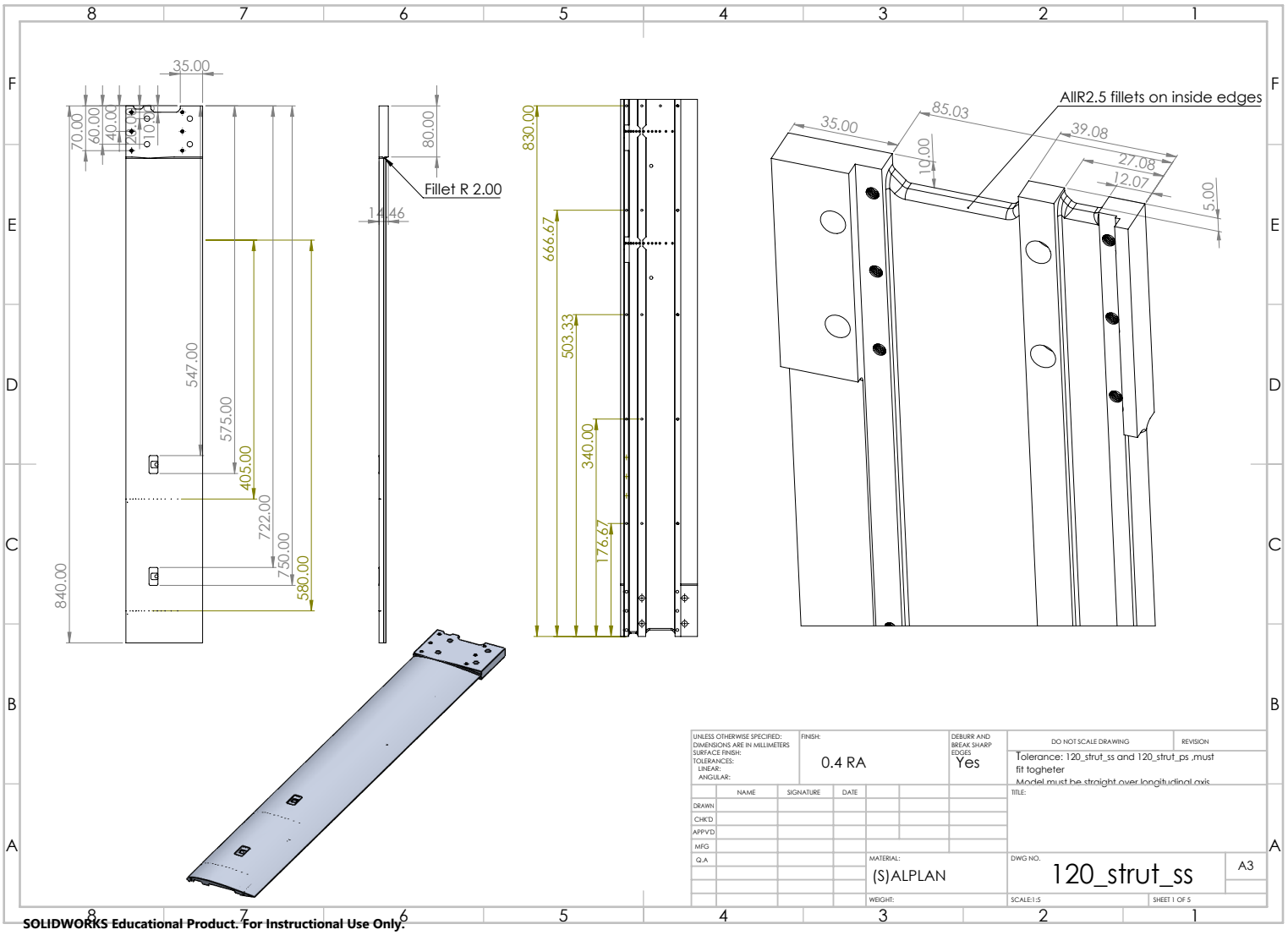

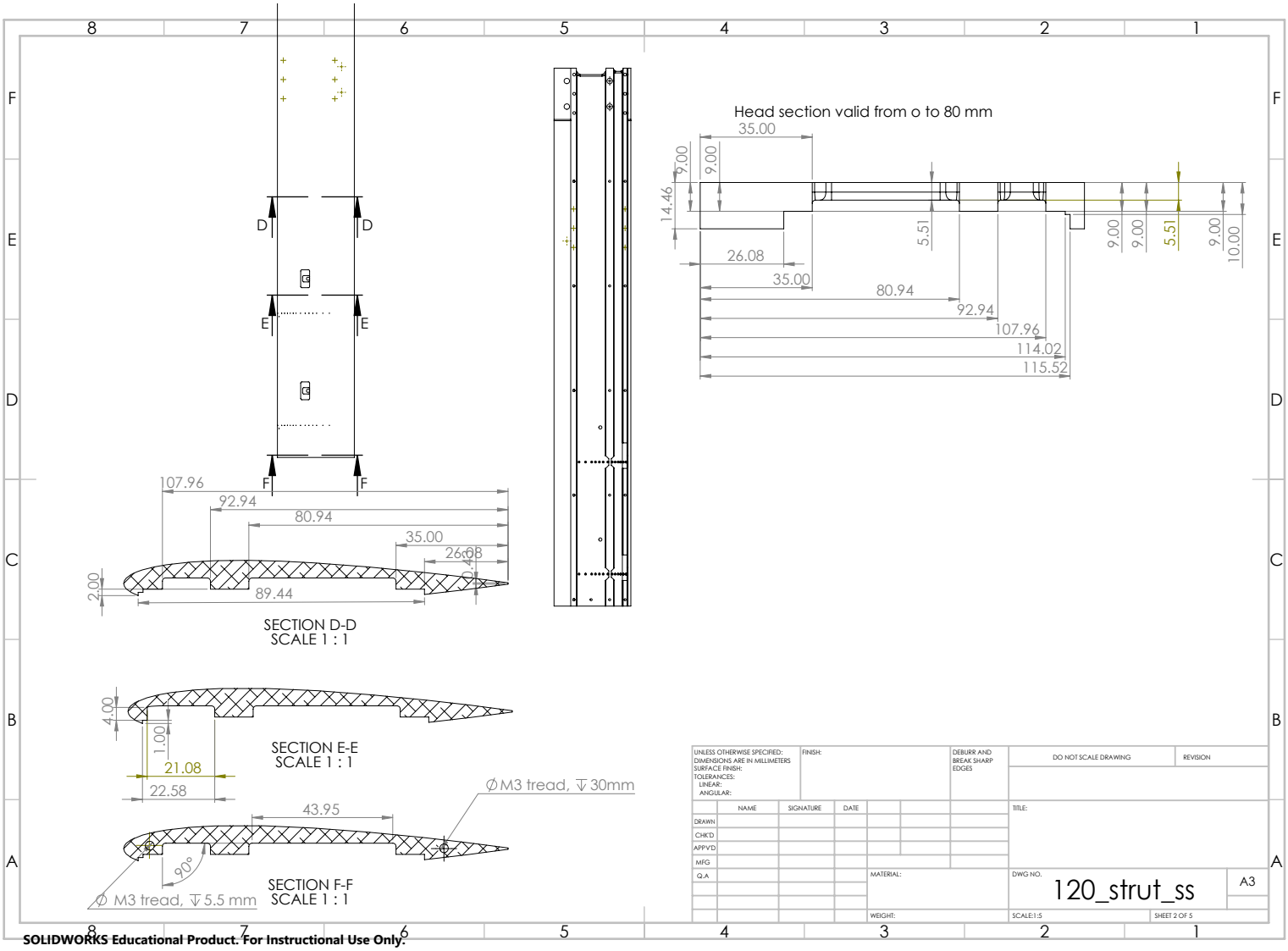

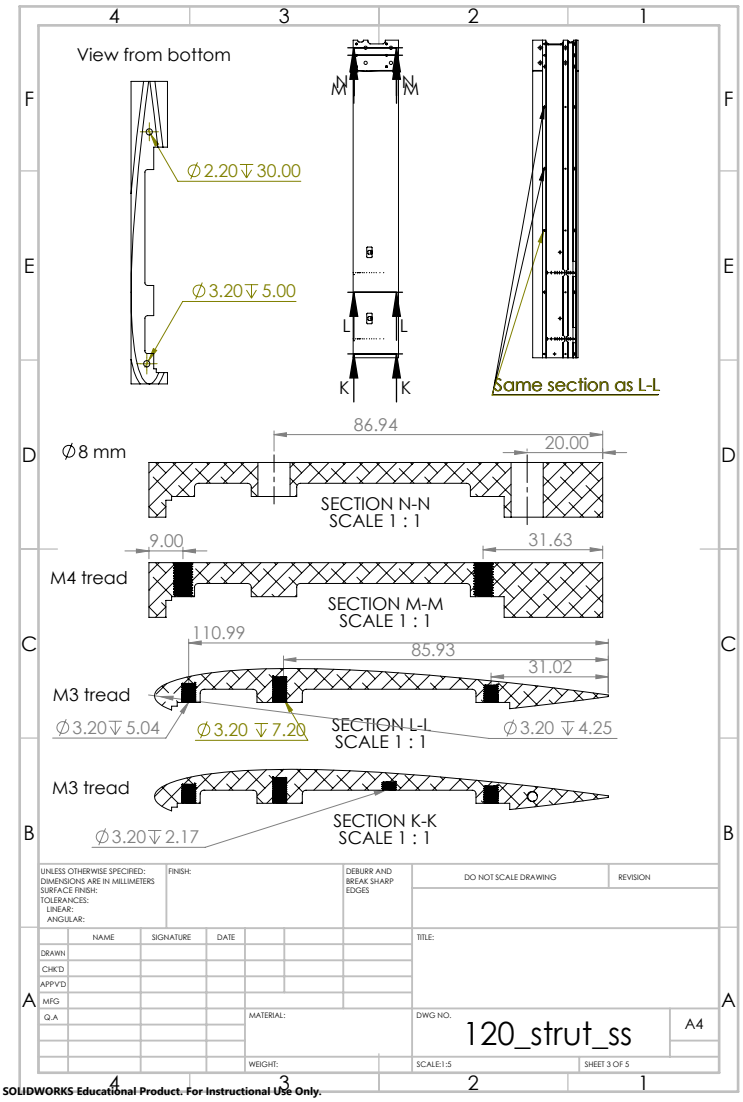

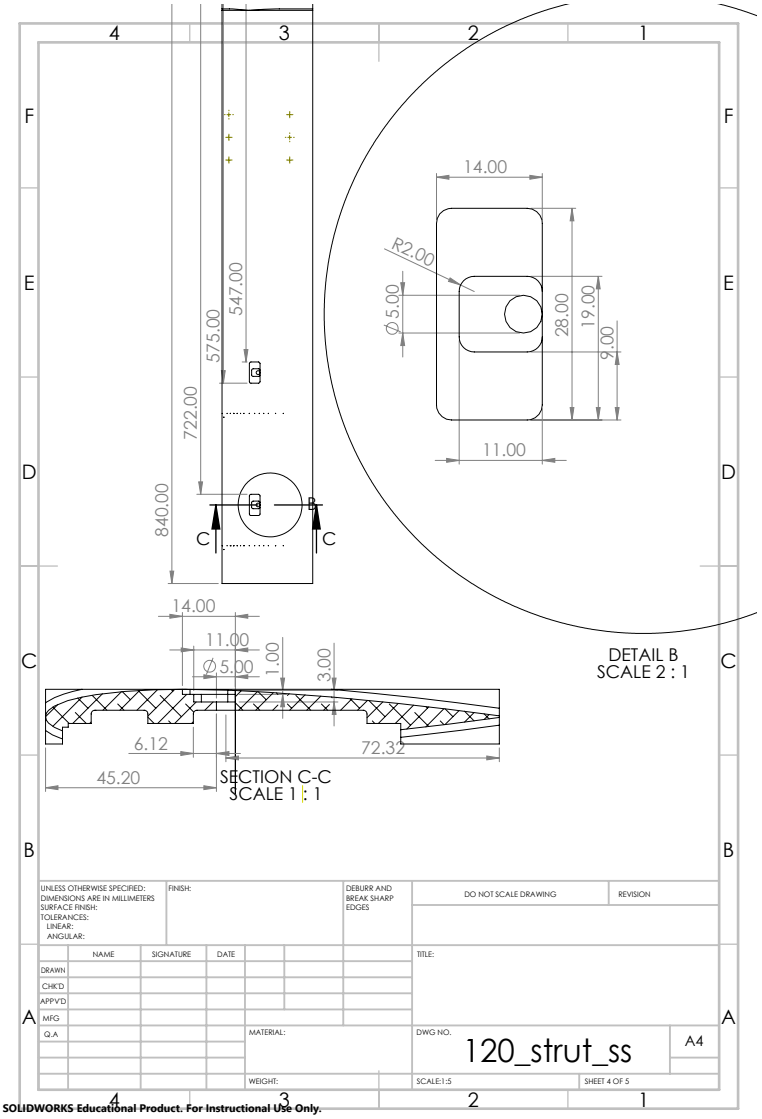

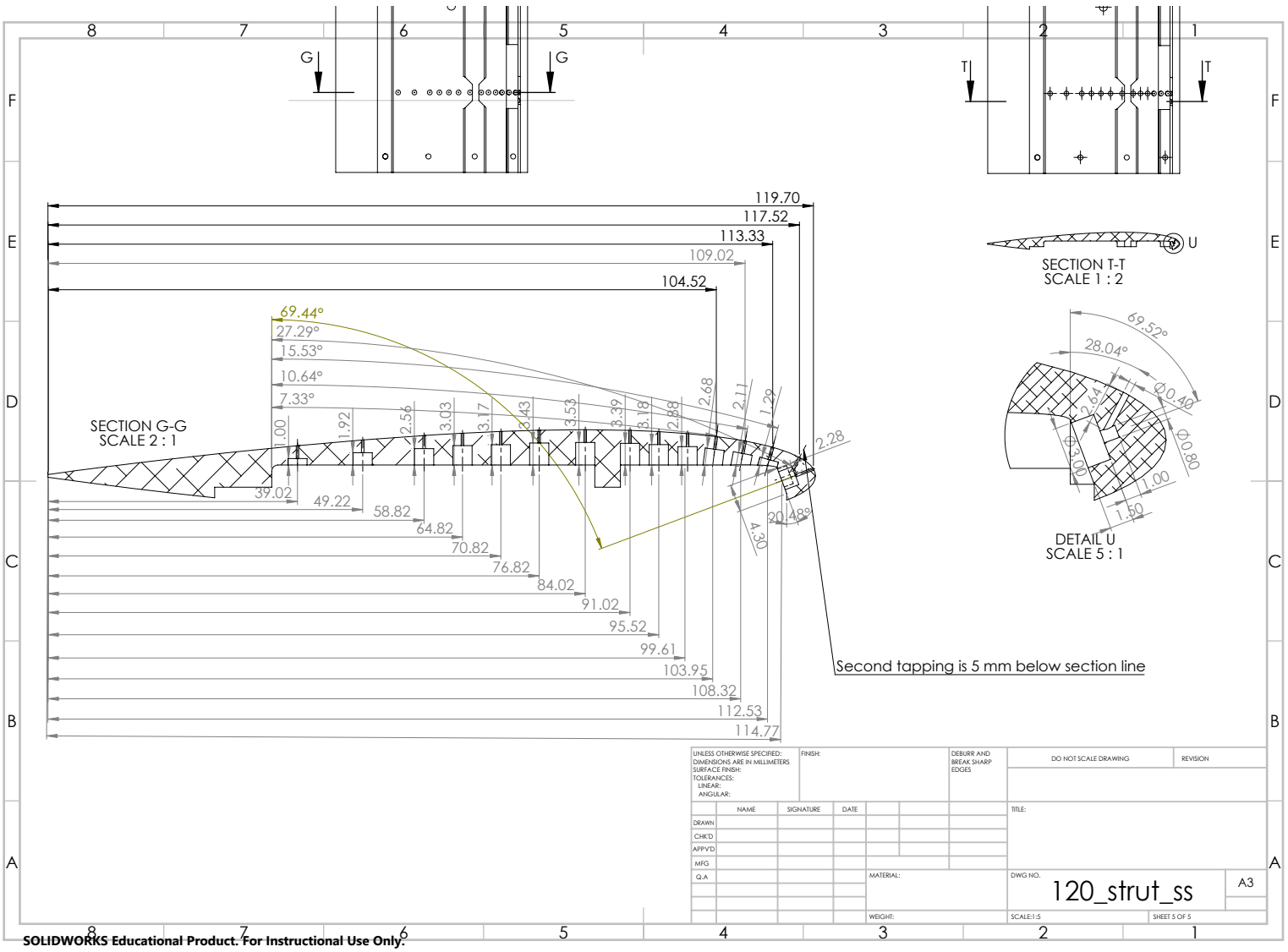

UNLESS OTHERWISE SPECIFIED: DIMENSIONS ARE IN MILLIMETERS SURFACE FINISH: TOLERANCES: LINEAR: ANGULAR:		FINISH:		DEBURR AND BREAK SHARP EDGES	DO NOT SCALE DRAWING	REVISION	
	NAME	SIGNATURE	DATE		TITLE:		
DRAWN							
CHKD							
APPV'D							
MFG							
Q.A				MATERIAL:	DWG NO. 120_strut_ss		A3
				WEIGHT:	SCALE:1:5	SHEET 5 OF 5	

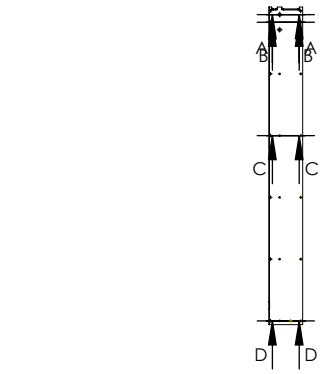

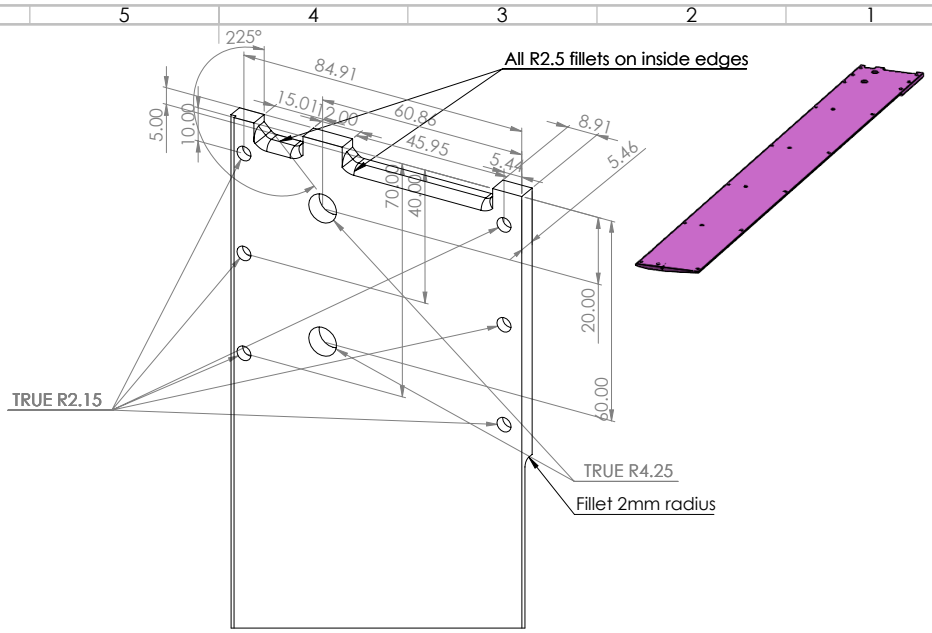

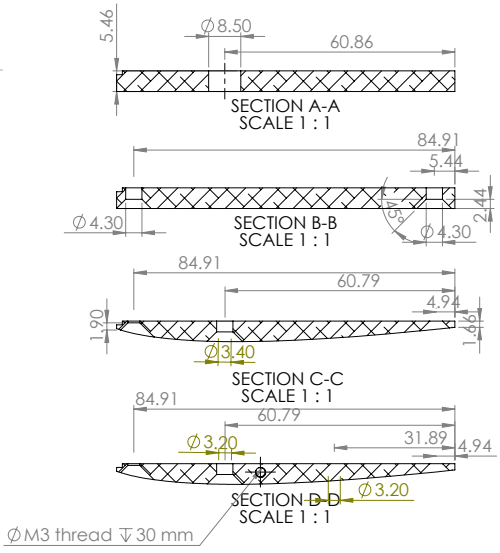

UNLESS OTHERWISE SPECIFIED: DIMENSIONS ARE IN MILLIMETERS SURFACE FINISH: TOLERANCES: LINEAR: ANGULAR:		FINISH: 0.4RA		DEBURR AND BREAK SHARP EDGES	DO NOT SCALE DRAWING		REVISION
					Both pieces (ss and ps) must fit togeheter Piece must be straight over longitudinal axis		
	NAME	SIGNATURE	DATE				
DRAWN					TITLE:		
CHKD							
APPV'D							
MFG							
Q.A							
				MATERIAL:	DWG NO.		A3
					120_strut_ps		
				WEIGHT:	SCALE:1:10	SHEET 1 OF 1	

D.2. Extension pieces

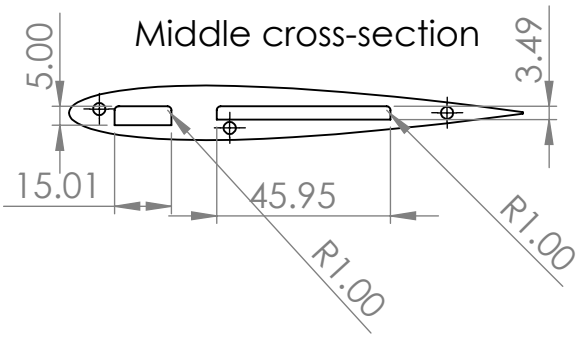

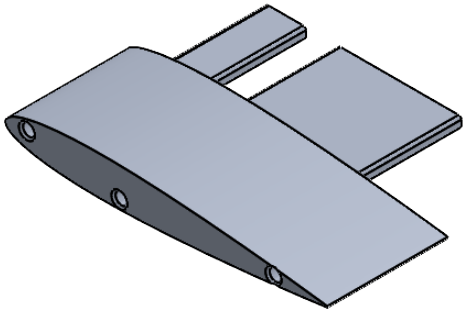

Closed piece 40 mm

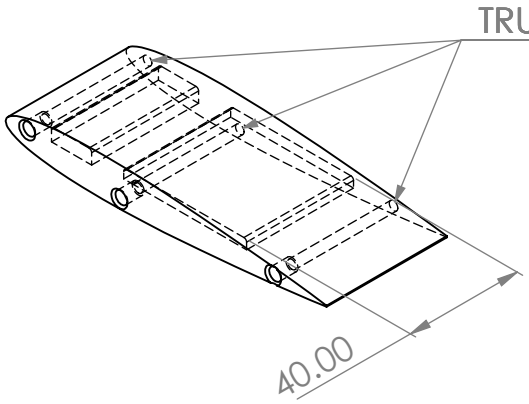

Closed piece 80 mm

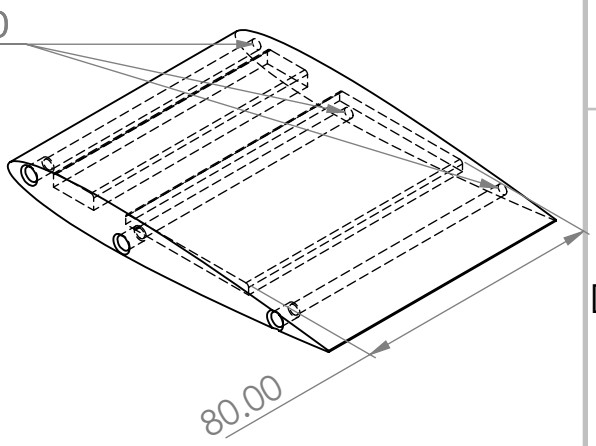

Closed piece 120 mm

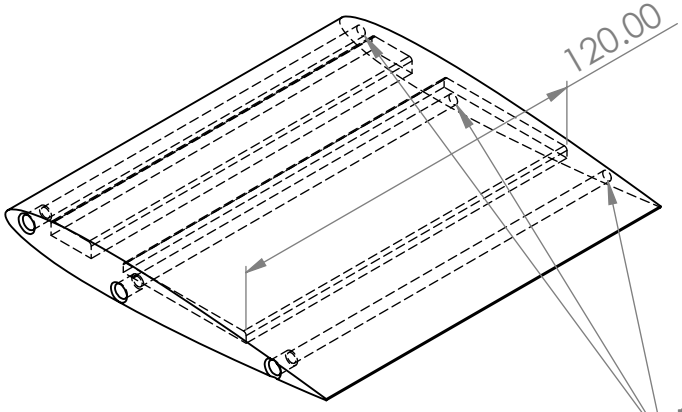

Open piece 40 mm

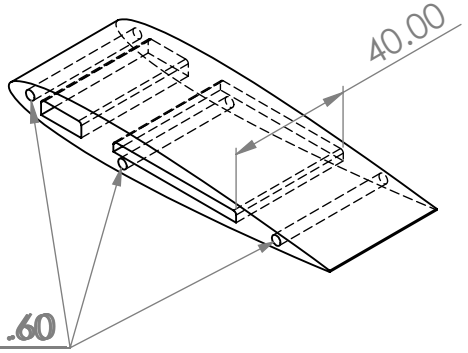

UNLESS OTHERWISE SPECIFIED: DIMENSIONS ARE IN MILLIMETERS SURFACE FINISH: 0.2RA TOLERANCES: LINEAR: inside +/-0.25 mm Outside, flush to aluminium strut ANGULAR:	FINISH:		DEBURR AND BREAK SHARP EDGES	DO NOT SCALE DRAWING	REVISION	
	NAME	SIGNATURE	DATE	TITLE:		
DRAWN				Extension pieces different lengths		
CHK'D						
APPV'D						
MFG						
Q.A				MATERIAL:	DWG NO.	A4
				SLA resin rigid 10K (formlabs)		
				WEIGHT:	SCALE:1:2	SHEET 1 OF 1

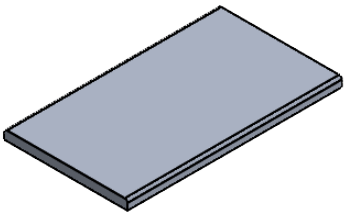

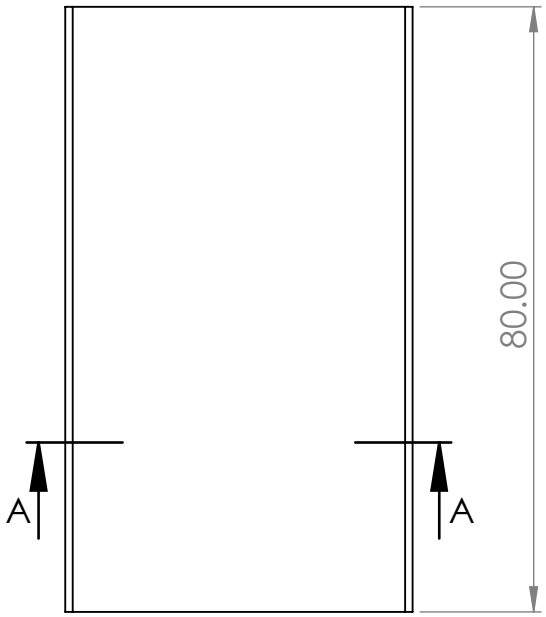

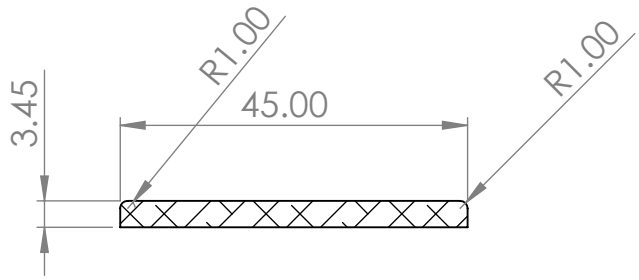

SECTION A-A
SCALE 1 : 1

4 pieces needed of same cross - section but different lengths.

1. 80mm
2. 120 mm
3. 160 mm
4. 200 mm

UNLESS OTHERWISE SPECIFIED: DIMENSIONS ARE IN MILLIMETERS SURFACE FINISH: - TOLERANCES: LINEAR: +/- 0.25 mm ANGULAR: -	FINISH:	DEBURR AND BREAK SHARP EDGES	DO NOT SCALE DRAWING / REVISION

	NAME	SIGNATURE	DATE
DRAWN			
CHK'D			
APPV'D			
MFG			
Q.A			

TITLE:
Wide stainless steel bars, for the extension pieces

MATERIAL:
Stainless Steel

DWG NO.

A4

WEIGHT:

SCALE:1:2

SHEET 1 OF 1

4 pieces, same concept different lengths.
All four different sizes depicted below.

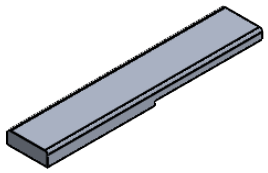

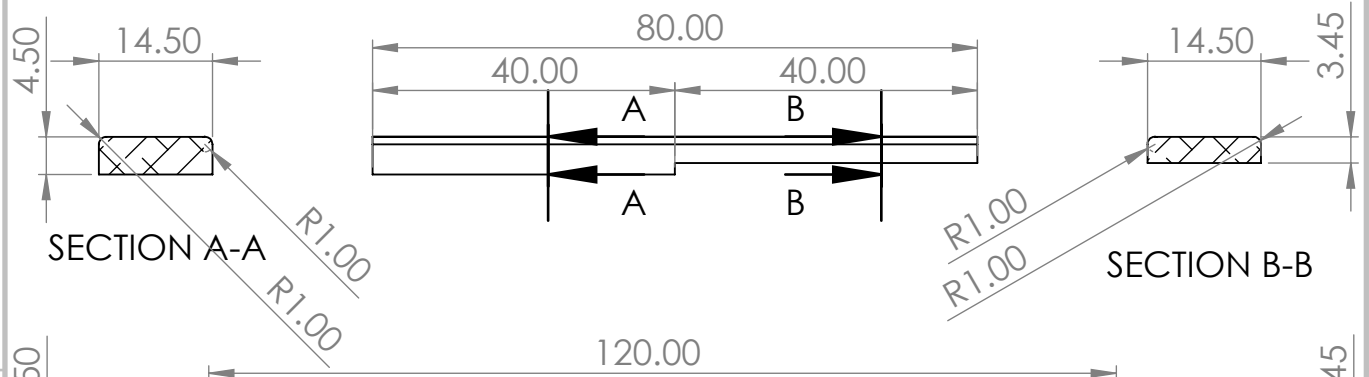

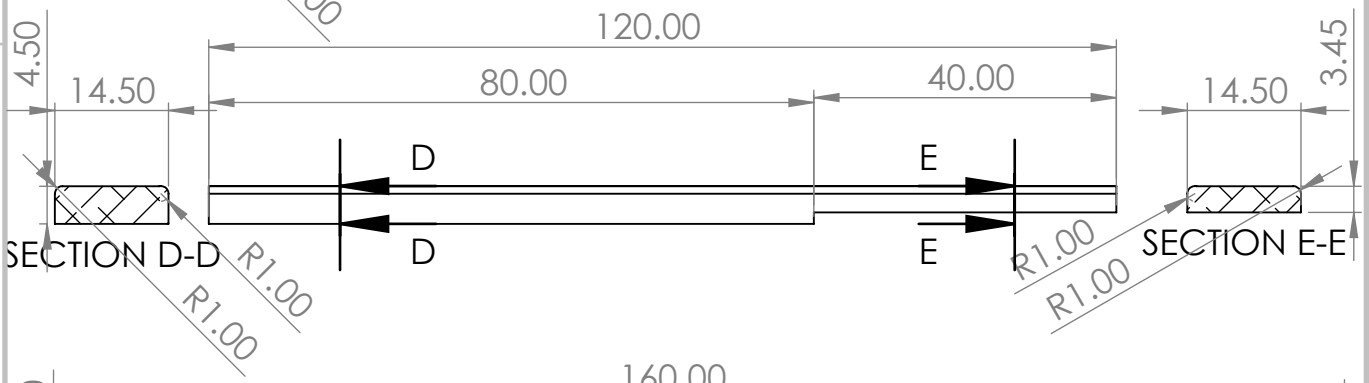

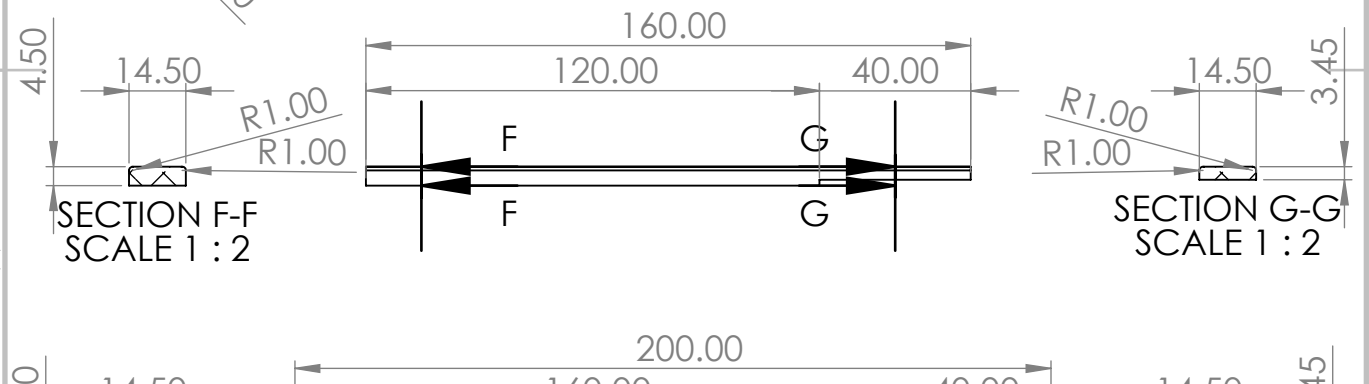

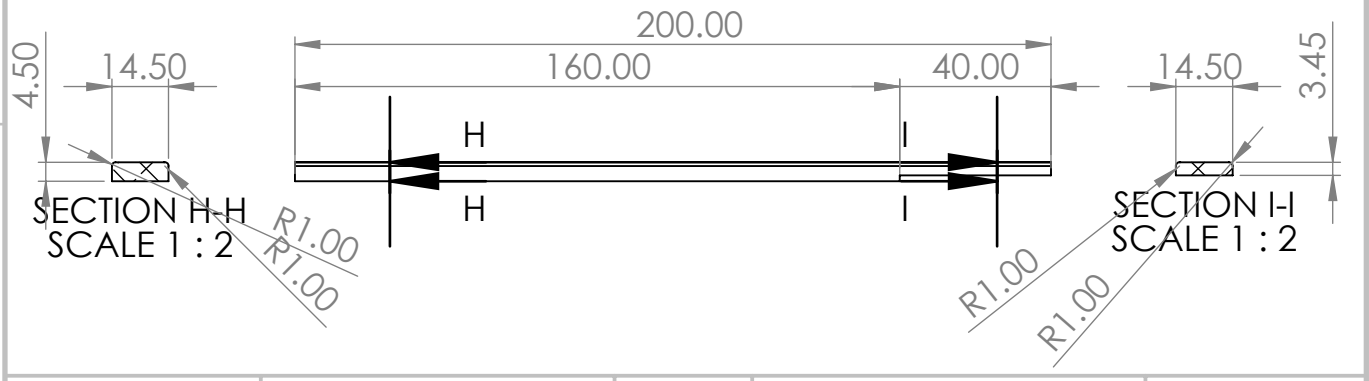

UNLESS OTHERWISE SPECIFIED: DIMENSIONS ARE IN MILLIMETERS SURFACE FINISH: - TOLERANCES: LINEAR: +/- 0.25mm ANGULAR: -	FINISH:	DEBURR AND BREAK SHARP EDGES	DO NOT SCALE DRAWING / REVISION

	NAME	SIGNATURE	DATE
DRAWN			
CHK'D			
APPV'D			
MFG			
Q.A			

TITLE:

Narrow stainless steel bars, to fit the leading edge holw of the extension pieces

MATERIAL: Stainless steel	DWG NO.	A4
WEIGHT:	SCALE:1:1	SHEET 1 OF 1

D.3. Straight attachment bracket

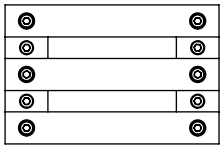

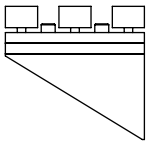

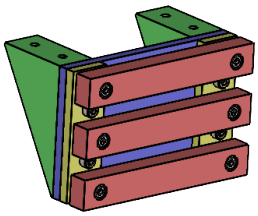

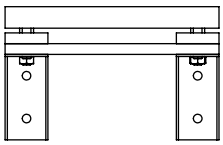

ITEM NO.	PART NUMBER	DESCRIPTION	QTY.
1	bar_30x20x200		3
2	bracket_80x130x40		2
3	plate_10x200x130		1
4	strip_40x80x10		2
5	B18.3.1M - 8 x 1.25 x 30 Hex SHCS -- 30NHX		4
6	B18.3.1M - 8 x 1.25 x 40 Hex SHCS -- 40NHX		6
7	B18.2.4.1M - Hex nut, Style 1, M8 x 1.25 --D-N		4

UNLESS OTHERWISE SPECIFIED:
DIMENSIONS ARE IN MILLIMETERS
SURFACE FINISH: -
TOLERANCES:
LINEAR: +/- 1mm
ANGULAR:

FINISH:

DEBURR AND BREAK SHARP EDGES

DO NOT SCALE DRAWING | REVISION

	NAME	SIGNATURE	DATE
DRAWN			
CHK'D			
APPV'D			
MFG			
Q.A			

TITLE:

MATERIAL: Aluminium

DWG NO. Attachment_assembly_22042

A4

WEIGHT:

SCALE:1:5

SHEET 1 OF 1

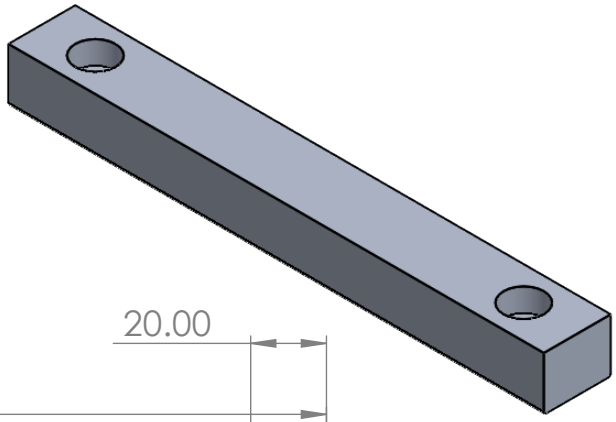

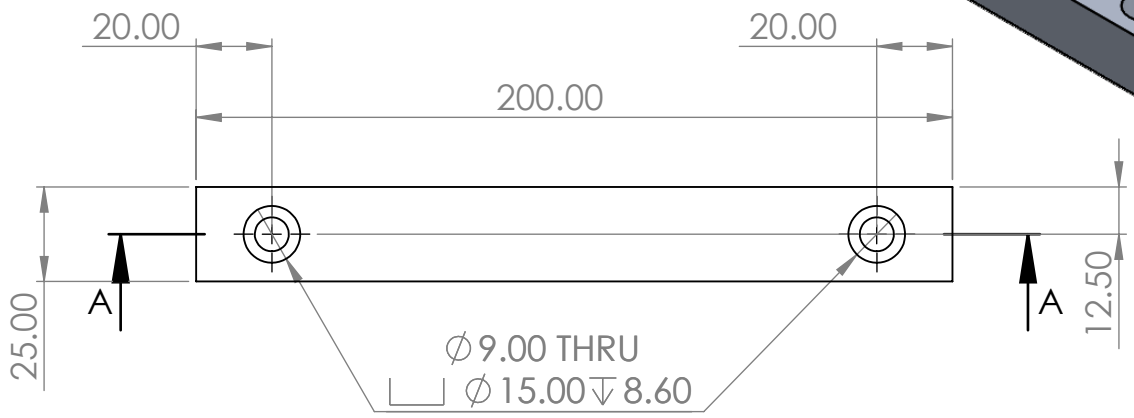

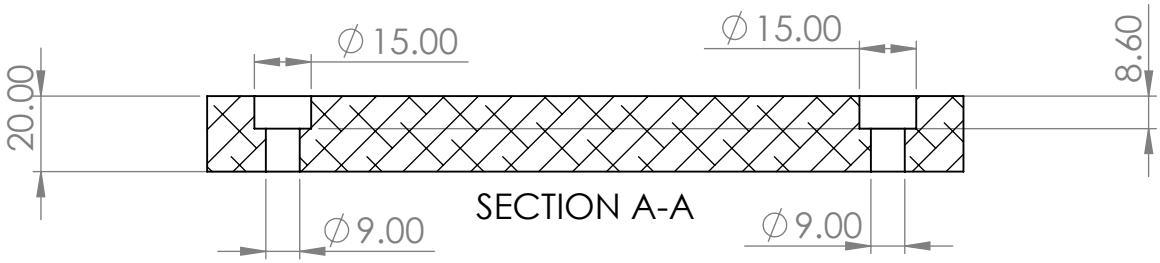

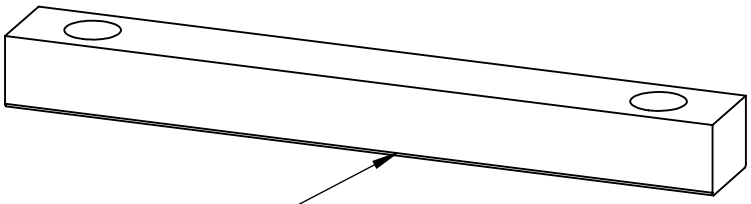

Fillet the edges to prevent tubes from scratching

UNLESS OTHERWISE SPECIFIED: DIMENSIONS ARE IN MILLIMETERS SURFACE FINISH: TOLERANCES: LINEAR: ANGULAR:		FINISH:		DEBURR AND BREAK SHARP EDGES		DO NOT SCALE DRAWING	REVISION
	NAME	SIGNATURE	DATE			TITLE:	
DRAWN						Ammount: 3	
CHK'D							
APPV'D							
MFG							
Q.A				MATERIAL:		DWG NO. bar_200x25x20_2	A4
				WEIGHT:		SCALE:1:2	SHEET 1 OF 1

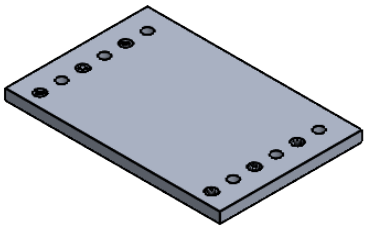

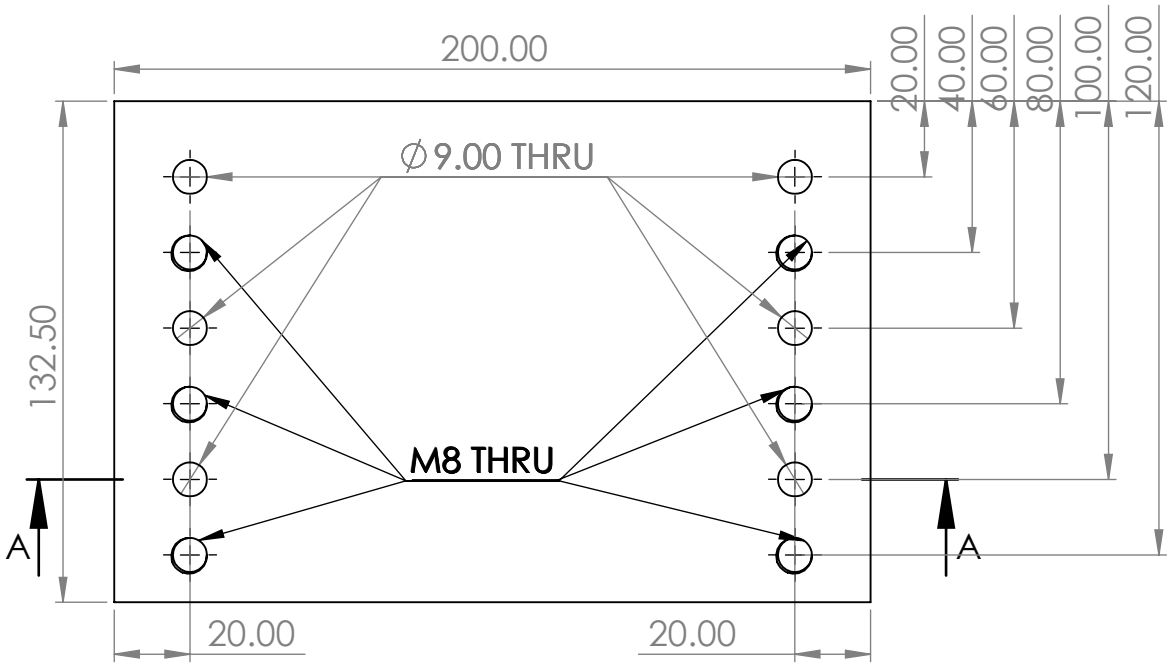

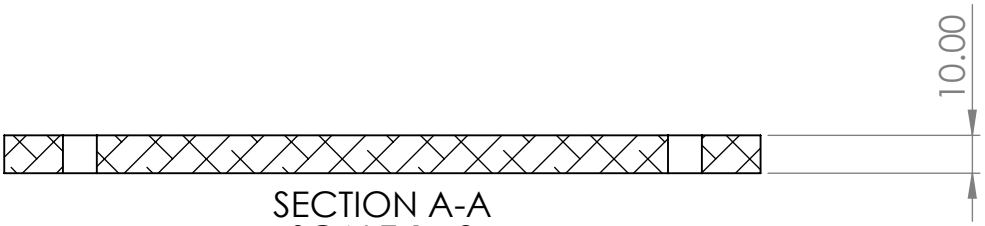

SECTION A-A
SCALE 1 : 2

UNLESS OTHERWISE SPECIFIED: DIMENSIONS ARE IN MILLIMETERS SURFACE FINISH: TOLERANCES: LINEAR: ANGULAR:		FINISH:		DEBURR AND BREAK SHARP EDGES		DO NOT SCALE DRAWING	REVISION
	NAME	SIGNATURE	DATE			TITLE:	
DRAWN							
CHK'D							
APPV'D							
MFG							
Q.A				MATERIAL:		DWG NO.	A4
						plate_200x132.5x10	
				WEIGHT:		SCALE:1:5	SHEET 1 OF 1

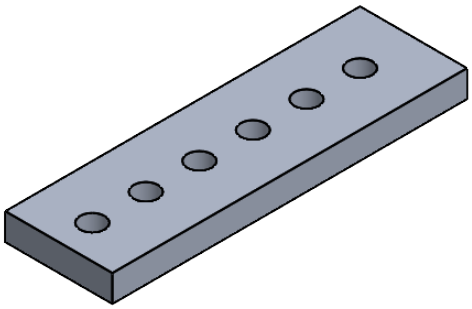

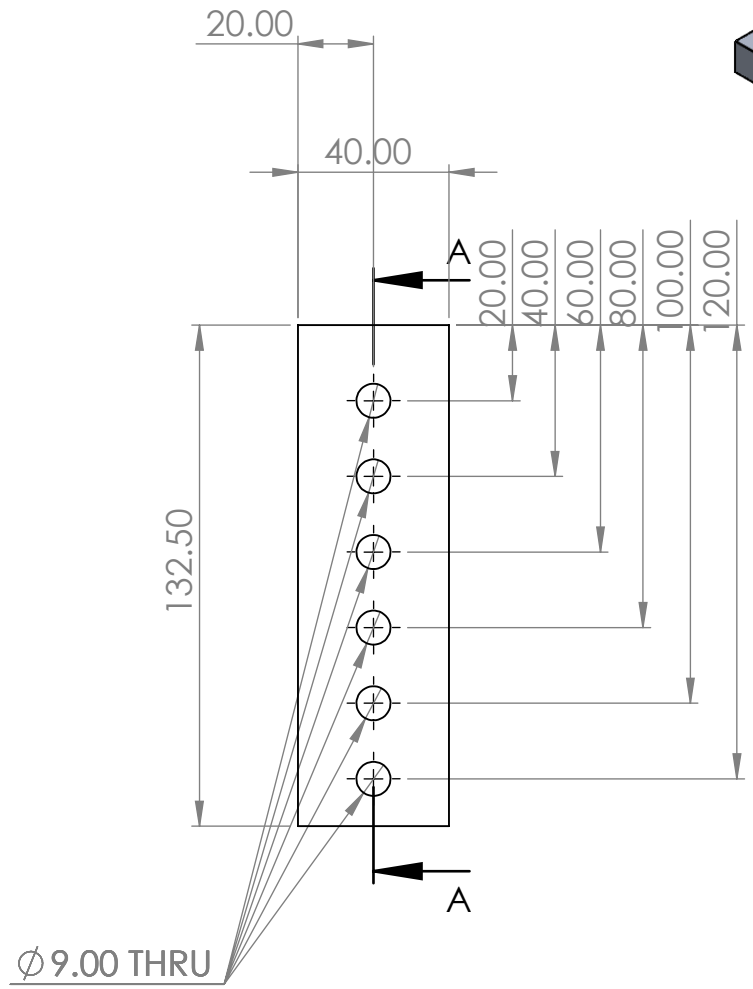

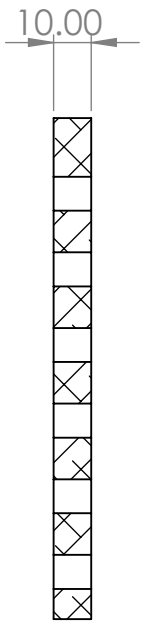

SECTION A-A

UNLESS OTHERWISE SPECIFIED: DIMENSIONS ARE IN MILLIMETERS SURFACE FINISH: TOLERANCES: LINEAR: ANGULAR:		FINISH:		DEBURR AND BREAK SHARP EDGES		DO NOT SCALE DRAWING	REVISION
	NAME	SIGNATURE	DATE			TITLE:	
DRAWN						Ammount: 2	
CHK'D							
APPV'D							
MFG							
Q.A				MATERIAL:		DWG NO. strip_40x80x10	A4
				WEIGHT:		SCALE:1:2	SHEET 1 OF 1

D.4. Angled spacer

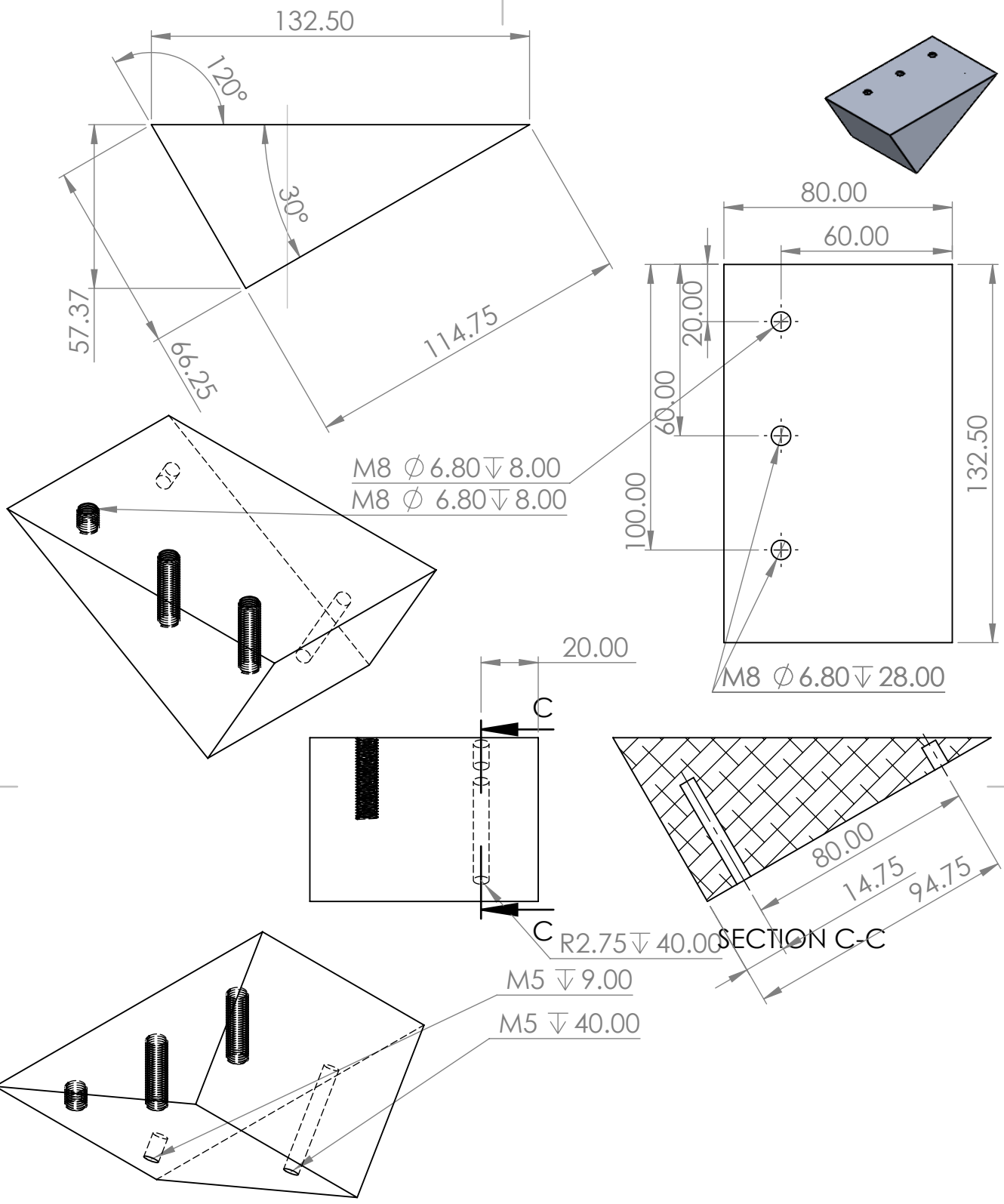

UNLESS OTHERWISE SPECIFIED: DIMENSIONS ARE IN MILLIMETERS SURFACE FINISH: - TOLERANCES: LINEAR: +/- 0.5 mm ANGULAR: 0.1 deg	FINISH:	DEBURR AND BREAK SHARP EDGES	DO NOT SCALE DRAWING / REVISION

	NAME	SIGNATURE	DATE
DRAWN			
CHK'D			
APPV'D			
MFG			
Q.A			

TITLE:

MATERIAL: Aluminium

DWG NO. angled_bracket_1

A4

WEIGHT:

SCALE:1:2

SHEET 1 OF 1

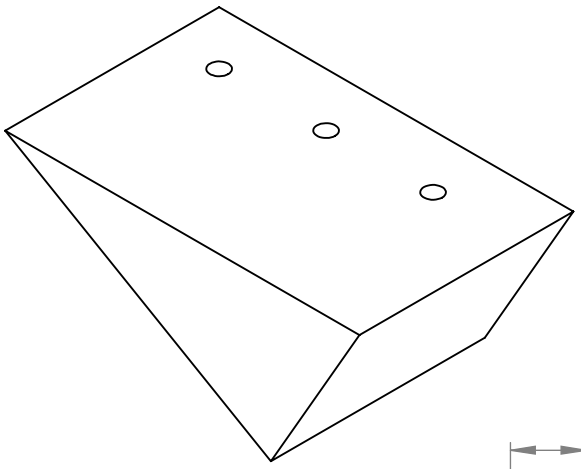

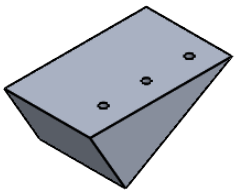

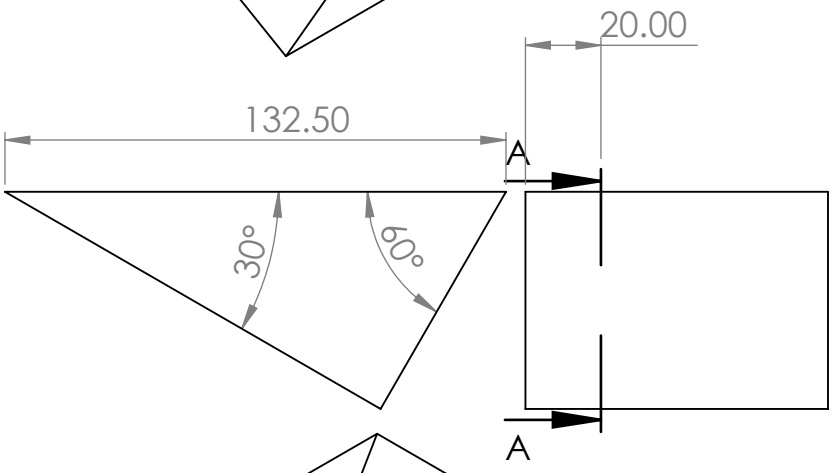

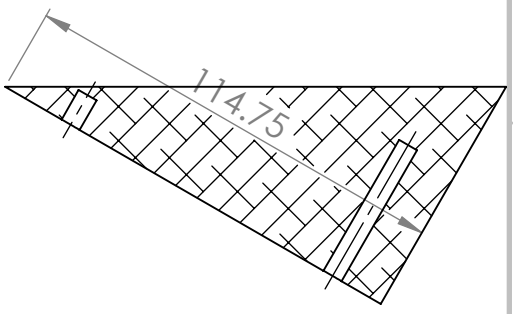

SECTION A-A

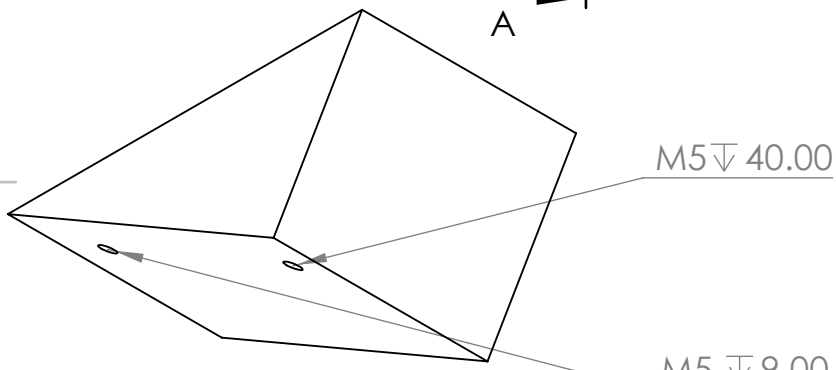

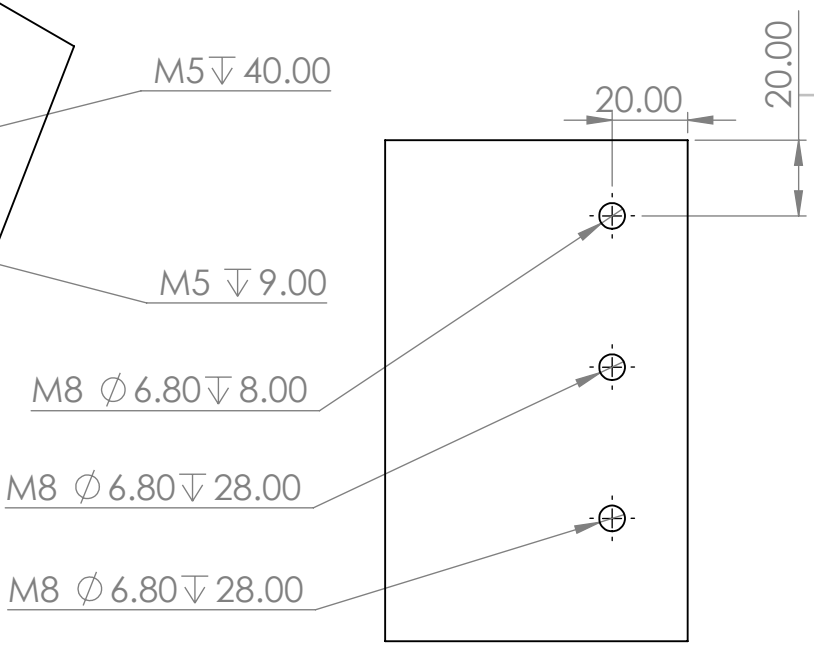

UNLESS OTHERWISE SPECIFIED: DIMENSIONS ARE IN MILLIMETERS SURFACE FINISH: - TOLERANCES: LINEAR: +/- 0.5mm ANGULAR: 0.1 deg	FINISH:	DEBURR AND BREAK SHARP EDGES	DO NOT SCALE DRAWING / REVISION

	NAME	SIGNATURE	DATE
DRAWN			
CHK'D			
APPV'D			
MFG			
Q.A			

TITLE:

Bracket 2 is mirrored version of brackete 1

MATERIAL:	DWG NO.	
Aluminium	angled_bracket_2	A4
WEIGHT:	SCALE:1:2	SHEET 1 OF 1

E

Force transducer calibration results

Run				Run	1	F pos			Run	2	F neg		
				[kg]	[V]	[N]	[N/V]		[kg]	[V]	[N]	[N/V]	
date	1-Jun-22		step	massa	U	F	sens	accuracy	massa	U	F	sens	accuracy
			1	0.00	0.00	0.00			0.00	0.00	0.00		
chan	5		2	1.00	0.13	9.81	73.38	0.1%	-1.00	-0.13	-9.81	73.20	-0.2%
name	FSZ		3	3.00	0.40	29.44	73.33	0.0%	-3.00	-0.40	-29.44	73.24	-0.1%
			4	5.00	0.67	49.06	73.43	0.1%	-5.00	-0.67	-49.06	73.27	-0.1%
			5	10.00	1.34	98.12	73.31	0.0%	-10.00	-1.34	-98.12	73.24	-0.1%
sensor no	861-40-I		6	15.00	2.01	147.18	73.30	0.0%	-15.00	-2.01	-147.18	73.28	-0.1%
range	40	kg	7	20.00	2.68	196.24	73.31	0.0%	-20.00	-2.68	-196.24	73.27	-0.1%
			8	25.00	3.35	245.30	73.32	0.0%	-25.00	-3.35	-245.30	73.32	0.0%
amplifier	Picas		9	30.00	4.01	294.36	73.40	0.1%	-30.00	-4.02	-294.36	73.31	0.0%
range in	2	mV/V	10	35.00	4.68	343.42	73.42	0.1%	-35.00	-4.69	-343.42	73.32	0.0%
range out	10	V	11	40.00	5.35	392.48	73.38	0.1%	-40.00	-5.36	-392.48	73.34	0.0%
R neutral	-1.0971	uV/V	12	35.00	4.68	343.42	73.31	0.0%	-35.00	-4.69	-343.42	73.26	-0.1%
C neutral	-14.505	uV/V	13	30.00	4.01	294.36	73.36	0.0%	-30.00	-4.02	-294.36	73.28	-0.1%
			14	25.00	3.34	245.30	73.35	0.0%	-25.00	-3.35	-245.30	73.30	0.0%
			15	20.00	2.67	196.24	73.36	0.0%	-20.00	-2.68	-196.24	73.28	-0.1%
			16	15.00	2.01	147.18	73.39	0.1%	-15.00	-2.01	-147.18	73.27	-0.1%
			17	10.00	1.34	98.12	73.33	0.0%	-10.00	-1.34	-98.12	73.28	-0.1%
			18	5.00	0.67	49.06	73.38	0.1%	-5.00	-0.67	-49.06	73.28	-0.1%
			19	3.00	0.40	29.44	73.39	0.1%	-3.00	-0.40	-29.44	73.30	0.0%
sens	73.322	N/V	20	1.00	0.13	9.81	73.44	0.2%	-1.00	-0.13	-9.81	73.31	0.0%
	0.133765		21	0.00	0.00	0.00			0.00	0.00	0.00		

Run				Run	3	F pos			Run	4	F neg		
				[kg]	[V]	[N]	[N/V]		[kg]	[V]	[N]	[N/V]	
date	1-Jun-22		step	massa	U	F	sens	accuracy	massa	U	F	sens	accuracy
			1	0.00	0.00	0.00			0.00	0.00	0.00		
chan	6		2	1.00	0.27	9.81	36.69	-0.2%	-1.00	-0.27	-9.81	36.82	0.1%
name	F6Z		3	2.00	0.53	19.62	36.72	-0.2%	-2.00	-0.53	-19.62	36.73	-0.1%
			4	4.00	1.07	39.25	36.75	-0.1%	-4.00	-1.07	-39.25	36.83	0.1%
			5	6.00	1.60	58.87	36.75	-0.1%	-6.00	-1.60	-58.87	36.80	0.1%
sensor no	861-20-II		6	8.00	2.14	78.50	36.82	0.1%	-8.00	-2.13	-78.50	36.79	0.0%
range	20	kg	7	10.00	2.67	98.12	36.77	0.0%	-10.00	-2.67	-98.12	36.81	0.1%
			8	15.00	4.00	147.18	36.76	0.0%	-15.00	-4.00	-147.18	36.80	0.1%
amplifier	Picas		9	20.00	5.34	196.24	36.77	0.0%	-20.00	-5.33	-196.24	36.80	0.1%
range in	2	mV/V	10	15.00	4.00	147.18	36.78	0.0%	-15.00	-4.00	-147.18	36.76	0.0%
range out	10	V	11	10.00	2.67	98.12	36.75	-0.1%	-10.00	-2.66	-98.12	36.78	0.0%
R neutral	-226.4	uV/V	12	8.00	2.14	78.50	36.79	0.0%	-8.00	-2.13	-78.50	36.76	0.0%
C neutral	-142.15	uV/V	13	6.00	1.60	58.87	36.75	-0.1%	-6.00	-1.60	-58.87	36.77	0.0%
			14	4.00	1.07	39.25	36.76	0.0%	-4.00	-1.06	-39.25	36.77	0.0%
			15	2.00	0.53	19.62	36.73	-0.1%	-2.00	-0.53	-19.62	36.77	0.0%
			16	1.00	0.27	9.81	36.81	0.1%	-1.00	-0.26	-9.81	36.86	0.2%
			17	0.00	0.00	0.00	36.77	0.0%	0.00	0.00	0.00	36.81	0.1%
					510								
sens	36.775	N/V											
	0.266896												

Run				Run	5	F pos			Run	6	F neg		
				[kg]	[V]	[N]	[N/V]		[kg]	[V]	[N]	[N/V]	
date	2-Jun-22		step	massa	U	F	sens	accuracy	massa	U	F	sens	accuracy
			1	0.00	0.00	0.00			0.00	0.00	0.00		
chan	3		2	1.00	-0.13	9.81	-76.50	-0.1%	-1.00	0.13	-9.81	-76.69	0.1%
name	F3Y		3	3.00	-0.38	29.44	-76.47	-0.2%	-3.00	0.38	-29.44	-76.63	0.0%
			4	5.00	-0.64	49.06	-76.56	-0.1%	-5.00	0.64	-49.06	-76.59	0.0%
			5	10.00	-1.28	98.12	-76.52	-0.1%	-10.00	1.28	-98.12	-76.56	-0.1%
sensor no	047-40-II		6	15.00	-1.92	147.18	-76.65	0.1%	-15.00	1.92	-147.18	-76.63	0.0%
range	40	kg	7	20.00	-2.56	196.24	-76.62	0.0%	-20.00	2.56	-196.24	-76.64	0.0%
			8	25.00	-3.20	245.30	-76.59	0.0%	-25.00	3.20	-245.30	-76.63	0.0%
amplifier	Picas		9	30.00	-3.84	294.36	-76.60	0.0%	-30.00	3.84	-294.36	-76.74	0.2%
range in	2	mV/V	10	35.00	-4.48	343.42	-76.68	0.1%	-35.00	4.48	-343.42	-76.68	0.1%
range out	10	V	11	40.00	-5.12	392.48	-76.63	0.0%	-40.00	5.12	-392.48	-76.72	0.2%
R neutral	267.73	uV/V	12	35.00	-4.48	343.42	-76.57	0.0%	-35.00	4.48	-343.42	-76.59	0.0%
C neutral	11.674	uV/V	13	30.00	-3.84	294.36	-76.46	-0.2%	-30.00	3.84	-294.36	-76.55	-0.1%
			14	25.00	-3.20	245.30	-76.57	0.0%	-25.00	3.20	-245.30	-76.59	0.0%
			15	20.00	-2.56	196.24	-76.62	0.0%	-20.00	2.56	-196.24	-76.61	0.0%
			16	15.00	-1.92	147.18	-76.65	0.1%	-15.00	1.92	-147.18	-76.65	0.1%
			17	10.00	-1.28	98.12	-76.57	0.0%					
			18	5.00	-0.64	49.06	-76.57	0.0%	-10.00	1.28	-98.12	-76.72	0.2%
			19	3.00	-0.38	29.44	-76.35	-0.3%	-5.00	0.64	-49.06	-76.56	-0.1%
sens	-76.606	N/V	20	1.00	-0.13	9.81	-76.53	-0.1%	-3.00	0.38	-29.44	-76.70	0.1%
	-0.12808		21	0.00	0.00	0.00			-1.00	0.13	-9.81		
	-0.122132												

Figure E.1: Data book of force transducer calibration, the accuracy of each measurement is with respect to the computed calibration factor denoted in orange on the left side for each sensor.

Run				Run	8	F pos			Run	7	F neg		
				[kg]	[V]	[N]	[N/V]		[kg]	[V]	[N]	[N/V]	
date	2-Jun-22		step	massa	U	F	sens	accuracy	massa	U	F	sens	accuracy
			1	0.00	0.00	0.00			0.00	0.00	0.00		
chan	1		2	1.00	0.28	9.81	35.47	0.2%	-1.00	-0.28	-9.81	35.35	-0.2%
name	F1X		3	2.00	0.55	19.62	35.41	0.0%	-2.00	-0.55	-19.62	35.44	0.1%
			4	4.00	1.11	39.25	35.41	0.0%	-4.00	-1.11	-39.25	35.40	0.0%
			5	6.00	1.66	58.87	35.42	0.0%	-6.00	-1.66	-58.87	35.40	0.0%
sensor no	20-XII		6	8.00	2.22	78.50	35.41	0.0%	-8.00	-2.22	-78.50	35.42	0.0%
range	20	kg	7	10.00	2.77	98.12	35.42	0.0%	-10.00	-2.77	-98.12	35.43	0.0%
			8	15.00	4.16	147.18	35.41	0.0%	-15.00	-4.16	-147.18	35.40	-0.1%
amplifier	Picas		9	20.00	5.54	196.24	35.41	0.0%	-20.00	-5.54	-196.24	35.43	0.0%
range in	2	mV/V	10	15.00	4.15	147.18	35.34	-0.2%	-15.00	-4.15	-147.18	35.36	-0.2%
range out	10	V	11	10.00	2.77	98.12	35.37	-0.1%	-10.00	-2.77	-98.12	35.40	0.0%
R neutral	794.62	uV/V	12	8.00	2.21	78.50	35.42	0.0%	-8.00	-2.21	-78.50	35.44	0.1%
C neutral	68.003	uV/V	13	6.00	1.66	58.87	35.44	0.1%	-6.00	-1.66	-58.87	35.44	0.1%
			14	4.00	1.10	39.25	35.42	0.0%	-4.00	-1.11	-39.25	35.41	0.0%
			15	2.00	0.55	19.62	35.44	0.1%	-2.00	-0.55	-19.62	35.43	0.0%
			16	1.00	0.27	9.81	35.46	0.1%	-1.00	-0.28	-9.81	35.47	0.1%
sens	35.416	N/V	17						0.00	0.00	0.00	35.46	0.1%
	0.277089				510								
	-0.111179												

Run				Run	10	F pos			Run	9	F neg		
				[kg]	[V]	[N]	[N/V]		[kg]	[V]	[N]	[N/V]	
date	2-Jun-22		step	massa	U	F	sens	accuracy	massa	U	F	sens	accuracy
			1	0.00	0.00	0.00			0.00	0.00	0.00		
chan	4		2	1.00	0.27	9.81	35.93	0.8%	-1.00	-0.27	-9.81	35.89	0.1%
name	F4Z		3	2.00	0.82	19.62	17.95	0.5%	-2.00	-0.55	-19.62	35.90	-0.1%
			4	4.00	1.37	39.25	35.90	0.5%	-4.00	-1.09	-39.25	35.86	0.1%
			5	6.00	1.91	58.87	35.87	0.6%	-6.00	-1.64	-58.87	35.86	0.1%
sensor no	861-20-XII		6	8.00	2.46	78.50	35.90	0.4%	-8.00	-2.19	-78.50	35.86	0.0%
range	20	kg	7	10.00	3.83	98.12	14.33	1.3%	-10.00	-2.74	-98.12	35.84	0.1%
			8	15.00	5.20	147.18	35.91	0.1%	-15.00	-4.10	-147.18	35.84	0.1%
amplifier	Picas		9	20.00	3.83	196.24	-35.89	0.1%	-20.00	-5.47	-196.24	35.84	0.1%
range in	2	mV/V	10	15.00	2.46	147.18	35.90	0.1%	-15.00	-4.11	-147.18	35.86	0.0%
range out	10	V	11	10.00	1.92	98.12	89.64	0.0%	-10.00	-2.74	-98.12	35.86	0.0%
R neutral	918.68	uV/V	12	8.00	1.37	78.50	35.89	0.2%	-8.00	-2.19	-78.50	35.86	0.0%
C neutral	517.11	uV/V	13	6.00	0.82	58.87	35.91	1.0%	-6.00	-1.64	-58.87	35.85	0.0%
			14	4.00	0.27	39.25	35.89	0.8%	-4.00	-1.10	-39.25	35.85	0.0%
			15	2.00	0.00	19.62	71.84	0.4%	-2.00	-0.55	-19.62	35.86	0.0%
			16	1.00	-0.27	9.81	35.91	0.3%	-1.00	-0.27	-9.81	35.86	0.2%
sens	35.159	N/V	17						0.00	0.00	0.00	35.85	0.1%
	0.236872												
	-61.11069												

Run				Run	11	F pos			Run	12	F neg		
				[kg]	[V]	[N]	[N/V]		[kg]	[V]	[N]	[N/V]	
date	1-Jun-22		step	massa	U	F	sens	accuracy	massa	U	F	sens	accuracy
			1	0.00	0.00	0.00			0.00	0.00	0.00		
chan	2		2	1.00	0.14	9.81	70.09	0.1%	-1.00	-0.14	-9.81	70.02	0.0%
name	F2Y		3	3.00	0.42	29.44	70.04	0.0%	-3.00	-0.42	-29.44	70.05	0.0%
			4	5.00	0.70	49.06	69.87	-0.2%	-5.00	-0.70	-49.06	70.01	0.0%
			5	10.00	1.40	98.12	70.04	0.0%	-10.00	-1.40	-98.12	70.03	0.0%
sensor no	047-40-X		6	15.00	2.10	147.18	70.05	0.0%	-15.00	-2.10	-147.18	69.95	-0.1%
range	40	kg	7	20.00	2.80	196.24	70.03	0.0%	-20.00	-2.80	-196.24	69.98	-0.1%
			8	25.00	3.50	245.30	69.99	0.0%	-25.00	-3.50	-245.30	70.01	0.0%
amplifier	Picas		9	30.00	4.20	294.36	70.03	0.0%	-30.00	-4.21	-294.36	70.01	0.0%
range in	2	mV/V	10	35.00	4.90	343.42	70.00	0.0%	-35.00	-4.91	-343.42	69.99	0.0%
range out	10	V	11	40.00	5.61	392.48	69.98	-0.1%	-40.00	-5.61	-392.48	69.99	0.0%
R neutral	-882.54	uV/V	12	35.00	4.91	343.42	70.12	0.1%	-35.00	-4.91	-343.42	70.10	0.1%
C neutral	-15.664	uV/V	13	30.00	4.21	294.36	70.00	0.0%	-30.00	-4.21	-294.36	70.06	0.1%
			14	25.00	3.51	245.30	70.06	0.1%	-25.00	-3.51	-245.30	69.95	-0.1%
			15	20.00	2.80	196.24	70.05	0.0%	-20.00	-2.81	-196.24	70.05	0.0%
			16	15.00	2.10	147.18	70.05	0.0%	-15.00	-2.10	-147.18	69.96	-0.1%
			17	10.00	1.40	98.12	70.08	0.1%	-10.00	-1.40	-98.12	70.00	0.0%
			18	5.00	0.70	49.06	70.06	0.1%	-5.00	-0.70	-49.06	70.02	0.0%
			19	3.00	0.42	29.44	69.94	-0.1%	-3.00	-0.42	-29.44	69.92	-0.1%
sens	70.017	N/V	20	1.00	0.14	9.81	70.09	0.1%	-1.00	-0.14	-9.81	70.01	0.0%
	0.140108		21	0.00	0.00	0.00			0.00	0.00	0.00		

Figure E.2: Data book of force transducer calibration, the accuracy of each measurement is with respect to the computed calibration factor denoted in orange on the left side for each sensor.

F

Pressure sensors pre-calibration results

STEPS [mm]	9010	7694	6410	5116	3832	2505	slope [V/mm]	intercept [V]	R-squared
P01	1.986038	1.745961	1.511622	1.275116	1.039749	0.796487	0.000182793	0.339413825	**0.9999968**
P02	2.804628	2.508062	2.218776	1.925543	1.634636	1.333436	0.000226376	0.766468461	**0.99999836**
P03	2.688976	2.39526	2.108402	1.817679	1.529068	1.230313	0.0002242	0.670014312	**0.99999852**
P04	2.519484	2.231226	1.949742	1.664272	1.381322	1.088035	0.000220147	0.537316712	**0.9999985**
P05	0.574547	0.426855	0.282696	0.13665	-0.00798	-0.1586	0.000112668	-0.44005466	**0.99999827**
P06	0.766578	0.613855	0.464972	0.314046	0.163938	0.008454	0.000116401	-0.28183125	**0.99999683**
P07	0.665004	0.516158	0.370158	0.222435	0.075777	-0.07583	0.000113892	-0.36047508	**0.99999691**
P08	0.506254	0.360879	0.219381	0.076032	-0.06625	-0.21348	0.000110699	-0.49067436	**0.99999906**
P09	0.857669	0.705038	0.555936	0.404067	0.255394	0.101309	0.000116461	-0.19111766	**0.99999396**
P10	0.66192	0.509643	0.361084	0.210898	0.06151	-0.09129	0.000115824	-0.38160641	**0.99999895**
P11	0.551291	0.406912	0.266214	0.123646	-0.01761	-0.16399	0.000110002	-0.43936958	**0.99999925**
P12	0.741993	0.588257	0.439245	0.284418	0.133994	-0.02132	0.000117346	-0.31480411	**0.99999255**
P13	1.470861	1.152932	0.842736	0.528386	0.216742	-0.10577	0.000242652	-0.71385717	**0.99999798**
P14	1.431893	1.115797	0.810089	0.497215	0.183897	-0.13397	0.000239478	-0.72755865	**0.99996706**
P15	1.510153	1.196383	0.890276	0.58008	0.272458	-0.04625	0.000239457	-0.64588428	**0.99999854**
P16	1.265946	0.953232	0.648118	0.338935	0.032257	-0.28537	0.000238557	-0.88225403	**0.99999889**
P17	1.67866	1.357176	1.043496	0.725689	0.410521	0.084354	0.000245322	-0.53019689	**0.99999828**
P18	1.892215	1.567578	1.250855	0.929993	0.611753	0.28243	0.000247518	-0.33688237	**0.99999922**
P19	1.709883	1.408016	1.113511	0.815149	0.519272	0.213552	0.000230207	-0.36314871	**0.99999898**
P20	1.467711	1.159503	0.858789	0.55404	0.251948	-0.06057	0.000235161	-0.6497288	**0.9999986**
P21	-1.12983	-1.28995	-1.44619	-1.60449	-1.76147	-1.92388	0.000122176	-2.22992544	**0.99999844**
P22	1.200607	0.912777	0.628445	0.340978	0.063983	-0.24143	0.000221995	-0.79547029	**0.99996783**
P23	-1.05868	-1.2197	-1.37661	-1.53523	-1.69206	-1.85339	0.000122355	-2.16097155	**0.99999762**
P24	1.427046	1.128925	0.83611	0.527853	0.232865	-0.07559	0.000231196	-0.65215171	**0.99997913**
P25	1.440788	1.139313	0.847606	0.543005	0.247465	-0.06079	0.000230784	-0.63650422	**0.99999034**
P26	1.128783	0.822156	0.522908	0.219848	-0.08105	-0.39428	0.000233897	-0.9776016	**0.99999679**
P27	-1.13672	-1.29735	-1.45264	-1.61345	-1.77181	-1.93295	0.000122322	-2.23864284	**0.99999054**
P28	1.307843	1.000789	0.702697	0.403326	0.096192	-0.21204	0.000234156	-0.7995961	**0.99998926**
P29	5.397841	4.235839	3.08806	1.94574	0.793203	-0.39957	0.000892343	-2.63180155	**0.99999227**
P30	7.076487	5.86726	4.686178	3.489616	2.304791	1.070314	0.000923057	-1.23551415	**0.99999732**
P31	7.329337	6.124584	4.948463	3.756705	2.574844	1.350559	0.000919347	-0.9492405	**0.9999989**
P32	6.873712	5.565609	4.246419	2.936443	1.63262	0.284729	0.001011219	-2.23343208	**0.99998045**
P33	4.95313	3.75828	2.534015	1.356809	0.153764	-1.08303	0.000927783	-3.39867217	**0.99998678**
P34	3.896861	2.822668	1.759685	0.688331	-0.38214	-1.45996	0.000825002	-3.53148538	**0.99998783**
P35	5.552799	4.417257	3.308972	2.185773	1.071232	-0.08225	0.000866664	-2.2510599	**0.99999864**
P36	4.767202	3.652009	2.539998	1.421706	0.308476	-0.85008	0.000867082	-3.02496086	**0.99998306**

Figure F.1: Data book of pressure sensors of pre-calibration. Most right column depicts the R-squared values per sensor.

G

Misalignment of foil and correction to the force data process script

This section explains how a misalignment was found based on the lift and drag coefficient plots. The steps are undertaken to find where the discrepancy was coming from and how to solve this. The lift and drag curves first attained are shown in figure G.1. This shows a lift coefficient which goes trough zero and an indication of stall angle at AoA 16°. The drag coefficient curve is wrong. It is not symmetric around AoA 0°.

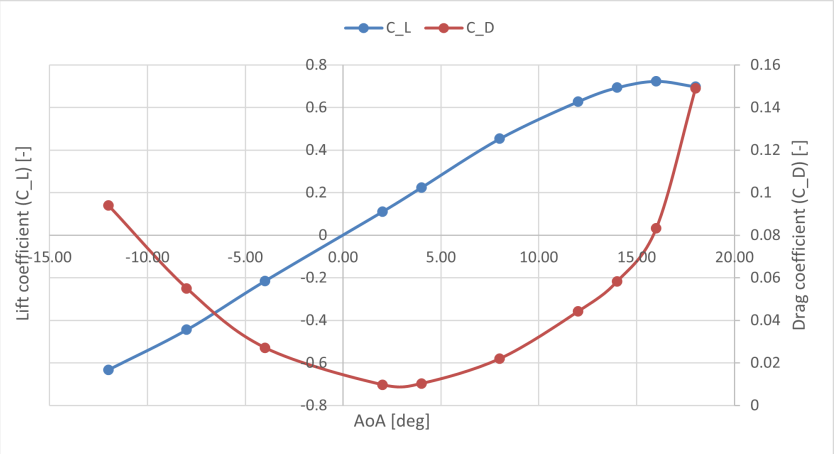

Figure G.1: Lift and drag coefficient for a NACA0012 surface-piercing hydrofoil, AR 3.46, Re $3.42 \cdot 10^5$

Based on this drag coefficient curve it can be said the misalignment is 3°. The lift coefficient is not shifted, this is therefore not the solution. A lot of testing into the 6DOF frame is executed. By pulling and pushing in all three directions the live response is observed. From this, it is established that the response of the sensors matches the direction of force imposed. Further electrical checks are carried out to see if the problem comes anywhere from the sensors and or cables. The F3Y force sensor is found to have a loose ground and upon further inspection, the entire sensor is deemed corrupt. The 6DOF frame is taken apart and a new calibrated sensor is placed inside the frame. There after the cross-check calibration on the entire frame is carried out again.

To be sure the problem was not partly due to the model itself first a different test geomtery is mounted. A T-foil is attached to the 6DOF that is known to be symmetric from previous experiments. The raw result of these static runs are shown in figure G.2.

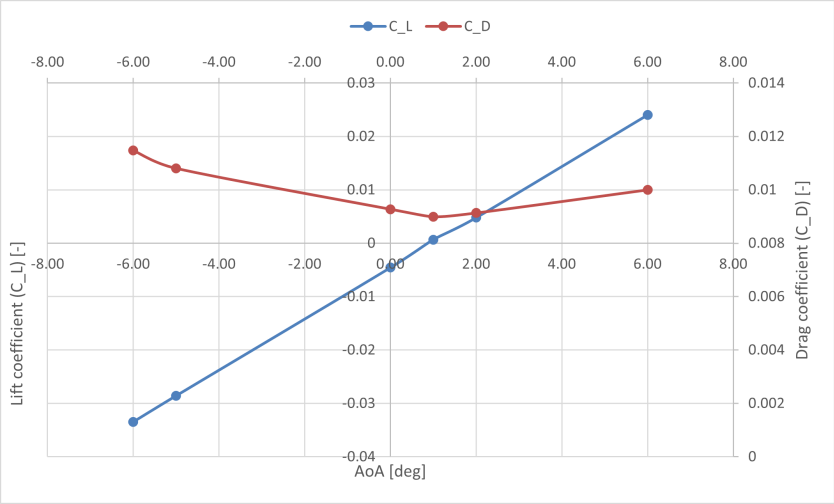

Figure G.2: Lift and drag coefficient for a NACA0012 tapered T-foil, Re $3.42 \cdot 10^5$

Both lift and drag curves are not symmetric over AoA 0°. They do however show the same offset, the curves do coincide with each other. This means the error is not present in the measurement frame anymore. And based on this result an angular misalignment due to mounting to the 6DOF can be found and corrected. The T-foil is dismounted and the correct test geometry is mounted again.

Again static runs are carried out to check for the misalignment between foil and 6DOF frame. The lift and drag curves are shown in figure G.3. The results look different to those in figure G.1, this is both a result of fixing the electrical problems and the human factor in angular misalignment whilst mounting the foil to the 6DOF.

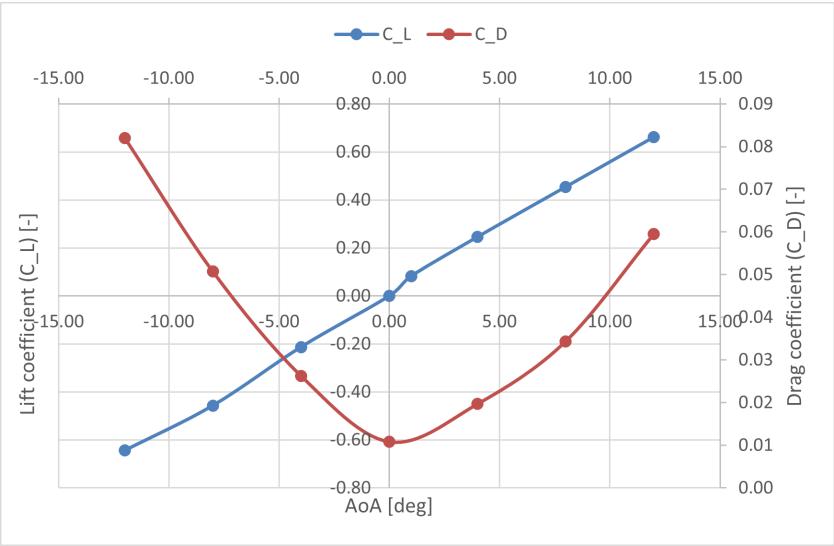

Figure G.3: Lift and drag coefficient for a NACA0012 surface-piercing hydrofoil, AR 3.46, Re $3.42 \cdot 10^5$

A skew is observed in the drag curve. By tweaking the data for different angles between 6DOF and foil in the data process (Eq. 5.2b) a misalignment of 0.8° is found (see figure G.4). This angle is implemented in the script. And this angle is corrected for within the Hexamove coordinate system, this ensures that when imposing an AoA 2°, this is in fact a 2° and not 2.8°. This completes the process of finding the misalignment.

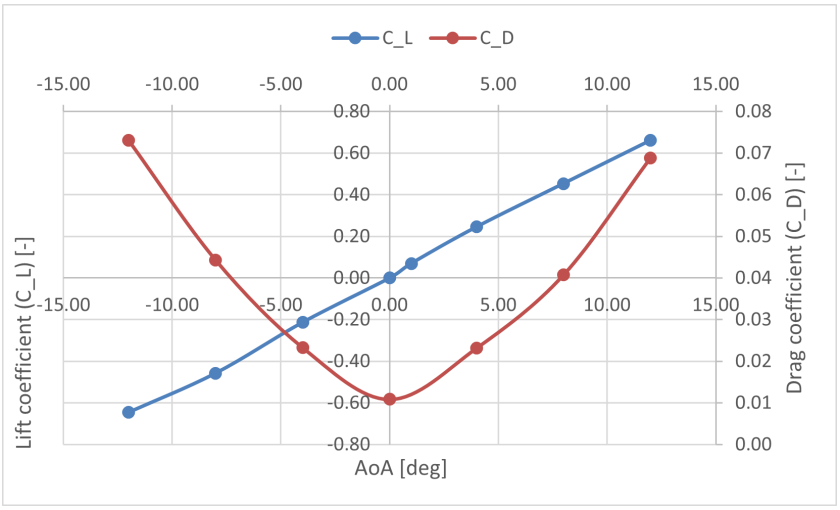

Figure G.4: Lift and drag coefficient for a NACA0012 surface-piercing hydrofoil, AR 3.46, Re $3.42 \cdot 10^5$, with a 0.8° misalignment angle correction